UNIVERSITY of CALIFORNIA
Santa Barbara

Quantitative Analysis and Modeling of Confocal Retinal Images

A Dissertation submitted in partial satisfaction
of the requirements for the degree

Doctor of Philosophy
in
Electrical and Computer Engineering

by

Jiyun Byun

Committee in Charge:

Professor B.S. Manjunath, Chair
Professor Shivkumar Chandrasekaran
Professor Steven K. Fisher
Professor Kenneth Rose
Professor Ambuj K. Singh

June 2007

The Dissertation of Jiyun Byun is approved.

Professor Shivkumar Chandrasekaran

Professor Steven K. Fisher

Professor Kenneth Rose

Professor Ambuj K. Singh

Professor B.S. Manjunath, Committee Chair

April 2007

Quantitative Analysis and Modeling of Confocal Retinal Images

by

Jiyun Byun

To the glory of God

Acknowledgements

Completing my graduate studies at UCSB has been a wonderful journey. A journey is easier when you travel together. My doctorate is the result of work whereby I have been accompanied and supported by many people. I am happy to have an opportunity to express my gratitude for all of them.

First and foremost, I would like to thank Professor Manjunath for his constant support and guidance. I have been privileged to have Prof. Manjunath as my advisor. He always remains available in spite of his extremely busy schedule and helps me staying at the right track of interdisciplinary research. He teaches me how to create tangible outcome yet not to lose the big picture.

I am grateful to my doctoral committee members: to Prof. Chandrasekaran for always providing me interesting idea to solve the problems, to Prof. Rose for valuable comments and discussions, to Prof. Singh for helpful discussions, and to Prof. Fisher for sharing his expertise in retinal cell biology with me. Beside the committee members, I owe a debt of gratitude to all the members of Prof. Fisher's lab. Dr. Lewis provides beautiful data collections and interests me in knowing more about the retina. I enjoyed working with Dr. Verardo who was full of energy and excitement. I also would like to thank to Kenneth Linberg, Ethan Chapin, Gabe Luna, and Dr. Banna. Without their devotions, this work would not be possible.

I also like to acknowledge the National Science Foundation for providing me a chance to work on such an interesting project and supporting my research (grant NSF ITR #0331697).

It has been pleasure to work with smart and interesting people both at the Vision Research Lab and at the Center of Bio-image Informatics at UCSB. Their support, helpful discussion, energy and friendship have enriched my life. I have been benefitted from collaboration with Luca Bertelli, Dmitry Fedorov, Thomas Kuo, Bariş Sümengen, Nhat Vu, and Marco Zulliani. Laura Boucheron has been a great support and encouragement. I would like to thank all colleagues, past and present: Alphan Altinok, Arnab Bhattacharya, Sitaram Bhagavathy, Zhiqiang Bi, August Black, Onkar Dabeer, Elisa Drelie Gelasca, Pratim Ghosh, Ohashi Gosuke, Ibrahim El-Khalil, Kristian Kvilekval, Vebjorn Ljosa, Emily Moxley, Shawn Newsam, Mike Quinn, Emre Sargin, Anyndia Sarkar, Motaz El-Saban, Kaushal Solanki, Xinding Sun, Jelena Tešić, Lei Wang, and all the past and current visiting researchers.

I would like to thank to my other fellow graduate students Enki Yoo, Minkyoung Park, Sanguk Ryu, Jaehyuk Shin, Byoungchae Kim, Dongwoo Hong, Joomi Kim, Taehyuk Gang, Suckseung Hwang, and Sunwoo Kim. During these years I shared numerous wonderful moments with my friends who always encourage me and pray for me: Sumin Kim, Joyce Moon, Jieun Jun, Soojun Ahn, Jongyoon Han, Hyunah Kim, and Il-Kee Moon. My sincere gratitude goes to Prof. Long who became my spiritual mentor, Pastor Hakcheon Kim, and Mrs. Kim. All my old friends from the Computer Vision Lab in South Korea also deserve to acknowledged here for their support: Jongmin Kim, Sungyoung Kim, Daesung Moon, Sanghoon Lee, Younghee Gil, and Gilman Lee. I am grateful for Prof. Kim whose enthusiasm toward research attracts me to start this experience.

I have no words to express gratitude towards my family. Without their endless love, encouragement, and support, this wonderful journey would not have begun. My parents deserve all the credit what I have achieved. When I was discouraged to enter the engineering school, they remind me what I have been longing since I was a little girl. They always encourage me to go extra mile and support me whenever I am discouraged. I am indebted to my sister, Nature, for her continuous support and encouragement.

I especially thank my best friend, Jeonghee Shin, who started this journey with me. I could go through and enjoy the journey by walking with her.

A special thanks to Ken for his support, his faith, unique and special 50,000 miles of journey he shared with me, and his love. I am also thankful to Ken's family for their caring support and Hello Kitty encouragement.

Curriculum Vitæ

Jiyun Byun

Education

2007	Doctor of Philosophy Department of Electrical and Computer Engineering University of California, Santa Barbara.
2006	Master of Science Department of Electrical and Computer Engineering University of California, Santa Barbara.
2000	Master of Engineering Department of Computer Engineering Pusan National University, Pusan, South Korea.
1998	Bachelor of Engineering Department of Computer Engineering Pusan National University, Pusan, South Korea.

Experience

2002 – 2007	Graduate Research Assistant University of California, Santa Barbara.
2004	Summer Intern Samsung Advanced Institute of Technology, South Korea.
2001	Research Assistant Research Institute of Computer, Information & Communication, Pusan National University, South Korea.
2000	Teaching Assistant Computer Center, Pusan National University, South Korea.
2001	Intern Research Institute of Computer, Information & Communication, Pusan National University, South Korea.
1998 – 2000	Research Assistant Pusan National University, South Korea.
1998	Teaching Assistant Pusan National University, South Korea.

Selected Publications

L. Bertelli, J. Byun and B. S. Manjunath, "A Variational Approach to Exploit Prior Information in Object-Background Segregation: Application to Retinal Images," *IEEE International Conference on Image Processing (ICIP)*, 2007.

S. K. Fisher, M. R. Verardo, J. Byun, G. P. Lewis, G. Luna, S. Kjellstrom, and P. Sieving, "Retinal Changes Following Experimental Retinal Detachment In The Retinoschisin Knockout Mouse," in *Association for Research in Vision and Ophthalmology (ARVO) E-Abstract 1538*, Apr 2007.

J. Byun, M. R. Verardo, N. Vu, D. Fedorov, G. P. Lewis, S. K. Fisher, and B. S. Manjunath, "Quantifying structural distortions in retinal tissue before and after injury," *In 2006 Workshop on Multiscale Biological Imaging, Data Mining & Informatics*, Sep 2006.

J.Byun, M. R. Verardo, B. Sumengen, G. P. Lewis, B. S. Manjunath, and S. K. Fisher, "Automated tool for the detection of cell nuclei in digital microscopic images: Application to retinal images," in *Molecular Vision, vol. 12, pp. 949.960*, Aug 2006.

S. K. Fisher, J. Byun, D. Fedorov, N. Vu, B. Sumengen, M. Verardo, G. P. Lewis, and B. S. Manjunath, "Image informatics tools for the analysis of retinal images," in *Invest Ophthalmol Vision Science 2006;47: Association for Research in Vision and Ophthalmology (ARVO) E-Abstract 4225*, Apr 2006.

B. S. Manjunath, B. Sumengen, Z. Bi, J. Byun, M. El-Saban, D. Fedorov, and N. Vu, Towards automated bioimage analysis: From features to semantics, in IEEE International Symposium on Biomedical Imaging (ISBI), Apr 2006.

J. Byun, N. Vu, B. Sumengen, and B. S. Manjunath, "Quantitative Analysis of Immunofluorescent Retinal Images," in *IEEE International Symposium on Biomedical Imaging: From Nano to Macro (ISBI)*, Arlington, Virginia, USA, Apr 2006.

J. Byun, L. Wang, G. P. Lewis, S. K. Fisher, and B.S. Manjunath, "Challenges in Bio-Molecular Imaging and Information Discovery: Developing a Searchable, distributed Retinal Image Database," in *The Association for Research in Vision and Ophthamalogy (ARVO)*, Apr 2004.

Abstract

Quantitative Analysis and Modeling of Confocal Retinal Images

by

Jiyun Byun

Images have become critical components for a detailed understanding of the structure and function of cells and proteins. For example, confocal microscopy images are used to obtain a better understanding of several critical functions of the central nervous system (CNS), such as mechanisms behind the loss and recovery of vision following retinal detachment. Image processing and information discovery tools increasingly play a significant role in better harvesting these vast amounts of data, most of which is currently analyzed manually and qualitatively.

The main contribution of this work is the development of quantitative analysis and modeling of bio-molecular images. We focus primarily on retinal images for characterizing patterns of cellular/ subcellular protein distribution and changes in such patterns. Specifically, we develop an automated nucleus detection method which provides reliable and accurate results for counting cell nuclei. Quantitative measurements to characterize the structural distortion of the retina, including layer thickness, local cell density, and distortion indices, are proposed. We model the retinal detachment process using a Bayesian network in order to understand the protein-protein interactions within the retinal cells as well as interactions between cells. Quantitative analysis and statistical modeling provide opportunities to test therapeutic agents that may reduce the damaging effects of detachment or improve the outcome of reattachment surgery.

Contents

List of Tables

List of Figures

Chapter 1

Introduction

"A picture is worth a thousand words,
but a model is worth a thousand pictures."

Imaging technologies for biology research have seen much progress during the past decade. For example, fluorescence microscopy is extensively used in generating high resolution images with subcellular resolution. Images have become critical components for building/obtaining a detailed understanding of the structure and function of cells and proteins. These images are used to obtain better understanding of several critical functions of the central nervous system (CNS), such as mechanisms behind the loss and recovery of vision following retinal detachment. Image processing and information discovery tools increasingly play a significant role in better harvesting this vast amount of data, most of which is currently analyzed manually and qualitatively.

The main contribution of this work is the development of quantitative analysis and modeling methods of bio-molecular images, in particular retinal images, for characterizing patterns of cellular/subcellular protein distribution and changes in

such patterns. The experimental data comes from Steve Fisher's laboratory at UCSB that has been studying retinal detachment for over 25 years. We provide a quantitative understanding of mechanism behind vision loss and recovery after injury from the images through automated analysis and statistical modeling. These quantitative analyses provide opportunities to test therapeutic agents that may reduce the damaging effects of detachment or improve the outcome of reattachment surgery. Additionally, the detailed understanding leads us to develop new hypotheses. While we focus on specific biological problems relating to retinal images, the underlying issues and proposed solutions are applicable to a broader class of images ranging from a single cell to whole organisms.

1.1 Introduction to Retinal Images

The retina is the light-sensitive layer of tissue that lines the inside of the eye. It shares limited regenerative capabilities of the CNS. This has profound consequences for the return of function after injury. Retinal detachment is a fairly common physical injury involving separation of the neural retina from the underlying monolayer of pigmented epithelium. Because it can cause blindness in the affected area if left untreated, retinal detachment is considered an ocular emergency that requires immediate medical attention and surgery. While surgical success is very high at over 90%, much remains unknown about the degenerative processes that lead to visual defects, and little is understood about the biology of the regenerative process. For this reason, understanding and characterizing the functional effects of cellular changes initiated by detachment and reattachment are important.

Understanding the mechanisms behind the loss and recovery of vision following retinal detachment and reattachment has been the focus of studies for many years [27]. Steve Fisher's lab at UCSB is a leading research laboratory of retinal detachment studies. They have provided the basis for the current understanding of the retinal detachment and also pioneered the use of oxygen therapy to slow or reverse the negative effects of retinal detachment.

Analysis is usually done by comparing normal to detached retinas using different views, cross section and wholemount, and considering the difference between the two patterns. The most common method for determining cellular and subcellular patterns is through fluorescent images, which are generated by emitted fluorescence light (in essence "dark field" imaging) collected by confocal laser scanning microscopy (CLSM). An antibody is used to visualize a specific cell shape and protein distributions in the retina. Figure 1.1 shows example images of retinas labeled with antibody to rod opsin. This experimental image set is generated to answer the question '*How does the pattern of rod opsin protein expressions change in response to detachment?*'. The deconstruction of the rods involves a number of other characteristic responses to detachment [27]. One response is the 'redistribution' of rod opsin molecules in the plasma membrane that surrounds the inner portions of the rod photoreceptors within the outer nuclear layer (ONL). Localization, level of protein expression, and the pattern of rod opsin protein expression distribution are the main features to interpret this image set. However, qualitative differences between two samples are often characterized using vague parameters such as "texture", "fuzziness", "shape", or "somewhat flattened appearance" [43]. While experts are good at recognizing generic spatial features in

such images, such as structures, abnormalities, shapes, and the like, their resulting qualitative observations are often difficult to reproduce in a scientific experiment.

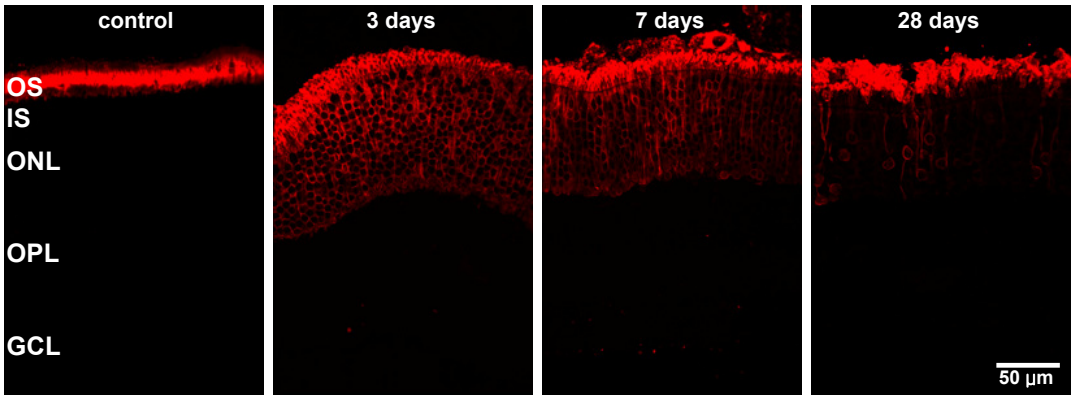

Figure 1.1: Confocal images of retinas immunolabeled with antibody to rod opsin (red) (a) Normal retina. Anti-rod opsin labeling is restricted to the outer segments (OS). (b) 3-day detached retina. Anti-rod opsin labels the truncated OS and rod cell bodies in the ONL. (c) 7-day detached retina. (d) 28-day detached retina. Anti-rod opsin labels OS fragments as well as rod cell bodies in the ONL.

There are challenges in deriving quantitative descriptions of the above mentioned phenomenon. The descriptions include, for example,

- *quantitative evaluation of damage to photoreceptors*: the number of photoreceptors is a common measurement of visual function of retina. (image processing tools: segmentation and automated nuclei counting).

- *determining cellular and subcellular changes in response to detachment*: to quantify the change in rod opsin distribution, segmenting retinal layers (ONL in Figure 1.1) is necessary. (image processing tools: segmentation and layer classification).

- *discovery of underlying relationships between the distribution of rod opsin and other proteins/cells* (pattern recognition tools: statistical modeling,

spatio temporal models, and Bayesian networks).

Ideally an image analysis tool should have the pattern recognition abilities of a human and the fast and accurate evaluation of the computer to allow feature based representation, discover non-obvious pattern/relationships, and model spatio temporal patterns. Ultimately this can lead us to a better understanding of retinal detachment via modeling, which can provide opportunities to test therapeutic agents that may reduce the damaging effects of detachment or improve the outcome of reattachment surgery.

1.2 Challenges in Analyzing Retinal Images

The structure and organization of the different cell types constituting the retinal tissue pose interesting challenges to image analysis and pattern recognition. In this thesis, we focus primarily on retinal images that are stained with antibodies and collected with confocal laser scanning microscopy. We outline below some of the major issues:

- **Segmentation**

  - Heterogeneity in morphology between objects/regions: Image data in an individual retinal layer is not statistically homogeneous information. This is one of the fundamental problems in segmenting micrographs [62]. Further difficulties in retinal images include visual variation from staining. For example, the same layer can show different structures depending on the probed antibodies.

- **Object representation and feature selection**

  - Intrinsic variance between samples: Another demanding element is the intrinsic variance between samples. Any biological system exhibits significant variations. Unfortunately, the resources of tissues are limited so it is practically impossible to collect enough images to cancel out noise and variance between samples under the same conditions. It is crucial to extract robust features that capture common characteristics from the images under the same conditions in spite of the variance, yet have the capacity of discriminating subtle variation among images from different conditions.

- **Spatial-temporal modeling**

  - Observations cannot take place on the same sample over time: Images are collected from retinal cross section/wholemount at intervals of one day after retinal detachment, 3 days, 7 days, and 28 days. Each sample comes from a different animal and the sampling tissue is often ad hoc and not evenly spaced. Coupled with technical variabilities in sample preparations and image acquisition, the underlying image representation is sparse and heterogeneous.

- **Data sparcity**

  Since every data set is generated to answer specific experimental questions, the data set usually consists of a relatively small number of images from various conditions. Each data set may require extracting different features depending on the hypothesis. It is a challenge to combine each result from various experiments to discover interesting patterns over all data. Addition-

ally, single plane images extracted from z-series, a series of optical sections through the depth of a specimen, are redundant. They do not provide much additional information. Thus maximizing the amount of information attainable from a single sample is very important.

1.3 Main Contribution

In this thesis, we propose a set of quantitative methods to characterize the cellular changes associated with retinal detachment. Specifically,

- **Automated nucleus detection (Chapter 4 and Chapter 5).**
  We design an automated nucleus detection method for counting photoreceptor nuclei. This method replaces the time consuming, and also routinely repeated manual analysis with a robust, easy to use software. The proposed method has been actively used for providing quantitative information to prove/reject various hypotheses of the response of the retina to detachment and reattachment [37, 26].

- **Quantification of structural distortion in the retina (Chapter 5).**
  Based on the nuclei detection results, we introduce the first thorough quantitative analysis for retinal images. Our quantitative measurements are corroborated by conclusions derived from manual measurements and qualitative assessments, and provide significant information about local structural changes during retinal detachment [10, 9].

- **Layer segmentation and classification (Chapter 6).**
  We propose segmentation methods which provide a reliable map of the reti-

nal layers within an image. The developed layer segmentation and classification greatly simplifies the image analysis tasks for understanding the events initiated by retinal detachment.

- **Modeling and pattern discovery in retinal images (Chapter 7).** We model the retinal detachment process in order to understand protein-protein interactions within the cells as well as interactions between cells. A Bayesian network framework is ideally suited to study this problem. A recovered causal network with quantitative features derived from retinal images elucidates most of the traditionally reported relationships and also predicts the interesting causal relationship between expressions of rod opsin and glial fibrillary acid protein (GFAP), and photoreceptor cell density. The method of Bayesian networks is also applied to characterize the effect of detachment in genetic mutant mice. An interesting finding from the constructed network confirms the plausibility of a new treatment (gene therapy).

1.4 Thesis Organization

This thesis is organized as follows. In Chapter 2 we introduce the retina, retinal detachment, and recent high resolution retinal imaging techniques. Details of image processing issues for quantitative analysis are also discussed. Chapter 3 provides a brief background of the methods which we employ to characterize the changes in retina. In Chapter 4, we present the generic nucleus detection methods which are applicable to a wide range of image types, sample preparations, and imaging methods. In Chapter 5, we extend results of Chapter 4 by

automating counting photoreceptor nuclei within the ONL. Based on the nucleus detection results, we propose a novel method to quantitatively analyze and characterize structural distortion of a retina after injury. In Chapter 6, we propose an approach to segment and classify the retinal layers using image driven features and metadata/content. The combination of all quantitative measures (cell counts, layer thickness, local cell density, and distortion indices) provides important information which has not yet been reported. In Chapter 7, we shift our focus to modeling the retinal detachment process. We demonstrate how the above tools (described in Chapters 3 - 6) are applied to extract quantitative information from retinal images, and to model the retinal detachment process. We discover underlying relationships between proteins for which there is little knowledge. The detailed understanding of retinal detachment via modeling can provide opportunities to test therapeutic agents that may reduce the damaging effects of detachment or improve the outcome of reattachment surgery. It may also reveal information of use for understanding other causes of blindness rooted in retinal defects or injuries. We summarize our conclusions and discuss further research directions in Chapter 8.

Chapter 2

Retinal Detachment

"You cannot depend on your eyes
when your imagination is out of focus."

Mark Twain

Understanding the mechanisms behind the loss and recovery of vision following retinal detachment and reattachment has been the focus of study for many years. Here we survey the current research of cellular remodeling in mammalian retina in response to retinal detachment and reattachment. We specifically focus on recent high resolution retinal imaging techniques, image processing problems for quantitative analysis, and image analysis challenges in immunofluorescent retinal images.

2.1 Structure and Function of The Retina

2.1.1 Overview

The retina is the light-sensitive layer of tissue that lines the inside of the eye and sends visual messages through the optic nerve to the brain. The retina shares limited regenerative capabilities of the central nervous system (CNS). This has profound consequences for the return of function after injury. The retina offers a unique opportunity to study neuronal diseases experimentally and in patients as it is the only part of the CNS that is directly visible and remains the most surgically accessible.

All vertebrate retinas are composed of three layers of cell bodies and two layers of synapses (Figure 2.1). Figure 2.1 (b) shows a simplistic drawing of a cross section of a retina. The ganglion cells (G in Figure 2.1 (b)) lie in the innermost region of the retina closest to the lens and front of the eye, and the photoreceptors (rods and cones) lie in the outermost region of the retina adjacent to the retinal pigment epithelium (RPE). In other words, the "raw" image is actually formed at the back (the photoreceptors) and the "processed" signal is routed inward by converging axons from a series of integrator cells (bipolar and horizontal cells) located in the inner portion of the retina. The most logical way to understand the layers of the retina is to consider them in sequential order as a progression of events in the transduction of vision, beginning at the innermost and following the signal through the outermost photoreceptors and back to the point of exit via the optic nerve. Light enters from the ganglion cell layer (GCL) and travels through different cell types in the retina before activating the rod and cone photoreceptors.

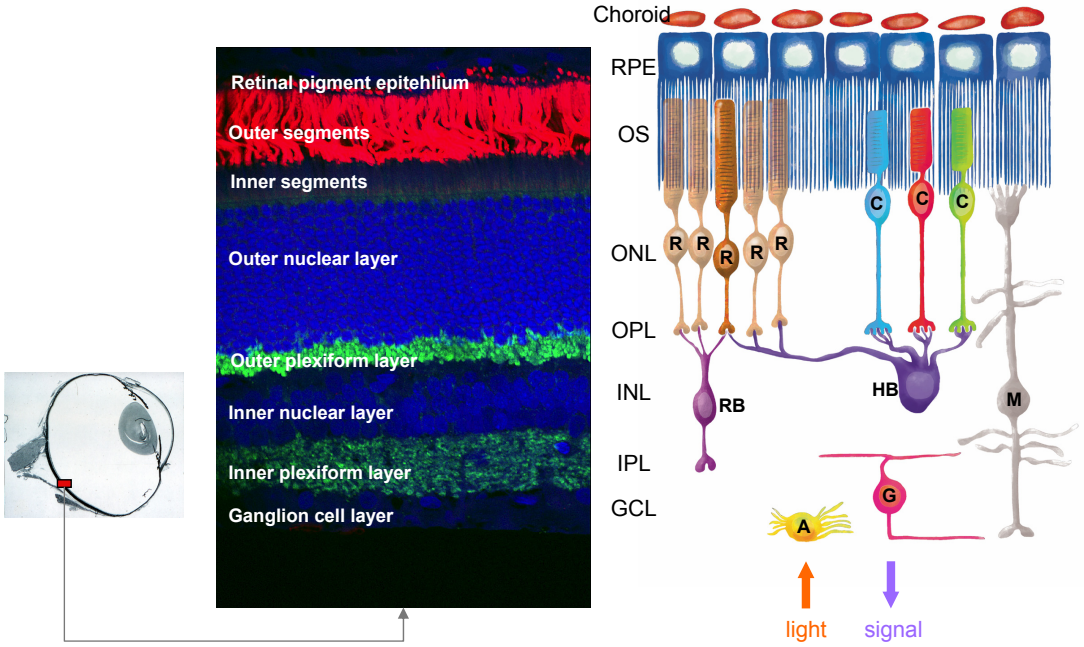

(a) (b)

Figure 2.1: Retinal layers. (a) Confocal microscopy of a vertical section through a cat retina. (b) A drawing representing the retinal cell types discussed in [27] (Figure 1 in [27]) (courtesy of Steve Fisher's lab). The outer segments of rod (R) and cone (C) photoreceptors interdigitate with the apical surface of the retinal pigment epithelium (RPE). The photoreceptor cell bodies comprise the outer nuclear layer (ONL), and their synaptic terminals end in the outer plexiform layer (OPL). The dendrites of rod bipolar cell (RB) and the axon terminals of the B-type horizontal cell (HB) are postsynaptic to rod photoreceptors. The dendrites of the HB cell are postsynaptic to cones. Axons of rod bipolar cells terminate in the inner plexiform layer (IPL) . The dendrites of ganglion cells (G) terminate in the IPL and their axons form the optic nerve. Their cell bodies comprise the ganglion cell layer (GCL). A population of astrocytes (A) lies in the GCL . Müller cells (M) are the radial glia of the vertebrate retina. Their microvilli extend beyond the outer limiting membrane (OLM), their cell bodies lie in the inner nuclear layer (INL), and their endfeet abut the inner limiting membrane (ILM).

Subsequently, the absorption of photons by the visual pigments within the outer segments (OS) of the photoreceptors is translated into an electrical message that can signal through their cell bodies in the outer nuclear layer (ONL), and out to their axons. In the outer plexiform layer (OPL), rod photoreceptor axons contact the dendrites of bipolar cells (RB in Figure 2.1 (b)) and the axon terminals of B-type horizontal cells (HB in Figure 2.1 (b)). The rod bipolar cells (RB) in the inner nuclear layer (INL) process input from rod photoreceptors and horizontal cells (HB). Horizontal cells in the INL, interneurons which aid in signal processing, process input from both photoreceptors. Bipolar cell axons contact the dendrites of ganglion cells (G) and amacrine cells in the inner plexiform layer (IPL). The signal is relayed via the ganglion cell axons through the optic nerve to the brain. Ganglion cells, displaced amacrine cells, and astrocytes (A in Figure 2.1 (b)) comprise the ganglion cell layer (GCL). A vertical section of a retina illustrates its complexity and highly patterned architecture (Figure 2.1 (a)). Since the group of cell bodies or synaptic terminals of specific cell types comprise each layer, the normal architecture of layers is crucial to retinal function. Hence, changes in the integrity of the layers serve as an index of retinal function after injury. Moreover, this layer information is used for localizing specific cells and analyzing the effects of genes, drugs, stress, and protective factors on retinal integrity.

2.1.2 Retinal pigment epithelium (RPE)

The retinal pigment epithelium (RPE) is the pigmented cell layer outside the retina that nourishes retinal cells. RPE is firmly attached to the underlying choroid (the vascular layer of the eye), and their microvilli interdigitate with the

outer segments (OS) of photoreceptors (Figure 2.2). The RPE provides nutrition such as glucose and oxygen to the retina. It also has a vital function in ensuring the OS are supplied with vitamin A to maintain visual function. The RPE is composed of a single layer of hexagonal cells that are densely packed with pigment granules, melanin and lipofuscin. These pigment granules in the RPE increase the contrast of the visual images by absorbing light that would otherwise be reflected back inwards towards the photoreceptors. The morphology of the RPE changes after retinal injury or disease. These changes disrupt the interface between RPE and photoreceptors, in particular, the OS.

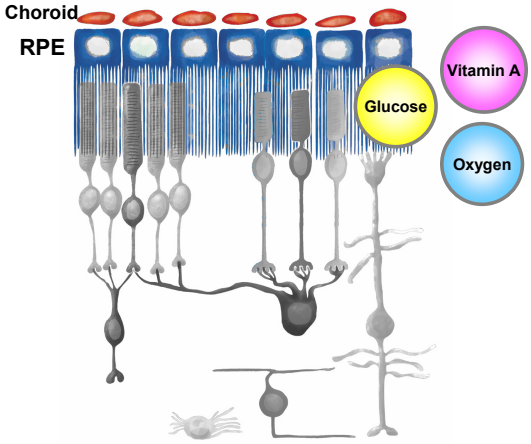

Figure 2.2: Retinal pigment epithelium. The drawing is modified from Figure 1 in [27] (courtesy of Steve Fisher's lab).

2.1.3 Photoreceptor layers

The outermost layer of the retina is comprised of rod and cone photoreceptors. These cells have a cell body, an axon, and outer segments (OS) and inner segments (IS). Outer segments are the actual light-sensitive elements containing visual pig-

ments. The visual pigment consists of a protein called opsin and a chromophore derived from vitamin A, known as retinal. The opsin and the chromophore are bound together and lie buried in the membranes of the outer segment discs. Outer segment degeneration is a common theme in all of the photoreceptor degenerative conditions, whether the underlying cause is genetic, disease, or injury. Figure 2.3 (a) and (b) show the outer segments of rods and cones of a normal cat retina collected by a confocal microscope.

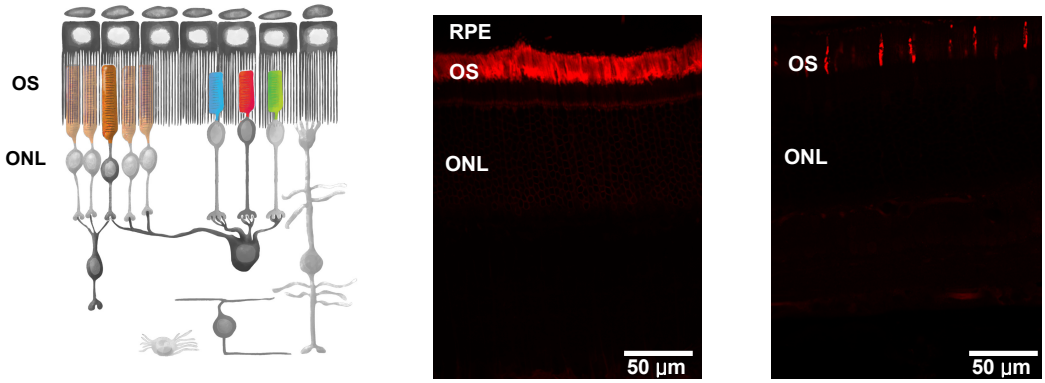

(a) (b)

Figure 2.3: Outer segments of photoreceptors. A drawing* of retinal layers highlighting outer segments of rods and cones is shown as a reference. (a) An example confocal image of a normal cat retina labeled with an antibody to rod opsin (red). Only the layer of rod outer segments (OS) is clearly labeled with this antibody. (b) A confocal image of a normal cat retina labeled with an antibody to medium (M)- and long (L)- wavelength-sensitive cone opsin (red). The feline retina has only M cones; thus only M-cone outer segments are labeled within the OS layer. *The drawing is modified from Figure 1 in [27] (courtesy of Steve Fisher's lab).

In the normal mammalian retina, rod opsin (Figure 2.3 (a)) is localized in the OS layer. In many degenerative conditions, outer segments become shortened over a period of a few days and rod opsin becomes redistributed to the plasma membrane of the IS and cell bodies. *The change in rod opsin distribution is a key*

feature for identifying degeneration of rod photoreceptors in response to injury. Outer segments of cone photoreceptors also lie in the OS layer and are greatly shortened and distorted under a degenerative condition. Hence their structural change is an important characteristic of injury.

2.1.4 The outer nuclear layer (ONL)

The nuclei of rods and cones constitute the ONL. Cone cell bodies are layered in columns below the outer limiting membrane (OLM). Some of the cone cell bodies are indicated by white arrows in Figure 2.4 (a). Rod cell bodies make up the remainder of the ONL below the cone cell bodies. Figure 2.4 (b) shows all the nuclear layers stained with a nuclear dye (blue).

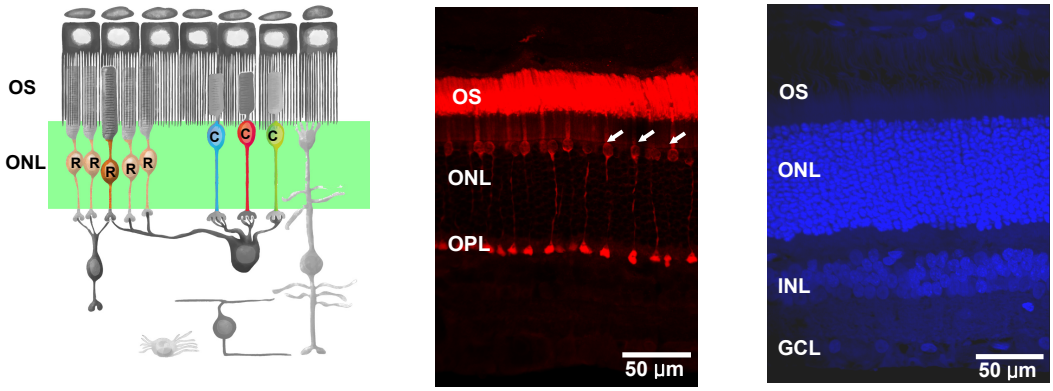

(a) (b)

Figure 2.4: The outer nuclear layer (ONL). A drawing* of retinal layers highlighting the outer nuclear layer is shown as a reference. *The drawing is modified from Figure 1 in [27] (courtesy of Steve Fisher's lab). (a) An example confocal image of a normal cat retina labeled with an antibody to PDEγ (red). The labeling shows rod and cone OS as well as the entire cone cell. White arrows indicate example cone cell bodies. (b) A confocal image of a normal cat retina stained with a nuclear dye TO-PRO (blue). Nuclei in all nuclear layers (ONL, INL, and GCL) are shown.

Nucleus staining is useful for identifying individual cells and associated events such as cell death. In particular, the number of photoreceptors within the ONL is a common measurement of the visual function of a retina. Additionally, the ONL is useful for image segmentation since the layer has a consistent pattern; this is due to the structural similarity of cell bodies among rods and cones. It is important to identify the ONL to locate all other layers since the patterns of other layers are not as consistent as that of the ONL, and are more difficult to recognize without knowledge of relationships between the retinal layers. In this way, the ONL serves as a baseline for characterizing the cellular changes under a degenerative condition, and identifying the other layers.

2.1.5 The outer plexiform layer (OPL)

Rod and cone photoreceptors generate the initial neural signal and pass it to the interneurons (bipolar, horizontal, and amacrine cells) for processing and further handling. The dendrites of these interneurons and the synaptic terminals of rods and cones (rod spherules and cone pedicles) constitute the OPL. The OPL is best appreciated when the photoreceptor terminals are labeled with any one of several antibodies to presynaptic proteins, such as synaptophysin and vesicle associated membrane protein (VAMP). Figure 2.5 shows an example image labeled with an antibody to synaptophysin. In the normal retina, the photoreceptor synaptic terminals form a compact layer in the OPL. The dendrites of rod bipolar cells specifically enter the synaptic invaginations of the rod photoreceptor's synaptic terminals (spherules) (Figure 2.6 (a)). The large cone photoreceptor's synaptic terminals (pedicles) form a single row adjacent to the neuropil, while

the more distally located, numerous, and smaller rod spherules form an orderly band. The organization of rod synaptic terminals and the morphology of cone pedicles reflect their cellular responses. For example, after retinal detachment, rod synaptic terminals appear near the rod nuclei scattered through the ONL. Such terminal withdrawal and reorganization has been used to identify cellular events after retinal detachment and reattachment.

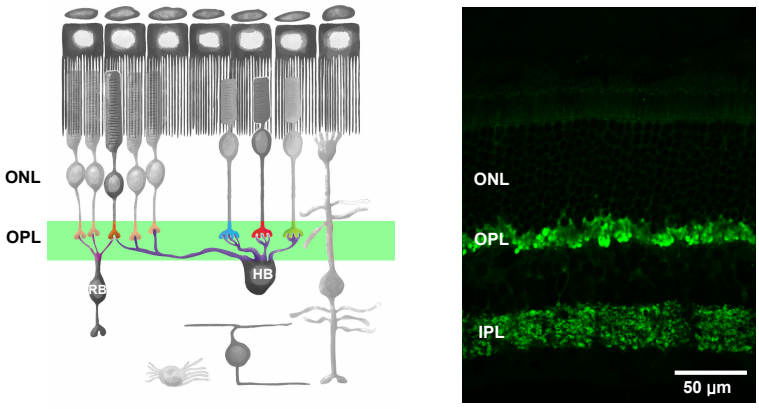

Figure 2.5: The Outer plexiform layer (OPL). Left: A drawing* of retinal layers highlighting the outer plexiform layer. Right: A confocal image of a normal cat retina labeled with an antibody to the synaptic vesicle protein, synaptophysin. The labeling is highly specific to the layer of photoreceptor synaptic terminals in the OPL illustrating the tightly packed ranks of photoreceptor terminals of a typical normal retina. *The drawing is modified from Figure 1 in [27] (courtesy of Steve Fisher's lab).

2.1.6 The inner nuclear layer (INL)

The cell bodies and nuclei of the interneurons, particularly the bipolar and horizontal cells, are located in the INL. Rod bipolar cells have multiple branched dendrites that terminate in the invagination of rod spherules. Rod bipolar cells can be observed by confocal imaging using an antibody to protein kinase C (PKC).

Figure 2.6 (a) shows the confocal image of a retina labeled with an antibody to PKC (red). The cell bodies of rod bipolar cells lie in the INL while their dendrites terminate in the OPL.

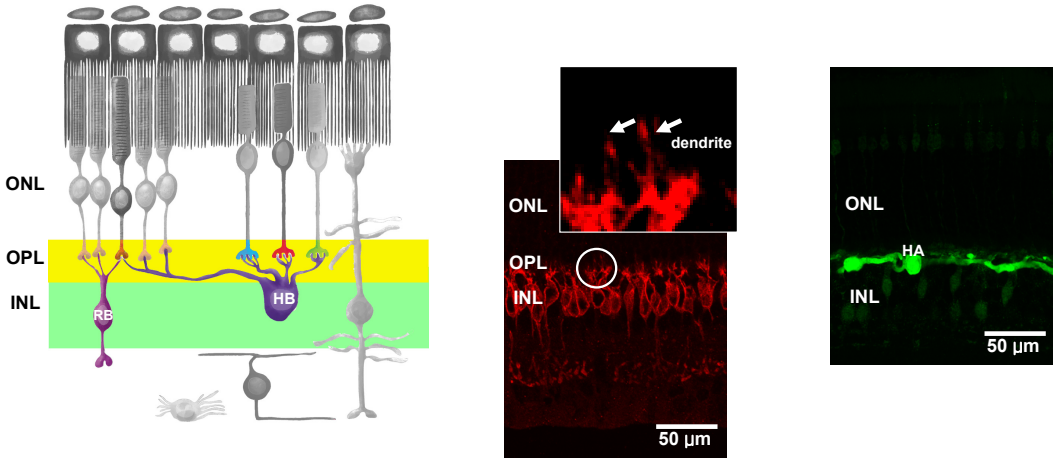

(a) (b)

Figure 2.6: The inner nuclear layer (INL). Left: a drawing* of retinal layers representing bipolar and horizontal cells. (a) The rod bipolar cells are labeled with an antibody to PKC (red) . Cell bodies of the rod bipolar cells reside in the INL and their dendrites (denoted by white arrows) enter the synaptic invagination of the rod spherules. (b) The A-type horizontal cells (HA) are labeled with an antibody to calbindin D (green). Cell bodies and their processes lie on the border of the INL. *The drawing is modified from Figure 1 in [27] (courtesy of Steve Fisher's lab).

The feline retina has two morphologically distinct horizontal cells; one with stout tapering dendrites and no axon (A-type) and the other with finer, highly branched dendrites and a long thin axon that forms an axon terminal (B-type). These two populations of horizontal cells are also distinguished based on the labeling signature (i.e. expressing protein) and location. The A-type horizontal cell contains calbindin D and calretinin demonstrating stout processes and a cell body that lies on the outer border of the INL (HA in Figure 2.6 (b)). The B-type hor-

izontal cell (HB in Figure 2.6 (a)) contains only calretinin having finer processes emerging from the cell body, and lies lower in the INL.

2.1.7 The inner plexiform layer (IPL)

The IPL, like the OPL, is a region of synapses. Here, the bipolar cells talk to different types of amacrine cells and to dendrites of the various ganglion cells. Similar to the OPL, the IPL is also visualized when the terminals are labeled with any one of several antibodies to presynaptic proteins. Figure 2.7 shows a confocal image of a retina labeled with an antibody to synaptophysin (green). In normal retina, bipolar cell axons and dendrites of amacrine and ganglion cells form a compact layer. This typical stratification in the IPL is no longer evident after injury.

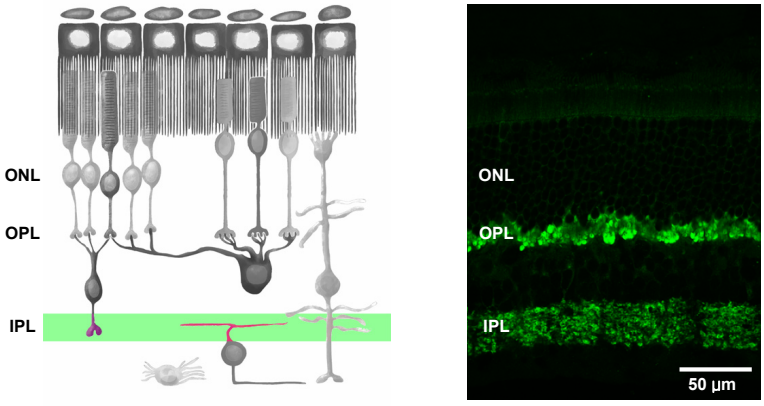

Figure 2.7: The inner plexiform layer (IPL). Left: A drawing* of retinal layer highlighting the IPL. Right: Confocal image of a normal cat retina labeled with an antibody to the synaptic vesicle protein, synaptophysin (green). The labeling is highly specific to the layer of synaptic terminals of bipolar cells in the IPL as well as OPL illustrating the stratum of bipolar cell terminals and dendrites of amacrine and ganglion cells. *The drawing is modified from Figure 1 in [27] (courtesy of Steve Fisher's lab).

2.1.8 The ganglion cell layer (GCL)

While the ganglion cells have synapses with bipolar cells in the IPL, their cell bodies are located in the next retinal layer, the GCL, which has far fewer nuclei than the inner or outer nuclear layers. Like other neurons, ganglion cells have axons, which carry the generated signal. These axons are bundled into tracts that run radially, converging at the site of origin of the optic nerve. The optic nerve collects all the axons of the ganglion cells and this bundle of more than a million fibers then passes information to the next relay station in the brain for sorting and integrating into further information processing channels. Figure 2.8 shows the calretinin-positive ganglion cell bodies in the GCL and their axons. The axon bundles, in the optic fiber layer, are visualized using an antibody to neurofilament protein. The bundles appear thicker when they are close to optic nerve.

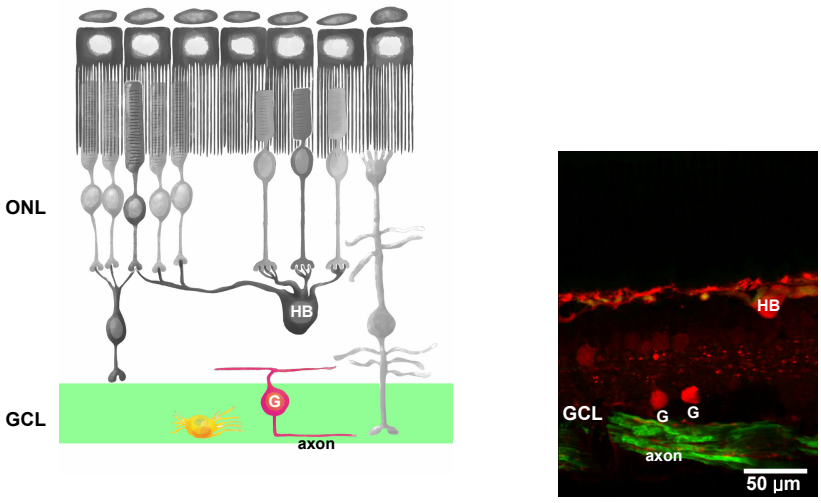

Figure 2.8: The ganglion cell layer (GCL). Left: a drawing* of retinal layers representing ganglion cells (G) and their axons. Right: a confocal image of retina labeled with antibodies to calretinin (red) and neurofilament (green). *The drawing is modified from Figure 1 in [27] (courtesy of Steve Fisher's lab).

2.1.9 Müller glial cells

The central nervous system consists of neurons and glial cells. Neurons constitute about half the volume of the central nervous system (CNS) and glial cells make up the rest. Glial cells provide support and protection for neurons. There are two basic types of glial cells in the cat and human retina: Müller cells and astrocytes. Müller cells are the principal glial cells of the retina. Müller cell bodies reside in the INL and project irregularly thick and thin processes in either direction to the OLM and to the inner limiting membrane (ILM) (M in Figure 2.9).

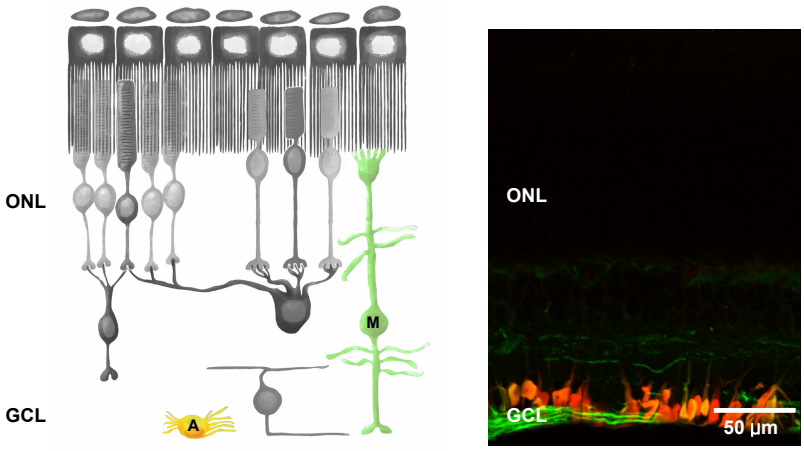

Figure 2.9: Glial cells: Müller cells and astrocytes. Left: a drawing* of retinal layers representing Müller cells (M) and astrocytes (A). Right: a confocal image of a normal cat retina labeled with antibodies to the interfilament proteins glial fibrillary acid protein (GFAP) (green) and vimentin (red). Intermediate filaments are concentrated in the endfoot region of the Müller cells with vimentin predominating over GFAP. *The drawing is modified from Figure 1 in [27] (courtesy of Steve Fisher's lab).

The OLM of the retina is formed from adherent junctions between Müller cells and photoreceptor cell inner segments. The ILM of the retina is likewise composed

of laterally contacting Müller cell endfeet and associated basement membrane constituents. Müller cells contain glycogen, mitochondria and the intermediate filament protein, vimentin and glial fibrillary acid protein (GFAP). The latter filaments are normally in the inner half of the Müller cells and their end feet (Figure 2.9), but following trauma to the retina such as retinal detachment, both vimentin and GFAP are massively upregulated and found throughout the cell.

2.2 Retinal Detachment & Reattachment

The degeneration of light sensitive photoreceptors accounts for the vast majority of blinding conditions in humans. One of the common causes is retinal detachment which can occur as a result of physical trauma or as a complication of disease. Retinal detachment is a fairly common physical injury involving separation of the neural retina from the underlying monolayer of pigmented epithelium (Figure 2.10).

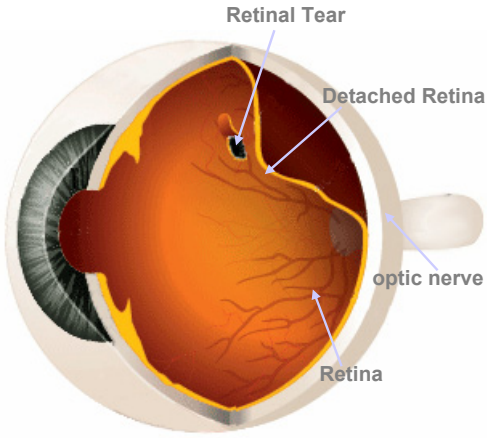

Figure 2.10: Retinal detachment. The image is modified from the original image in http://www.retinaconsultantsnj.com/images/detachment.jpg.

Because it can cause blindness in the affected area if left untreated, retinal detachment is considered an ocular emergency that requires immediate medical attention and surgery. With retinal reattachment surgery, over 90% of eyes with retinal detachment can be successfully treated. However, vision recovery is not always predictable. 20% to 37% of eyes with macular involvement recover visual acuity to 20/50 but other visual deficits commonly remain. The final visual result may not be known for up to several months following surgery. Even under the best of circumstances, and even after multiple attempts at repair, treatment sometimes fails and vision may eventually be lost. While surgical success is very high, much remains unknown about the degenerative processes that lead to visual defects, and little is understood about the biology of the regenerative process.

It has been a focus of research to understand the cellular changes that have the potential to significantly affect the return of vision after successful reattachment. A model system for retinal detachment in the cat has been developed by Steven Fisher's lab at UCSB [27]. As a model system for studying cellular remodeling in the retina due to injury, using retinal detachment as an injury model has some advantages; this system allows the study of the morphological, biochemical, and proliferative responses of the retina to trauma. Moreover, animal models provide precise control of the creation and location of the retinal detachment and it is also possible to create retinal detachments in multiple animals at many different time points, which is not possible in preserved human tissue. Figure 2.11 shows an experimental design for testing a hypothesis of the retinopathy of detachment and reattachment. Retinal detachments are experimentally created in one of the eyes of the animals. Briefly, the lens and vitreous are removed and a 0.25% solution of

sodium hyaluronate are infused via a glass pipette between the neural retina and the RPE. After a retinal detachment is created, various variables (e.g. hyperoxia) can be added depending on the proposed hypothesis. Following intervals such as 1, 3, 7, and 28 days of detachment, the animals are euthanized and the tissues are harvested, fixed and embedded for imaging techniques. For immunocytochemistry (see Section 2.3.3), the tissues are immersion fixed in paraformaldehyde and rinsed in phosphate buffered saline (PBS). The tissue is then embedded in low-melt agarose and sectioned at 100 μm with a vibratome®. Antibodies are added to label specific proteins in the tissue. Finally, images are collected by a confocal microscope. Analysis is done by comparing normal to detached retinas, and considering the differences between the antibody labeling patterns.

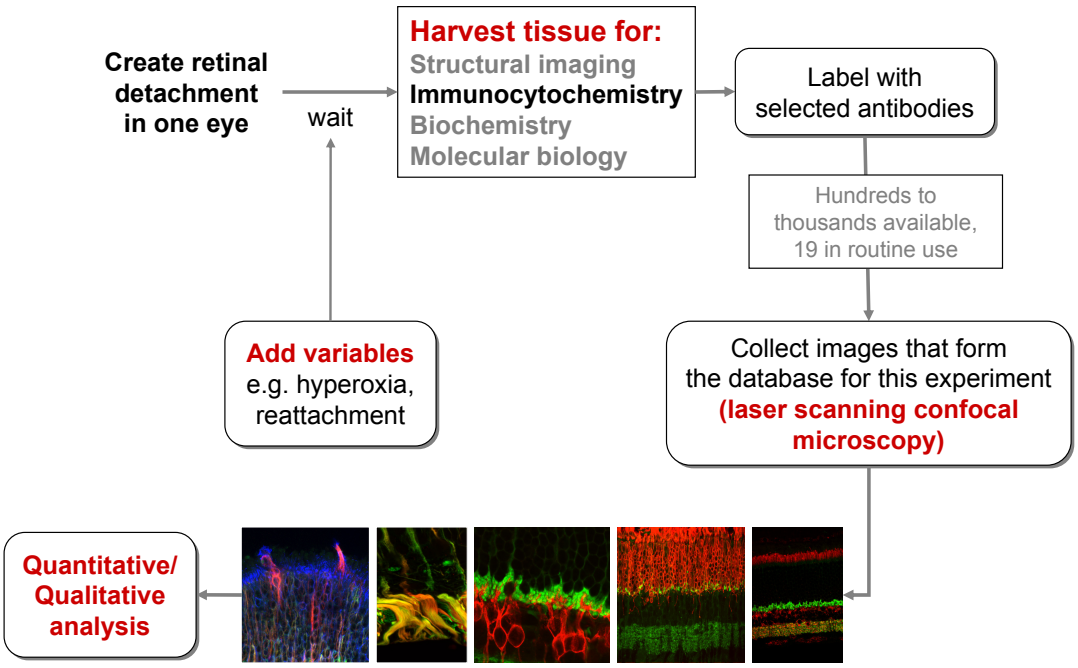

Figure 2.11: Experimental design for testing a hypothesis of the retinopathy of detachment and reattachment. (courtesy of Steven Fisher's lab, UCSB)

2.3 High Resolution Retinal Imaging

Recent advances in biological imaging and cytochemical labeling (e.g. fluorescent probes) have allowed for consistent, reliable ways of documenting changes in cell morphology and the expression patterns of specific proteins. Images have become critical components for a detailed understanding of the structure and function of cells and their proteins. More importantly, image processing is playing an increasing role in the analysis and understanding of quantitative biological experiments. A crucial aspect of research that is often overlooked is a full understanding of imaging techniques for quantitative analysis. Currently, vast quantities of images are generated to be analyzed by a human observer. The quality of images might be good for visual analysis but might not qualify for quantitative analysis. Image processing techniques that have been developed to deal with noisy images under traditional assumptions (e.g. image enhancement, segmentation, and restoration) should be re-evaluated before they are used in these types of images. It requires understanding of: the light source, the interaction of light with the desired specimen, the characteristics of modern microscope optics, and the characteristics of sensors. All of these components are important to achieve the accurate measurement of "analog" quantities given a digital representation of an image. Confocal imaging is a common method for determining cellular and subcellular patterns of a retina using confocal laser scanning microscopy (CLSM). Additionally, transmission electron microscope (TEM) and high resolution transmitted light microscopes are used, depending on the goal of the study. Each imaging technique reveals information about a tissue for different scales (from molecular to cellular) and resolutions (from nm to μm). In this section, we will

give a brief introduction of two imaging techniques, transmitted light microscopy and electron microscopy, and discuss confocal imaging in detail.

2.3.1 High resolution transmitted light microscopy

Transmitted light microscopy is one of the most commonly used and well known imaging techniques in biology. Most microscopes in current use are known as compound microscopes, where a magnified image of an object is produced by the objective lens, and the image is magnified by a second lens system (the ocular or eyepiece) for viewing. Thus, final magnification of the microscope is dependent on the magnifying power of the objective times the magnifying power of the ocular. Objective magnification powers range from 4x to 100x. This limitation is the result of light being diffracted by the object under observation and because diffracted light interferes with the image. Lower magnification is impractical on a compound microscope stand because of spatial constraints with image correction and illumination. Higher magnification is impractical because of limitations in light gathering ability and shortness of working distances required for very strong lenses. Ocular magnification ranges are typically ranging from 8x to 12x, and 10x oculars are most common. As a result, a standard microscope will provide a final magnification range of 40x up to 1000x and a pixel resolution of 0.2 μm. Light microscopy has been intensively used to study morphological changes that occur in the ONL and OPL after retinal detachment. Such morphological information is difficult to obtain using CLSM with immunocytochemistry. Figure 2.12 is an example image of a normal cat retina. Detailed structures of cell bodies and synaptic terminals are easily observed so that this figure can be used for compar-

ison to regions with a retinal detachment. Recent studies show that the antibody labeling of tissue sections with a transmitted light microscope can also provide precise quantitative information of structural remodeling of retinas.

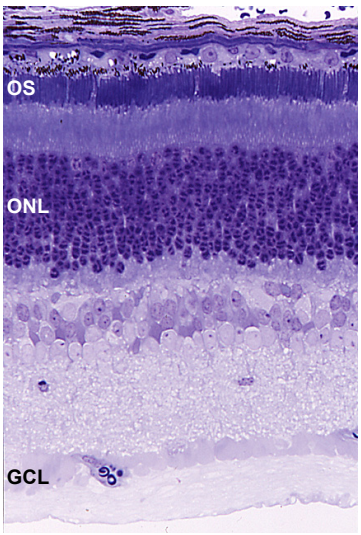

Figure 2.12: An example image of a vertical section through a cat retina. This is a normal cat retina embedded in Spurs resin and sectioned at 1 μm thickness using an LKB ultramicrotome. It was then counterstained with Toluidine blue and photographed with Ektachrome 64 slide film. The slide was then scanned to create a digital image.

2.3.2 Transmission electron microscopy

The electron microscope (EM) was developed to overcome the limitations of light microscopes which are limited by the physics of light, a maximum of 1000x magnification, and a resolution of 0.2 μm. In the early 1930's this theoretical limit had been reached and there was a scientific desire to see the fine details of the interior structures of organic cells. This required 10,000x plus magnification which is not possible using light microscopes. The transmission electron microscope (TEM) is the first type of electron microscope to be developed and is

patterned exactly on the transmitted light microscope except that a focused beam of electrons is used instead of light to "see through" the specimen. The resulting electron micrographs (EM) are very useful in understanding the structure of a retina and its cellular responses at nanometer resolution. Figure 2.13 shows an example of outer segments of rod photoreceptors by TEM and CLSM.

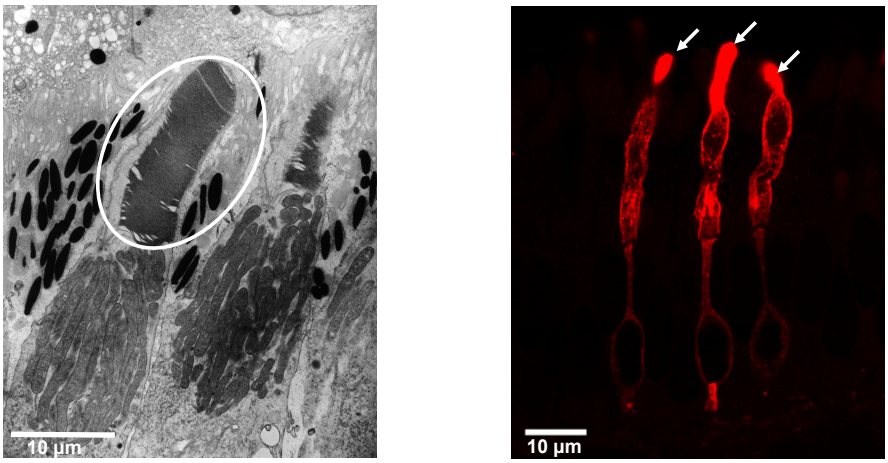

(a) (b)

Figure 2.13: Example image of transmitted electron microscope. (a) The outer segment of rod photoreceptors (circled region). The image is scanned with 300 dpi from TEM negative with 5000x magnification. (16.934 nm/pixel). (b) Example of single labeled image of rod photoreceptors collected with a confocal microscope (158 nm/pixel). Outer segments are denoted as arrows.

Outer segments in confocal images (Figure 2.13 (b)) display high concentration of rod opsin as solid regions, on the other hand, those of electron micrographs (Figure 2.13 (a)) reveals the morphological structure filled with stacks of membranes containing the visual pigment molecules such as rod opsin. While electron micrographs provide high resolution images, it is often challenging to extract accurate structural information from specimen images that are obscured with a granular noise. Additionally, an advanced imaging technique called electron tomography

allows the reconstruction of subcellular organelles and cells at nanometer resolution from collected projections of an object. The technique calculates a 3-D structure from many 2-D images or projections recorded over a wide range of tilt angles.

2.3.3 Confocal laser scanning microscopy

CLSM is a relatively new light microscopic imaging technique which has found wide applications in the biological sciences. The primary value of a confocal microscope is its ability to create optical sections through a 3-D specimen that would otherwise appear blurred when viewed with a conventional microscope. This is achieved by excluding most of the light from out-of-focus points of the sample. The image contains information from only one focal plane; therefore, by moving the focal plane through the depth of a specimen, a series of optical sections called z-series can be collected (Figure 2.14 (a)). The stack of serial optical sections can be viewed as a composite projection image which is commonly computed by the maximum projection of 3-D image stacks (Figure 2.14 (b)). Moreover, it is possible to reconstruct 3-D volumetric representations by assembling a stack of 2-D images along the vertical axis (i.e. z direction). This property of the CLSM is fundamental for solving 3-D biological problems where information from regions distant from the plane of focus can obscure the image (thick objects such as brain or retina). Figure 2.14 (a) shows the series of optical sections of a cross section of a cat retina. A cross section can be viewed from a vertical section of retina. Individual planes readily reveal the structure of cone photoreceptors with a lateral resolution of 1 μm.

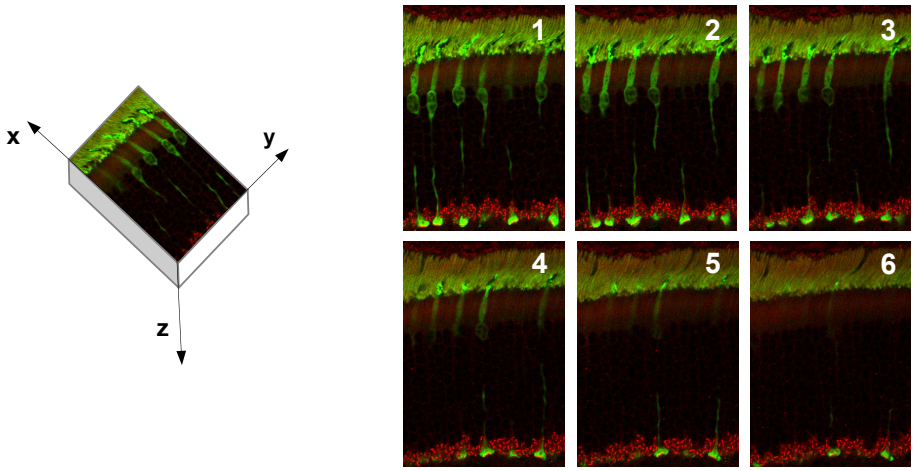

(a)

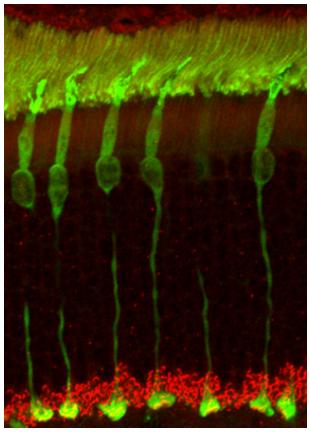

(b)

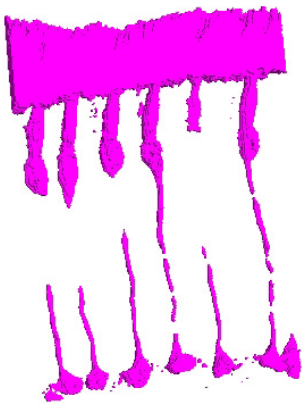

(c)

Figure 2.14: Optical section z-series of cone photoreceptors. (a) Six series of optical sections of the cross section of cat retina. The tissue is labeled with antibodies to synaptic ribbon protein C-terminal binding protein 2 (CtBP2) (red) and PDEγ (green). (b) A projection image of six optical sections reveals the structure of cone photoreceptors. (c) Volume rendered 3-D representation generated by software [25].

The projection image and 3-D reconstruction image of the selected cone photoreceptors are shown in Figure 2.14 (b) and (c). Moreover, the series of optical sections of a wholemounted cat retina can be collected. A wholemount can be viewed from either surface of a retina (RPE or ILM) and then optically sectioned to visualize a particular cell or layer. Figure 2.15 (b) shows the INL illustrating two different types of horizontal cells (Section 2.1.6) with many branched dendrites and axons.

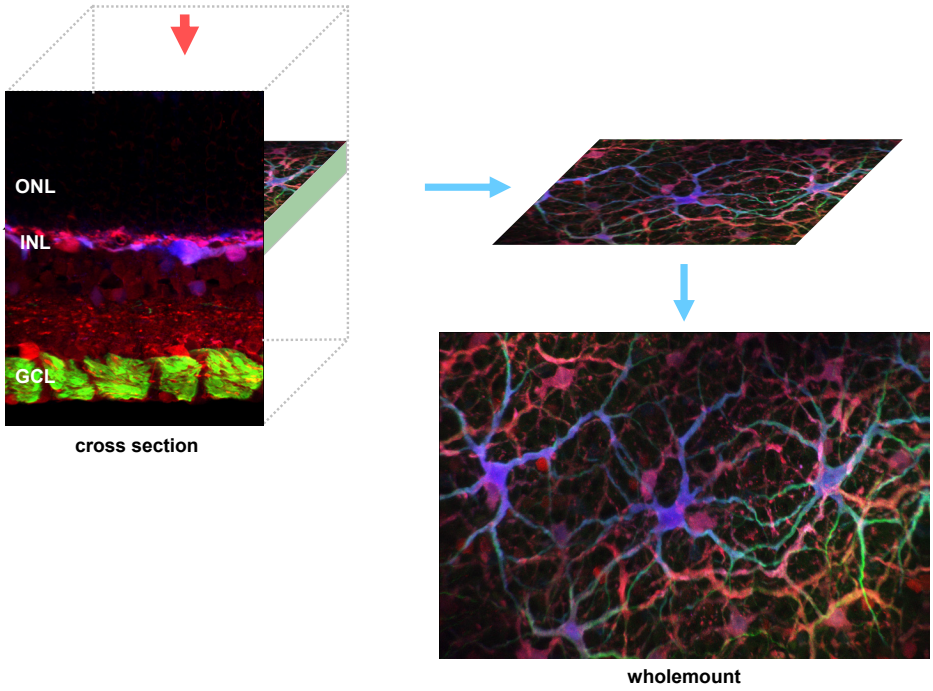

Figure 2.15: Example retinal images from cross section and wholemount of a retina. Images are labeled with antibody to calretinin (red), neurofilament (green), and calbindin D (blue). A retinal section can be viewed from a vertical section of retina illustrating all layers. On the other hand, a retinal wholemount can be viewed from either surface (RPE or ILM) and then optically sectioned for visualizing a specific layer, here horizontal cells in the INL.

Antibody labeling

Cells are mostly transparent in their natural state and the immense number of molecules that constitutes them are not optically distinguishable from one another. However, if a marker is attached to the protein of interest, it will very precisely indicate its position. Much effort has gone into finding suitable markers for this purpose. When Coons and Kaplan introduced a technique to label antibodies with a fluorescent dye to study antibody-antigen interactions, it profoundly changed the field of immunocytochemistry. In the case of antibodies, the indirect antibody technique is used frequently. First, the primary antibody that is targeted against a specific protein is added to the tissue (Figure 2.16). This molecule is not conjugated to a fluorochrome since this modification can reduce its binding efficiency to the antigen. To detect the primary antibody, a secondary antibody that is conjugated to a fluorochrome is added. This secondary antibody binds specifically to the primary antibody. Since several molecules can bind to one primary antibody molecule, there are now several dye molecules per target. Thus, the fluorescent emission arising from one primary antibody is amplified by the secondary antibodies that bind to it. The fluorochrome conjugated to the secondary antibody determines the color of the image stained by this indirect antibody staining protocol. That is, the tissue stained with the antibody is collected as a pseudo colored image.

Immunocytochemistry (labeling by antibodies) has been used to visualize a specific cell shape and protein distribution in the tissue. Similarly, the technical advantages of immunocytochemistry have permitted the discovery of remodeling events in the retina in recent years. Different antibodies or antibody combinations

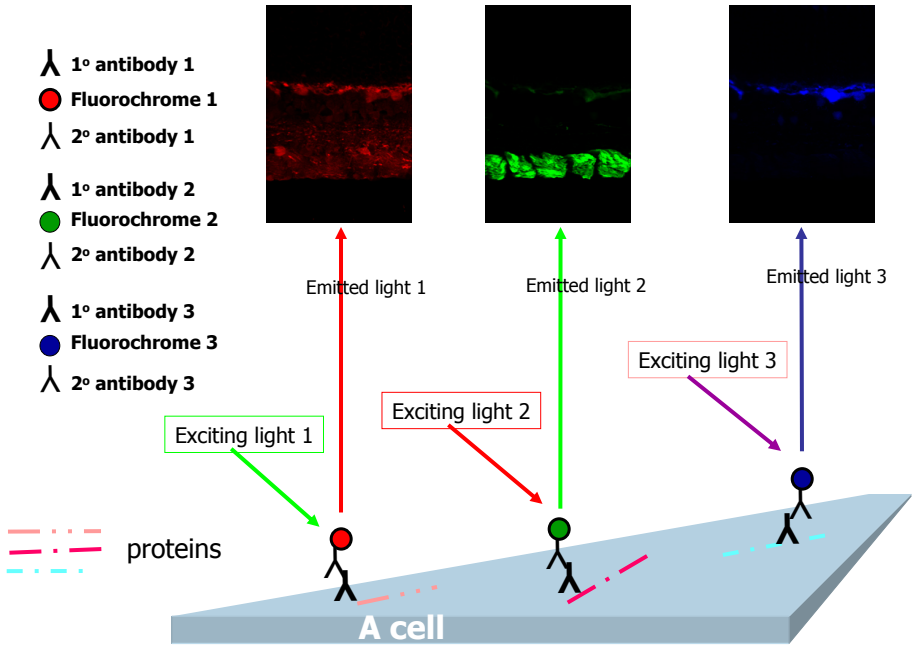

Figure 2.16: Indirect antibody staining technique. The primary antibody is added to the tissue. This molecule is targeted against a specific protein. A secondary antibody that is conjugated to a fluorochrome is added to detect the primary antibody. When the light of one wavelength (e.g. excited light 1) excites the dye (fluorochrome 1), protein is labeled by attaching fluorochrome so that they will emit the light of one wavelength (e.g. emitted light 1).

provide information about specific cell types and their reaction to retinal injury (Figure 2.17). It is also critical to identify and correlate changes in antibody labeling with the ultrastructural images. Figure 2.18 (a) shows an example of two proteins which are localized to a specific region in normal cells. The intensity of labeling with these antibodies (i.e. protein expression profile) and the pattern of their localization shifts dramatically when the retina is detached. The example in Figure 2.18 (b) shows cone photoreceptors. The intensity of labeling is decreased and the shape of the cone terminal, denoted by arrows, is changed in response to detachment.

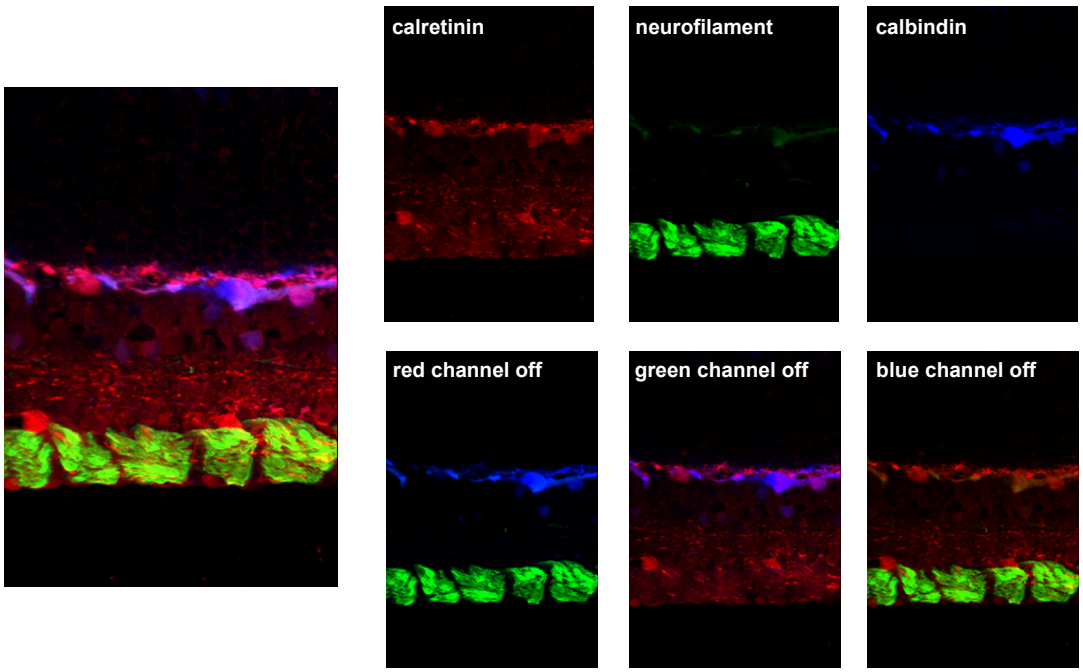

Figure 2.17: Example retinal section labeled with three antibodies. Information from each channel can be extracted separately.

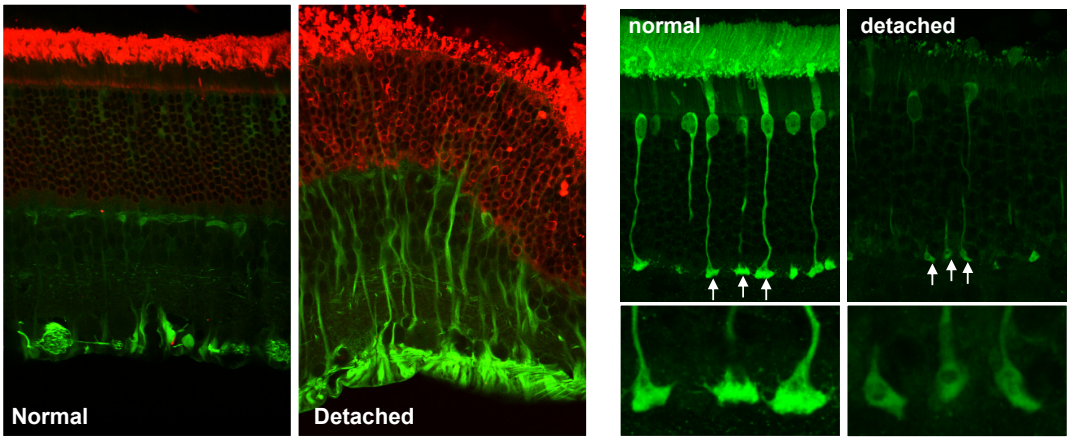

(a) (b)

Figure 2.18: Example data collection of immunofluorescence images of feline retina. (a) Example of double labeled images of rod photoreceptors (anti-rod opsin; red) and Müller cells (anti-GFAP; green) (b) Example of single labeled images of cone photoreceptors (anti-PDEγ).

Problems and limitations of confocal microscopy

It is known that CLSM is easy to use and its images reveal the location of labeled molecules in tissues. Over the past several years, confocal microscopy has become a quantitative tool. There are a number of aspects we should take into account to obtain accurate measurements from these fluorescent micrographs. Problems and limitations of confocal microscopy have appeared in the literature. We describe some of them which are crucial to quantitative image analysis of retinal tissues.

Signal-to-Noise: optical shot noise In CLSM the signal levels are typically low, only 10-20 photons/pixel in the brightest area, due to the limited amount of light obtainable from the small fluorophore probe volume in the focussed beam. Under such conditions, statistical variation in the number of detected photons is the most significant variable. The uncertainty in intensity determination caused by such shot noise results in an overall reduction in contrast. Furthermore, the level of noise relative to the signal determines the number of gray levels that can be distinguished in an individual image pixel, which in effect establishes a limit on the dynamic range of the image. The intrinsic statistical variation in the detected photon signal is governed by a Poisson distribution function. Such a distribution has the property that its mean value is equal to its variance. For a signal consisting of n photons, the signal-to-noise ratio is given by:

$$\text{Signal-to-Noise (S/N)} = \frac{n}{n^{1/2}} = n^{1/2}.$$

Note that the intensity of noise is proportional to the intensity of the fluorescence signal. Therefore, traditional assumptions about the relationship between signal and noise do not hold as presented in [84]: 1) the noise is *not* independent of the signal; 2) the noise is *not* Gaussian; and 3) the noise is *not* additive.

Signal-to-Background: background shot noise In an ideal microscope, only the optical shot noise limits the image quality. In an actual microscope, the presence of background shot noise must also be considered and is added to the noise component in the relationship between signal and noise. If the background contribution is large (small signal-to-background ratio), the desired signal may become lost in the high background shot noise, resulting in a signal-to-noise ratio approaching zero. For example, each confocal retinal image is generated to visualize a specific protein. Since only specific regions where fluorescent dye molecules bind are visualized, most regions in the tissue appear as dark regions whose intensity levels are close to zero or sometimes below the background noise level. In order to extract features from such regions, contrast enhancement techniques (e.g. histogram equalization) are often employed. Contrast enhancing for a region with high background noise will amplify the noise, resulting in poor feature extraction and image segmentation.

Resolution As with conventional microscopy, confocal microscopy has inherent resolution limitations due to diffraction. The width of the point spread function of intensity profiles are indicative of the microscope resolution– the best lateral resolution is typically about 200 nm. Images with higher

resolution than 200 nm are usually collected by a digital zoom, that is, interpolation.

Axial thickness of optical sectioning We saw one of the advantages of confocal microscopy is optical sectioning. The axial thickness of optical sections depends on the inverse square of the numerical aperture (NA). For example, with good oil immersion lenses (with a highest NA of 1.4), the optical sections can be collected with a resolution up to 0.5 μm. Therefore, pixel size in the z-direction will be larger than the xy-direction leading to a challenge in computing features in 3-D. For example, small structures such as synaptic ribbons in the photoreceptors are difficult to capture through multiple optical sections.

Photobleaching It is commonly believed that increasing the laser intensity will increase signal intensity. In fact, only a fraction of the light is needed to maximally excite fluorophores in confocal microscopy. The remaining light will lead to quenching of the fluorophores, heating of the cell, and photo-oxidative damage to the cell. This is a crucial problem in live cell imaging applications. In fixed cell imaging like retina, photobleaching will also occur when collecting serial optical sections. This causes intensity variations among the series of the optical sections.

Intensity variation by uneven staining An additional consideration is that fluorescence intensity usually is not even across the tissue section, because labeled structures are not uniformly distributed within the tissue or individual cells. In addition, antibodies and many other probes cannot penetrate

far into tissues. When a tissue is not flat, for example, a detached retina, the intensity variation is more significant. It is often necessary to change the laser intensity, or gain, to bring out detail in a particular area of interest, even though other regions of the cell or tissue are obscured in that image. Such variation is more dramatic across serial optical sections. For example, if the sections are to be collected through a depth of more than 5-10 μm to capture the neuronal processes of bipolar cells in the retina, adjacent series of several microns each may have to be collected, so that gain can be adjusted. Note that the intensity of the image is no longer accurate quantitative information.

There are other variables including autofluorescence, spectral bleed-through artifacts, different types of noise (e.g. dark current), tissue degradation [52] and the particular microscope configuration under consideration. It is desirable to optimize images during collecting to cope with these problems so subsequent image processing can be minimized. However, what is done with images after they are collected is as important as how they are collected. With an understanding of the addressed issues, we can extract *meaningful* and *accurate* quantitative information from properly processed images. Since signal and noise are not independent, we need an adaptive image processing method depending on the level of signal and background noise. More details will be discussed in the following chapters.

2.4 Image Analysis for Retinal Cell Biology

So far, we have described various imaging techniques. In this section, we present biological problems that have been asked to study retinal detachment and reattachment followed by associated image analysis issues, and unique challenges in processing retinal images.

A number of questions have been asked to understand the mechanism behind the loss and recovery of vision following retinal detachment and reattachment over the last several decades. The main research problems in biology of the detachment can be summarized as shown in Figure 2.19.

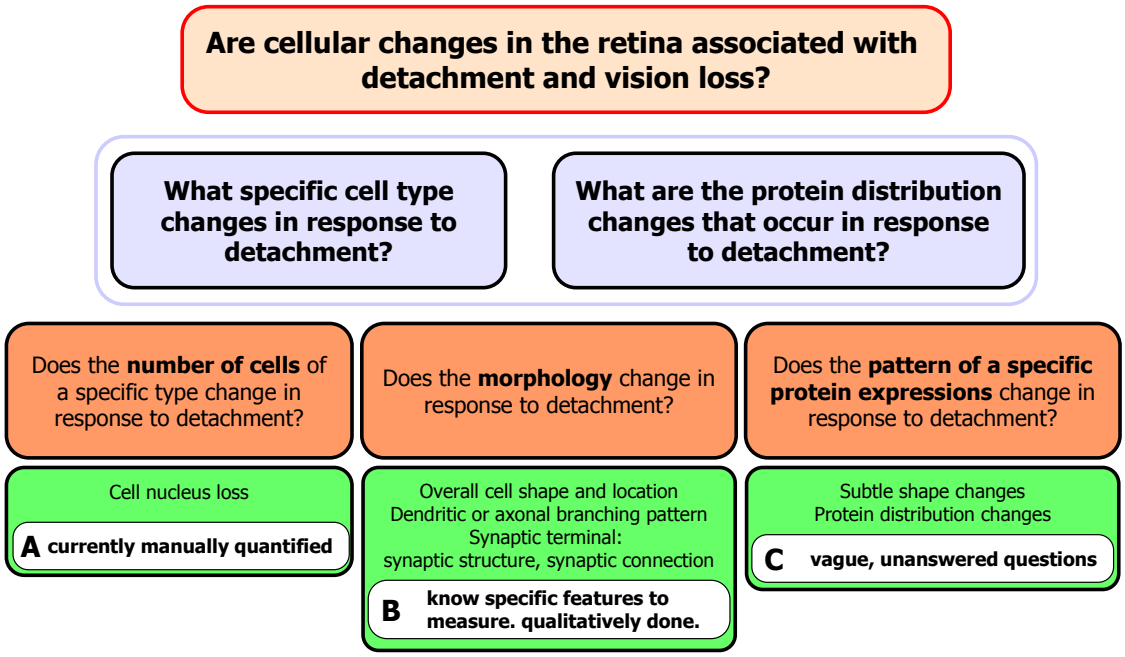

Figure 2.19: Biological questions about a model system for retinal detachment.

The main problem is refined until the problem is specific for the experimental design phase. A hypothesis that addresses the experimental question is then for-

mulated, and the experiment is designed. Thus, to understand the events initiated by retinal detachment, the ultimate question is if there are cellular changes in the retina associated with detachment (Highest level question in Figure 2.19). This question leads us to ask more specific questions. For example, if there are cellular changes in the retina, what type of cell type changes (a question at the second level in Figure 2.19). To answer this question, a hypothesis is proposed (e.g. Photoreceptors are changed) and in turn, a corresponding experimental question is asked such as "does the number of photoreceptors change in response to detachment?". To explore the answer to this question (whether the number of photoreceptors is changed), the experiment is designed as shown in Figure 2.11. In this example, the tissue is stained with a nuclear dye and images are collected by confocal imaging. The number of photoreceptors within the ONL is then counted.

The experimental questions can be summarized into three categories. The first group of questions (denoted A in Figure 2.19) are currently answered by manual quantification. Figure 2.20 shows an image set to answer one example experimental question type A: "Does the number of photoreceptors change in response to detachment?"

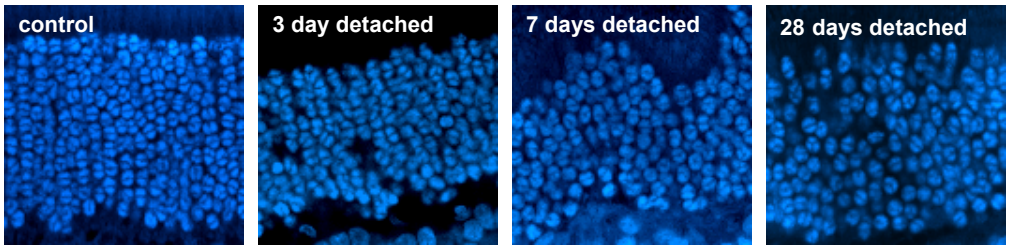

Figure 2.20: Confocal images of the ONL from normal and detached retinas stained with the nuclear dye, TO-PRO. After detachment, the photoreceptor layer appears to be much more loosely packed with nuclei than the control attached tissue.

Retinal detachment usually causes death of some photoreceptors and a thinning of the ONL. The thickness of the ONL and the number of cells in the ONL are two main features to answer the above question. Previously it has been shown that the number of photoreceptors decreases after detachment. The thickness of the ONL is measured using a microscope and the number of cells within the ONL are counted manually. In order to obtain statistically valid observations, many images should be collected from different samples and different animals. Unfortunately, the number of samples needed for analysis is often limited. Even if the samples are available, this is very time consuming and hardly feasible. For example if a 40x magnification oil immersion lens is used, a 2-D sampling region with dimensions of about 300 μm$\times$10 μm can be used for counting cells assuming that the image size is 512$\times$512 pixels. For the retina of area 1385 mm^2, since the total retina is a circular disc of approximately 42 mm diameter, each region thus represents a fraction of $1/2,000,000,000^{\text{th}}$ (a two billionth) of the whole retina. Usually manual analysis requires counting the tiny fraction of the retina and extrapolating the total number cells in the whole retina. Moreover, the question that is currently answered by manual analysis is repeated routinely. For example, Fisher's group already manually measures the thickness of the ONL and the number of photoreceptors within the ONL from normal and detached cat retinas. If an experimental condition is changed such as an interval of detachment (e.g. 56 days detachment) or species (mouse or ground squirrels), the cell number within the ONL and thickness of the ONL should be measured from vast amounts of new tissues. An automated quantifying approach can reduce this tedious manual measurement of such large data sets and also improve quality by reducing inter-

observer variation. We have developed an automated nucleus detector currently used for measuring the number of cells from cat and mouse retinas under various conditions (see Chapter 5).

The second group of the questions (denoted B in Figure 2.19) are currently answered by qualitative analysis. Figure 2.21 shows a series of retinal images labeled with an antibody to rod opsin. This experimental image set is generated to answer the experimental question: "Does the pattern of rod opsin protein expression change in response to detachment?" The deconstruction of the rods involves a number of other characteristic responses to detachment. One response is the 'redistribution' of rod opsin molecules in the plasma membrane that surrounds the inner portions of the rod photoreceptors (in the ONL). Localization, level of protein expression, and the pattern of rod opsin protein distribution are the main features to interpret this image set. The images are usually analyzed in a qualitative manner and the analysis result is described with images.

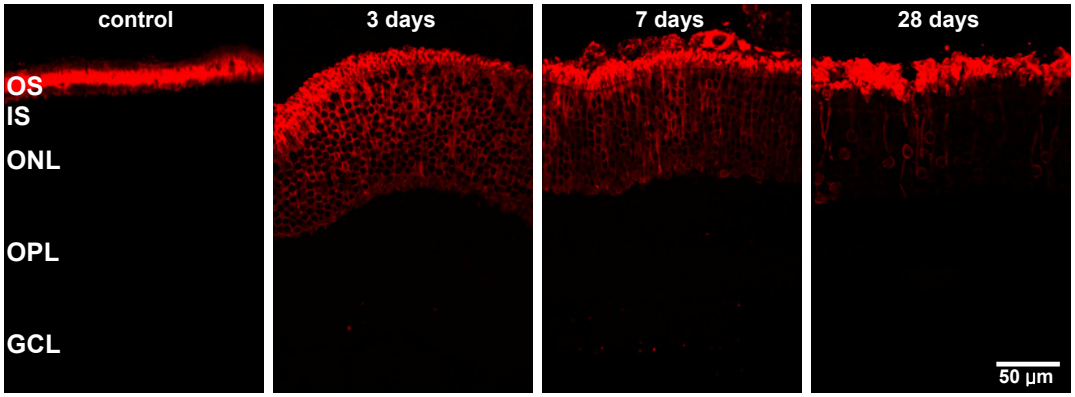

Figure 2.21: Confocal images of retinas immunolabeled with antibody to rod opsin (red). (a) Normal retina. Anti-rod opsin labeling is restricted to the OS. (b) 3-day detached retina. Anti-rod opsin labels the truncated OS and rod cell bodies in the ONL. (c) 7-day detached retina. (d) 28-day detached retina. Anti-rod opsin labels OS fragments as well as rod cell bodies in the ONL.

However, qualitative differences between two samples are often characterized using vague parameters such as "texture", "fuzziness", "shape", or "somewhat flattened appearance" [43]. It can be difficult to quantitatively measure such qualitative observations. On the other hand, image analysis methods can provide quantitative information based on identified specific features for a measurement. Moreover, quantitative analysis can extract *new* information that can not be captured by traditional manual quantitative/qualitative analysis. The questions in the third group denoted by C in Figure 2.19 are the most complicated questions; they can be answered as 'yes' or 'no' yet the answer can not be described quantitatively. For example "Does the expression pattern of a specific protein change in response to detachment?", if the pattern changes, how the pattern changes is challenging to describe even qualitatively. In particular, one must identify vague verbal descriptions of the biological characteristics that need to be translated into measuring image features. Image analysis and informatics methods cannot solve all the questions, but can provide more information about such complex problems so that we can have more insight.

To quantify the addressed biological problems and aid in the understanding of the events initiated by retinal detachment, the image analysis task can be summarized as follows:

- **Identifying patterns of cellular/subcellular protein distribution**

  All problems in experimental question type A and B in Figure 2.19 can be answered by detecting the patterns, and more specifically cells and layers. This is basically a *segmentation* problem, which is a mandatory step for image analysis. We are mainly focused on segmentation of biologically

meaningful objects (e.g. photoreceptor nuclei and synaptic terminals) and retinal layers (e.g. ONL).

- **Changes in these patterns**

  Once we have segmented objects/layers, we can extract multiple levels of features ranging from low-level features (e.g. intensity and texture) to high-level features (e.g. nuclei density, inter-layer relations, and inter-cell relations). These features need to be linked to biologically meaningful information for characterizing the changes after retinal injury. It will help to answer the questions of type B and C in Figure 2.19.

An ideal image analysis tool should have the pattern recognition abilities of a human and the fast and accurate evaluation of the computer to: allow feature based representation, discover non-obvious pattern/relationships, and support complex questions (e.g. question type C in Figure 2.19). Ultimately this can lead to the discovery of interesting and useful patterns from data by modeling events associated with retinal detachment. As will be discussed in Chapter 4, we demonstrate that information extracted by an image analysis from a single set of images provides not only corroborate conclusions derived from manual measurement and qualitative analysis, but also offers new insights.

2.4.1 Image analysis challenges

The nature of retinal tissue makes the problems addressed in the previous section challenging tasks. Note that we are only focusing on retinal images that are stained with antibodies and collected with CLSM.

- **Segmentation**

  - Heterogeneity in morphology between objects/regions: image data in an individual region (e.g. layer) is not statistically homogeneous information. This is one of the fundamental problems in segmenting micrographs. Further difficulties in retinal images include visual variation from staining. For example, the same layer can show different structures depending on probed antibodies. (Figure 2.22).

- **Object representation and feature selection**

  - Intrinsic variance between samples: another demanding element is the intrinsic variance between samples. Any biological system exhibits significant variations. For example, Figure 2.18 (b) shows cone photoreceptors. The shape of the terminal under the same condition displays high variance without clear landmarks to distinguish the shape of one condition from that of others. Unfortunately, the sample tissues available for imaging are limited so it is practically impossible to collect enough images to cancel out noise and variance between samples under the same conditions. It is crucial to extract robust features that capture common characteristics from the images under the same conditions in spite of the variance, yet have the capacity of discriminating subtle variation among images from different conditions.

  - Subtle domain specific differences across the samples from various conditions: There are subtle but critical changes that may not be distinguished by eye or may be difficult to describe. Figure 2.23 shows confocal images of 3 day and 7 day detached retinas illustrating the changes of intermediate filament proteins within Müller cells (GFAP and vimentin).

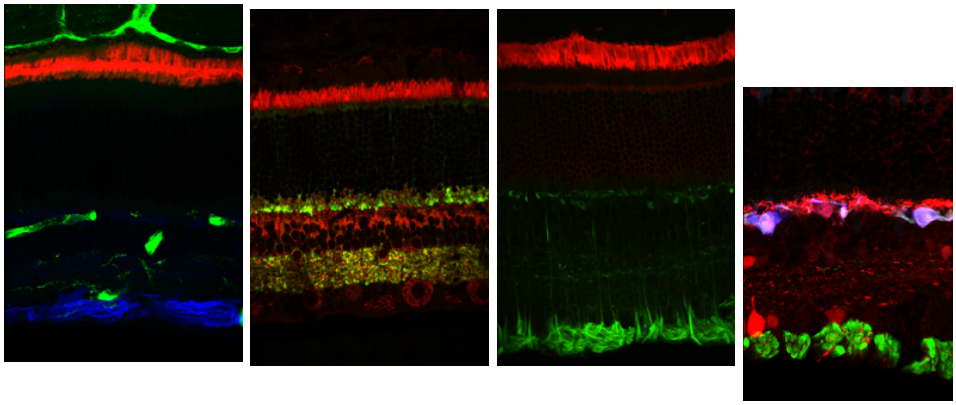

(a)

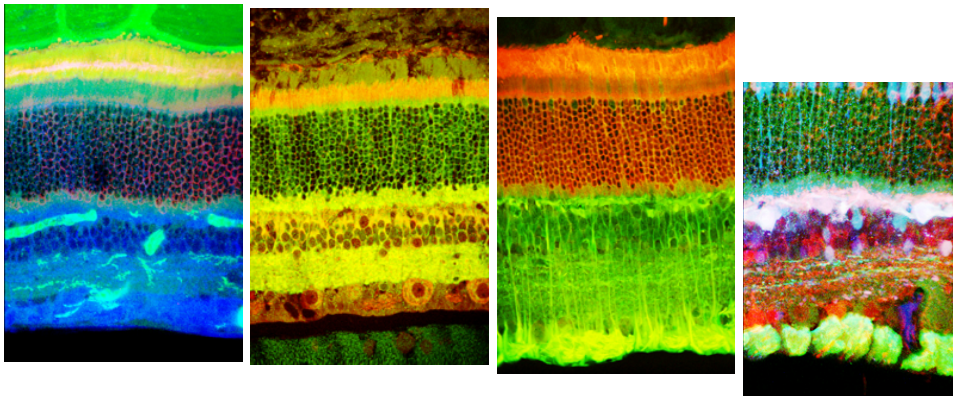

(b)

Figure 2.22: Example of representative images of retinal sections with different combinations of antibodies and from different locations. The same layer shows a different structure depending on the antibody used. (a) Representative image of normal retina section with different combinations of antibodies and from different locations. (b) Histogram equalized images of (a).

- Subtle domain specific differences across the samples from various conditions: There are subtle but critical changes that may not be distinguished by eye or may be difficult to describe. Figure 2.23 shows confocal images of 3 day and 7 day detached retinas illustrating the changes of intermediate filament proteins within Müller cells (GFAP and vimentin).

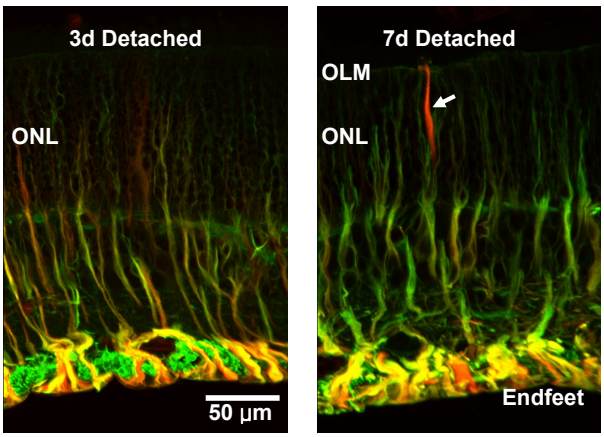

Figure 2.23: Confocal images of 3-day and 7-day detached retinas stained with two antibodies (anti-vimentin ; red, and anti-GFAP; green). After 7 days of detachment, the intermediate filament cytoskeleton is showing more growth from the endfeet compared to that after 3 days of detachment. These processes grow into subretinal space (denoted by a white arrow) and form a scar.

After 7 days of detachment, GFAP and vimentin labeling has increased particularly in the ONL. Müller cell processes that grow into the subretinal space (OLM) form a scar (denoted by an arrow in Figure 2.23) which predominantly labels with an antibody to vimentin. Such changes are difficult to describe without expertise. Even with expertise, it is more challenging to identify the difference between two images without knowing the condition of the tissue. Image analysis or data mining usually requires us to determine relevant features in an ad hoc manner. The relevant features of the data set can be determined by the already confirmed hypotheses, however,

we may not be very sure of the proposed hypothesis. Thus identification of new features is not always clear because of the complexity of underlying biological information. Feature selection should be done automatically instead of selecting features ad hoc. The ultimate goal in feature selection is not classification. Class information in a retinal image dataset, for example, species (cat, mouse, and squirrel) and experimental information (normal,n-day detachment, reattachment), are usually provided by metadata stored in a database with the images. Our goal is to characterize the underlying biological processes using the selected features. The classification can be used for prediction and understanding; the value of classifiers that produce an estimated probability for each class is apparent in their potential for interpretation as an index of structural integrity of a retina after detachment. The classification tree has a potential to link features from an image to biologically meaningful information.

- **Spatial-temporal modeling**

  - Observations cannot take place on the same sample over time: images are collected from retinal sections/wholemounts at intervals of one day after retinal detachment, 3 days, 7 days, and 28 days. Coupled with technical variabilities in sample preparations and image acquisition, the underlying image representation becomes heterogeneous.

- **Lack of data**

  Since every data set is generated for answering specific experimental questions to prove/disprove a proposed hypothesis, it usually consists of a relatively small number of images from various conditions. Each data set may

require different features depending on the hypothesis. It is a challenge to combine each result from various experiments to discover interesting patterns over all data. Additionally, single plane images extracted from z-series are redundant. Thus, maximizing the amount of information attainable from a single sample is very important.

2.5 Summary

We provided an overview of structure and function of the retina, and discussed imaging techniques with related signal/image processing challenges. We also presented how different imaging techniques reveal different information about the same retinal tissue. Retinal images are very complex and rich in information, increasing both the difficulty as well as the potential for image analysis and data mining. Biological problems which have been studied for several decades for understanding events associated with retinal detachment lead us to two main image analysis problems: identifying cellular and subcellular patterns, and characterizing changes in these patterns. There are several challenges associated with the unique nature of immunofluorescence retinal images. In the following chapters, we propose image analysis methods to cope with such challenges.

References

Retinal cell biology

- H. Kolb, E. Fernandez, and R. Nelson. WEBVISION:The Organization of the Retina and Visual System, 2005. http://webvision.med.utah.edu/. Last visited: Mar 27th, 2007.

- D. M. Paskowitz, G. Nune, D. Yasumura, H. Yang, R. B. Bhisitkul, S. Sharma, M. T. Matthes, M. A. Zarbin, M. M. LaVail, and J. L. Duncan. BDNF Reduction of Retinal Toxicity of Verteporfin PDT. *Investigative Ophthalmology and Visual Science*, 45(11):4190.4196, 2004.

- J. J. Michon, Z. Li, N. Shioura, R. J. Anderson, and M. O. M. Tso. A Comparative study of Methods of Photoreceptor Morphometry. *Investigative Ophthalmology and Visual Sciences*, 32(2):280.284, 1991.

Retinal detachment

- B. Cook, G. P. Lewis, S. K. Fisher, and R. Adler. Apoptotic photoreceptor degeneration in experimental retinal detachment. *Investigative Ophthalmology and Visual Science*, 36(6):990.996, 1995.

- D. Anderson, W. Stern, S. Fisher, P. Erickson, and G. Borgula. Retinal detachment in the cat: the pigment epithelial-photoreceptor interface. *Invest Ophthalmol Vision Science*, 24:906.926, 1983.

- P. A. Erickson, S. K. Fisher, D. H. Anderson, W. H. Stern, and G. A. Borgula. Retinal detachment in the cat: The outer nuclear and outer plexi-

form layers. *Investigative Ophthalmology and Visual Science*, 24(7):927.942, 1983.

- S. Fisher, P. Erickson, G. Lewis, and D. Anderson. Intraretinal proliferation induced by retinal detachment. *Invest Ophthalmology Vision Science*, 32:1739.1748, 1991.

- S. K. Fisher, G. P. Lewis, K. A. Linberg, and M. R. Verardo. Cellular remodeling in mammalian retina: results from studies of experimental retinal detachment. *Progress in Retinal and Eye Research*, 24:395.431, 2005.

- G. Lewis, K. Linberg, and S. Fisher. Neurite outgrowth from bipolar and horizontal cells after experimental retinal detachment. *Invest Ophthalmology Vision Science*, 39:424.434, 1998.

- G. P. Lewis, D. G. Charteris, C. S. Sethi, and S. K. Fisher. Animal models of retinal detachment and reattachment: identifying cellular events that may affect visual recovery. *Eye*, 16(4):375.387, 2002.

- K. Mervin, K. Valter, J. Maslim, G. Lewis, S. Fisher, and J. Stone. Limiting photoreceptor death and deconstruction during experimental retinal detachment: the value of oxygen supplementation. *American Journal of Ophthalmology*, 128(2):155.164, 1999.

- T. Sakai, J. B. Calderone, G. P. Lewis, K. A. Linberg, S. K. Fisher, and G. H. Jacobs. Cone photoreceptor recovery following experimental detachment and reattachment: an immunocytochemical, morphological, and

electrophysiological study. *Investigative Ophthalmology and Visual Science*, 44:416.425, 2003.

High resolution imaging and quantitative analysis

- C. Vonesch, F. Aguet, J. L. Vonesch, and M. Unser. The colored revolution of bioimaging. *IEEE Signal Processing Magazine*, 23(3):20.31, May 2006.
- I. T. Young. Quantitative microscopy. *IEEE Engineering in Medicine and Biology*, 15(1):59.66, 1996.
- J. B. Pawley. The 39 stpes: A cautionary tale of quantitative 3-d fluorescence microscopy. BioTechniques, 28(5):884.887, 2000.
- R. W. Marc, B. W. Jones, C. B. Watt, and E. Strettoi. Neural remodelling in retinal degeneration. *Progress in Retinal and Eye Research*, 22:607.655, 2003.

Electron tomography

- National center for microscopy and imaging research (NCMIR). http://www.ncmir.ucsd.edu/. Last visited: Aug 25th, 2006.
- J. Frank. Electron Tomography: Three-Dimensional Imaging with Transmission Electron Microscope. Springer, 1992.

Confocal microscopy

- Theory of confocal microscopy: Singal-to-noise considerations. http://olympusfluoview.com/theory/signaltonoise.html. Last visited: Oct 05th, 2006.

- A. Boyde. Bibliography on confocal microscopy and its applications. Scanning, 16:33.56, 1994.

- C. M. S. Croix, S. H. Shand, and S. C. Watkins. Confocal microscopy: comparisons, applications, and problems. *BioTechniques*, 39(s):2.5, 2005.

- B. Matsumoto. Methods in Cell Biology (Volume 70). Academic Press, 1993.

- M. Minsky. Memoir on inventing the confocal scanning microscope. *Scanning*, 10(4):128.138, 1988.

- J. B. Pawley. The 39 steps: A cautionary tale of quantitative 3-d fluorescence microscopy. *BioTechniques*, 28(5):884.887, 2000.

- J. B. Pawley. Handbook of biological confocal microscopy. Plenum Press, 1990.

- D. Semwogerere and E. R. Weeks. Bibliography on confocal microscopy and its applications. *Encyclopedia of Biomaterials and Biomedical Engineering*, 1(1):1.10, 2005.

Chapter 3

Background of Image Analysis & Pattern Recognition

Most of the work in biomedical image analysis has focused on the segmentation and visualization of macro biological structures such as tissues, organs and bones [62, 19, 22, 67]. On the other hand, an approach using *micro* biological structures (e.g. cellular or subcellular organism) is still in its infancy. Segmenting a micrograph is often more challenging than segmenting medical images, since much less heuristics can be made about the signal intensities or the shape of the object [62]. This characteristic discriminates microscopic image analysis from most of the classical medical image analysis that can use prior knowledge of anatomical structure to improve segmentation and visualization of macro biological structures. Hence algorithms developed for micrograph analysis have been very task specific.

In this chapter, we provide a brief background of the image analysis and pattern recognition methods we employ to solve the biological problems related to the retina. To develop fully automated nucleus detection methods for counting

photoreceptors, we estimate the cell size based on condition theory (Section 3.1). In order to segment and classify the retinal layers from the retinal images, a support vector machine (SVM) (Section 3.2) and graph partitioning active contours (GPAC) (Section 3.3) are employed. Finally, the use of a Bayesian network as a statistical modeling tool is investigated to build a model for analyzing direct influence among proteins associated with retinal detachment (Section 3.4).

3.1 Condition Theory for Characteristic Neighborhood Detection

Many computer vision tasks are performed by processing the intensity information in the neighborhood of an image point. Examples of these tasks include the detection of reference points and the construction of robust descriptors [58, 30, 33, 64, 68, 75, 72, 6, 57, 39, 78, 49] which can be used for tracking, establishing wide-baseline correspondence, identifying images, and the like. In order to develop algorithms that behave consistently despite changes in the viewing conditions such as translations, rotations, scalings or perspective distortions, it is crucial to automatically identify the characteristic structure of the neighborhood of an image point. In the literature several approaches have been proposed to identify point neighborhoods or the characteristic scale of an image [56, 6, 29, 47].

In order to identify the characteristic dimensions of the cells, we use a mathematical framework based on condition theory that allows us to define the characteristic structure of the neighborhood of a point [86, 39]. In this section, the framework presented in [39] is reviewed and extended to formulate a criterion to

detect the characteristic structure of a point neighborhood (see also [39, 85, 40]). The framework is applied in Chapter 5 to retinal images to estimate the characteristic dimension of cells within the outer nuclear layer (ONL). Experimental results are presented in Section 5.2.2. Before continuing let us introduce a few notation conventions. Throughout the section boldface letters will indicate vectors. The image pixel dimension is indicated with the letter n. When $n = 2$, usual 2-D images are considered, but all the theoretical results still hold in cases where $n > 2$, for example in a z-series, a series of optical sections, of confocal laser scanning microscopy (CLSM), the images with $n > 2$ are referred as generalized images. The image intensity dimension is instead indicated by the letter m: $m = 1$ models a single channel image (such as gray level image), $m = 3$ can model an RGB image and other values of m may be used to model arbitrary multichannel images.

3.1.1 Condition number

What is the sensitivity of an image point neighborhood to noise? The intuitive answer to this question is to measure how much an image neighborhood looks like itself after being perturbed by noise. To this purpose, the noise can be simply represented as an additive random signal that sums to the intensity. However, a quantitative measurement of the effects produced by the noise is a more complex task. Consider a neighborhood $\Omega(\boldsymbol{x})$ about the point $\boldsymbol{x}$ and a point $\boldsymbol{y} \in \Omega(\boldsymbol{x})$. The expression for the image intensity $\boldsymbol{I}$ corrupted by noise $\boldsymbol{\eta}$ at point $\boldsymbol{y}$ is given by:

$$\widetilde{\boldsymbol{I}}(\boldsymbol{y}) \stackrel{\text{def}}{=} \boldsymbol{I}(\boldsymbol{y}) + \boldsymbol{\eta} \tag{3.1}$$

The effect of the noise is modeled by a transformation parameterized by the vector $\boldsymbol{\theta} = \overline{\boldsymbol{\theta}} + \Delta\boldsymbol{\theta}$ that describes the geometric distortion of the intensity pattern in $\Omega(\boldsymbol{x})$. More precisely,

$$\widetilde{\boldsymbol{I}}(\boldsymbol{y}) = \boldsymbol{I}(\boldsymbol{T}_{\overline{\boldsymbol{\theta}}+\Delta\boldsymbol{\theta},\boldsymbol{x}}(\boldsymbol{y})) \tag{3.2}$$

where

$$\begin{aligned} \boldsymbol{T}_{\boldsymbol{\theta},\boldsymbol{x}} : \Omega(\boldsymbol{x}) \subseteq \mathbb{R}^n &\rightarrow \mathbb{R}^n \\ \boldsymbol{y} &\mapsto \boldsymbol{T}_{\boldsymbol{\theta},\boldsymbol{x}}(\boldsymbol{y}) \end{aligned}$$

and $\overline{\boldsymbol{\theta}}$ represents the identity in the parameter space (i.e. $\boldsymbol{T}_{\overline{\boldsymbol{\theta}},\boldsymbol{x}}(\boldsymbol{y}) = \boldsymbol{y}$). It is clear that a neighborhood is more sensitive than another if the same amount of noise produces larger deviations from $\overline{\boldsymbol{\theta}}$ in (3.2).

The sensitivity of a point neighborhood to noise will be measured using the notion of condition number:

Definition 3.1.1 *The condition number associated to the point neighborhood* $\Omega(\boldsymbol{x})$ *with respect to the transformation* $\boldsymbol{T}_{\boldsymbol{\theta},\boldsymbol{x}}$ *is defined as:*

$$K_{\boldsymbol{T}_{\boldsymbol{\theta},\boldsymbol{x}}}(\Omega(\boldsymbol{x})) \stackrel{\text{def}}{=} \lim_{\delta\to 0} \sup_{\|\boldsymbol{\eta}\|\leq\delta} \frac{\|\Delta\boldsymbol{\theta}\|}{\|\boldsymbol{\eta}\|} \tag{3.3}$$

The larger the condition number $K_{\boldsymbol{T}_{\boldsymbol{\theta},\boldsymbol{x}}}$ is, the larger is the magnitude of the variation of the parameter vector $\Delta\boldsymbol{\theta}$ induced by the noise and consequently the larger is the sensitivity of the neighborhood to the noise (or more pictorially, the smaller is the condition number the more similar is the intensity in $\Omega(\boldsymbol{x})$ to itself after being perturbed by noise).

It is now worth noting two things. First, the condition number becomes practically useful only if a closed form for its expression can be provided. Second,

if the statistical distribution of the noise is fixed, the derivatives of the image intensity pattern in $\Omega(\boldsymbol{x})$ play a fundamental role in determining the sensitivity of $\Omega(\boldsymbol{x})$ (or equivalently in the calculation of the condition number). Along this line of thought, the following theorem (whose proof can be found in [86]) provides a computable expression to estimate the condition number, which, as foreseen by Lindeberg [47], turns out to be intimately connected with the image derivatives in $\Omega(\boldsymbol{x})$.

Theorem 3.1.2 *A first order estimate of the condition number* (3.3) *is given by*

$$\hat{K}_{\boldsymbol{T}_{\boldsymbol{\theta},\boldsymbol{x}}}(\Omega(\boldsymbol{x})) = \| A^{\dagger}(\Omega(\boldsymbol{x})) \| \tag{3.4}$$

where † *denotes the pseudo inverse of the matrix:*

$$A(\Omega(\boldsymbol{x})) \stackrel{\text{def}}{=} \begin{bmatrix} A(\boldsymbol{y}_1) \\ \vdots \\ A(\boldsymbol{y}_N) \end{bmatrix} \in \mathbb{R}^{mN \times p} \tag{3.5}$$

which is formed by the N *submatrices:*

$$A(\boldsymbol{y}_i) \stackrel{\text{def}}{=} w(\boldsymbol{y}_i - \boldsymbol{x}) \frac{\partial \boldsymbol{I}}{\partial \boldsymbol{y}}(\boldsymbol{y}_i) \; \frac{\partial \boldsymbol{T}_{\bar{\boldsymbol{\theta}},\boldsymbol{x}}}{\partial \boldsymbol{\theta}}(\boldsymbol{y}_i) \tag{3.6}$$

obtained from a set of N *points that sample the neighborhood* $\Omega(\boldsymbol{x})$*. The scalar function* $w(\boldsymbol{y}_i - \boldsymbol{x})$ *denotes the weight associated to the point* $\boldsymbol{y}_i$*.*

3.1.2 Detecting the characteristic structure

Condition number is the fundamental building block to reveal the characteristic structure of a point neighborhood. Such a principle can be stated as follows:

> The intensity pattern of a generalized image in a neighborhood $\Omega(\boldsymbol{x})$ reflects the characteristic $\boldsymbol{T}$-structure of the image about $\boldsymbol{x}$ if the condition number $K_{\boldsymbol{T}_{\boldsymbol{\theta},\boldsymbol{x}}}(\Omega(\boldsymbol{x}))$ is minimized for local perturbations of the neighborhood itself.

Note that the notion of characteristic neighborhood is intimately related to the geometric transformation $\boldsymbol{T}_{\boldsymbol{\theta},\boldsymbol{x}}$ that is chosen to model the effects of the noise. We can give a formal definition of the $\boldsymbol{T}$-characteristic neighborhood as follows:

Definition 3.1.3 *The $\boldsymbol{T}$-characteristic neighborhood of a generalized image $\boldsymbol{I}$ about a point $\boldsymbol{x}$ is defined as:*

$$\Omega(\boldsymbol{x}) \stackrel{\text{def}}{=} \underset{\delta\Omega}{\operatorname{argmin}}\, \hat{K}_{\boldsymbol{T}_{\boldsymbol{\theta},\boldsymbol{x}}}(\Omega(\boldsymbol{x}) + \delta\Omega)$$

where $\delta\Omega$ represents a local perturbation of the neighborhood.

To translate the previous principle to a computational algorithm we need to specify how the neighborhood is parameterized and the functional form of the geometric transformation that models the effect of the noise. These two choices represent a tradeoff between complexity and accuracy: neighborhoods with many degrees of freedom and transformations described by many parameters can describe precisely the effects of the noise but they are difficult to handle and do not lead to efficient implementations on a computer. For the time being we will focus our attention on circular neighborhoods that can be simply parameterized as:

$$\Omega_r(\boldsymbol{x}) = \{\boldsymbol{y} : \|\boldsymbol{x} - \boldsymbol{y}\| \leq r\}$$

where r represents the radius of the neighborhood. The transformation we consider is intended to model the perturbations produced by the noise in the scaling,

rotation and translation of the intensity pattern of an ordinary image ($n = 2$):

$$\boldsymbol{T}_{\boldsymbol{\theta},\boldsymbol{x}}(\boldsymbol{y}) = \boldsymbol{x} + \begin{bmatrix} \theta_3 & -\theta_4 \\ \theta_4 & \theta_3 \end{bmatrix} (\boldsymbol{y} - \boldsymbol{x}) + \begin{bmatrix} \theta_1 \\ \theta_2 \end{bmatrix} \tag{3.7}$$

This type of transformation is relevant in the context of retinal image processing, where the intensity patterns formed by the cells composing different layers can be arbitrarily oriented and scaled. Observe that the transformation is linear in the parameter vector $\boldsymbol{\theta} \in \mathbb{R}^4$, and that we can write $\theta_3 = s\cos\phi$, $\theta_4 = s\sin\phi$ where s represents the scaling and ϕ the rotation angle. The condition number is invariant with respect to geometric distortions of the neighborhood that are described by the same transformation used to model the effects of the noise. This can be stated formally in the following lemma (whose proof can be found in [86]):

Lemma 3.1.4 *Consider two images ($\boldsymbol{I}$ and $\boldsymbol{I}'$), such that $\boldsymbol{I}'(\boldsymbol{y}') = \boldsymbol{I}(\boldsymbol{y})$ and $\boldsymbol{y}' = sR\boldsymbol{y} + \boldsymbol{t}$, where R is a rotation matrix, s represent scaling and $\boldsymbol{t}$ is the translation. Then:*

$$A'(\boldsymbol{y}') = A(\boldsymbol{y})$$

where A is defined as in (3.6).

As a result of this lemma, the condition number computed for two equivalent neighborhoods remains constant (provided that the density of the sampling points is large enough).

3.2 Support Vector Machine (SVM)

Segmenting the layers from the retinal images is a basic step to analyze the change in the integrity of the layers. The ONL is especially useful for image

segmentation since the layer has a consistent pattern regardless of antibodies used due to the structural similarity of cell bodies among rods and cones. Use of the texture feature is feasible to characterize the spatial pattern within the layers. In order to learn the distribution of texture features corresponding to layers from the noisy data, we need an accurate and robust supervised learning method. A SVM is employed for the ONL classification in Chapter 6 because of its robust performance, since a SVM minimizes structural risk (i.e. generalization or test set error) as opposed to empirical risk (i.e. the training set error) minimization as employed by the artificial neural network (ANN).

A SVM is a relatively new type of learning algorithm originally introduced by Vapnik [79] and successively extended by a number of other researchers. Due to its robust performance with respect to sparse and noisy data, it has been increasingly used in multiple areas from text categorization to microarray expression data evaluation. When used for classification, a SVM separates a given set of binary labeled training data with a hyperplane, called the maximal margin hyperplane, that is most distant from the vectors nearest to the boundary in both of the sets. These vectors are called support vectors.

Let $\mathbf{x}_i, i = 1, 2, \ldots, N$ be the feature vectors of the training set, X and $y_i \in \{-1, +1\}$ be the label of $\mathbf{x}_i$. The SVM finds a hyper-plane $(\mathbf{w}, b)$ such that the margin

$$\gamma = \min_i y_i\{< \mathbf{w}, \mathbf{x}_i > - b\} \tag{3.8}$$

is maximized, where $<,>$ denotes the inner product, the vector $\mathbf{w}$ has the same dimensionality of a feature vector, $||\mathbf{w}||_2$ is held constant, and b is a real number. $(< \mathbf{w}, \mathbf{x}_i > - b)$ is a distance between the point $\mathbf{x}$ and the hyperplane.

When the input vector is correctly classified, $(y_i < \mathbf{w}, \mathbf{x}_i > - b)$ gives a positive value. Given a new data point $\mathbf{x}$ to classify, a label is assigned according to its relationship to the decision boundary, and the corresponding decision boundary function is

$$f(\mathbf{x}) = \text{sign}(< \mathbf{w}, \mathbf{x} > - b). \tag{3.9}$$

Intuitively, this makes the classification correct for testing data that is near, but not identical to the training data. When no linear separation is possible, it can work in combination with kernel methods, which transforms complex inputs in low dimensional space to a high dimensional feature space. The hyperplane found by the SVM in the feature space corresponds to a nonlinear decision boundary in the input space. Let $\phi : \mathbf{x} \in R^l \rightarrow \mathbf{f} \in R^k$ be a mapping from the input feature space into a k-dimensional space, where the classes can satisfactorily be separated by a hyperplane. Similar to (3.9), a new data point $\mathbf{x}$ is classified by

$$f(\mathbf{x}) = \text{sign}(< \mathbf{w}, \phi(\mathbf{x}) > -b). \tag{3.10}$$

$K_{ij} =< \phi(\mathbf{x}_i), \phi(\mathbf{x}_j) >$ is called the *kernel matrix* and $K_{ij} = K(\mathbf{x}_i, \mathbf{x}_j)$ provides non-linear boundaries. Typical examples of kernel used in classification applications are

Polynomials:

$$K(\mathbf{x}_i, \mathbf{x}_j) = (< \mathbf{x}_i, \mathbf{x}_j > +1)^d, \tag{3.11}$$

and

Radial Basis Functions:

$$K(\mathbf{x}_i, \mathbf{x}_j) = \exp\left(- \frac{||\mathbf{x}_i - \mathbf{x}_j||^2}{\sigma^2} \right). \tag{3.12}$$

Although, we can not visualize the feature space and what happens inside the kernel, we sill have the geometric interpretation of the maximal margin hyperplane, so the SVM is more transparent than for example ANN.

3.3 Graph Partitioning Active Contours (GPAC)

There is no previous work on segmenting retinal layers from images. Image data in an individual layer is not statistically homogeneous information. Further difficulties in retinal images include visual variation from staining. For example, the same layer can show different structures depending on probed antibodies. To cope with the heterogeneity of retinal images, it is necessary to combine high-level information as well as low-level features extracted from images. GPAC is used as our segmentation method in Chapter 6 because of the versatility of GPAC; the information about pixels can be easily embedded in the similarity metric and it provides robust results in spite of topology changes.

In this section, we briefly introduce the mathematical framework of GPAC. In [76] Sumengen and Manjunath proposed a new approach to variational segmentation, which combines region-based active contour methods [59, 13] and graph partitioning methods [74]. They introduced a new class of variational cost functions based on the similarity or dissimilarity between pixels for background foreground segmentation. Using the notation $w(p_1, p_2)$ to represent the pairwise dissimilarity between point p_1 and point p_2 (where p_i is a 2-D point in the image domain), we can write this variational cost function as:

$$E(C) = -\iint_{p_1 \in R_o(C)} \iint_{p_2 \in R_i(C)} w(p_1, p_2) dp_1 dp_2 \tag{3.13}$$

where $R_i(C)$ and $R_o(C)$ are respectively the regions inside and outside the curve C. The minimization of $E(C)$ with respect to the curve C leads to a partitioning of the image, which maximizes the dissimilarity between regions $R_i(C)$ and $R_o(C)$. Steepest descent with respect to the curve C yields to the following curve evolution equation:

$$\frac{\partial C}{\partial t} = \Big(\iint_{p \in R_o(C(t))} w(c, p) dp - \iint_{p \in R_i(C(t))} w(c, p) dp \Big) \overrightarrow{N} \tag{3.14}$$

where c is a point on the curve C. Thus, every pixel on the curve C is compared with the interior and the exterior of the curve in terms of their similarities. The curve is then expanded or shrunk accordingly in the normal direction. At steady state the region inside of C and the region outside of it are the segmented background and foreground of the image.

GPAC combines region-based active contour methods and graph partitioning methods, exploiting the advantages of both approaches. The flexibility of graph partitioning methods, in which any information about pixels (i.e. intensity, color, texture, or neighborhoods statistics) can be easily embedded in the similarity metric, is therefore combined with the robustness of active contours and level set methods.

3.3.1 Background/Foreground Segmentation

The main idea of using the curve evolution framework is to solve the minimum cut problem. The minimum cuts criterion states that the best partition of a

weighted graph is the one which minimizes the following cost function:

$$cut(A,B) = \iint_{p_1 \in A} \iint_{p_2 \in B} w(p_1,p_2) dp_1 dp_2. \tag{3.15}$$

The variational cost functions shown in (3.13) can be rewritten based on dissimilarity within two regions (backround/foreground) [8].

$$\begin{aligned} E \;=\; & \iint_{p_1 \in A} \iint_{p_2 \in A} w(p_1,p_2) dp_1 dp_2 + \\ & \iint_{p_1 \in B} \iint_{p_2 \in B} w(p_1,p_2) dp_1 dp_2, \end{aligned} \tag{3.16}$$

where $w(p_1,p_2)$ is a dissimilarity metric (e.g distance in a particular feature space), $p_1 = (x_1,y_1)$ and $p_2 = (x_2,y_2)$ are 2-D points in the image and A, B form a partition such that $A \cup B = \Omega$, where Ω represents the whole image domain. The goal is to minimize this cost function, which we name *total dissimilarity within regions*, in order to partition the image into foreground and background.

Defining the region using implicit surfaces and using the gradient descent method for the minimization, we use this equation to evolve the level set functions:

$$\begin{aligned} \frac{\partial \phi(p_2)}{\partial t} \;=\; & \delta(\phi(p_2)) \Big[\iint_{\Omega} w(p_1,p_2) \Big(1 - H(\phi(p_1)) \Big) dp_1 \\ & - \iint_{\Omega} w(p_1,p_2) H(\phi(p_1)) dp_1 \Big]. \end{aligned} \tag{3.17}$$

This is equivalent to the curve evolution equation obtained in (3.14) with a more involved mathematical derivation. That is, every point c on the curve C (because of the presence of $\delta(\phi(p_2))$) is compared to the points inside and outside the curve. If c is more similar (less dissimilar) to the interior, the curve expands including c in its internal region, otherwise it shrinks. See [8] for more details and proofs.

For the retinal images, the foreground can be any layer (e.g. the ONL) that we aim to separate from the rest of layers. We calculate three dissimilarities between

pixels, color, texture, and nuclei density. For example, the dissimilarities using color feature are evaluated as follows:

$$w_{col}(p_1, p_2) = \sqrt{\sum_{i=1}^{3} \Big(c_i(p_1) - c_i(p_2) \Big)^2} \tag{3.18}$$

where c_i represent each one of the color channels. By embedding high-level information, the nuclei density calculated using candidate nuclei positions (proposed in Chapter 4), into the dissimilarity metric, the ONL can be segmented precisely in spite of the heterogeneity of retinal images.The segmentation result is immediately useful for automating further analysis such as counting photoreceptor nuclei within the ONL and characterizing the structural distortions of the layers described in Section 5.3.

3.4 Bayesian Networks

Many applications in computational biology have taken advantage of Bayesian networks, or, more generally, probabilistic graphical models. These include protein modeling, gene expression analysis [31], and pathway modeling [70], and biological data integration. These models can predict dependencies between differentially expressed genes or proteins, providing further insights of the interactions among molecules or cells.

Our primary goal is to model the retinal detachment process to understand the protein-protein interactions within the retinal cells as well as interactions between cells. The Bayesian network framework is ideally suited to study this problem. The Bayesian network is used in Chapter 7 to model the retinal detachment process. In this section, we review the basic concept of Bayesian network and

how they are used for inference.

3.4.1 Bayesian network basis

A Bayesian network is a compact graphical representation of the joint probability distribution over a set of random variables [34, 42]. The variables can represent the expression level of a gene, or a protein. Typically, continuous values are discretized into two or more categories(e.g. on/off or high/medium/low) by thresholding the values. A Bayesian network has two components:

- **a directed acyclic graph** $G = (V, E)$ with a node set V corresponding random variables $x_1, \ldots, x_n$ and edge set E of the nodes. An edge represents the statistical dependence between the variables and a node is conditionally independent of all other nodes given its parents in the network.

- **a parameter set** θ for conditional probability distributions of each node in the graph G. These probability distributions are local, and are of the form $p(x_i|\mathbf{pa}(x_i))$, where $\mathbf{pa}(x_i)$ is a parents nodes of x_i.

The two components (G, θ) specify a unique distribution of the random variables $x_1, \ldots, x_n$. The joint probability distribution is compactly expressed as

$$p(x_1, \ldots, x_n) = \prod_{i=1}^{n} p(x_i|\mathbf{pa}(x_i)). \tag{3.19}$$

The ability to express the joint probability by exploiting conditional independencies provide a concise representation in terms of a product of simple component distributions, thus reducing the number of parameters to be estimated.

3.4.2 Learning a Bayesian network

The structure and parameters of a Bayesian network can be statistically inferred from an adequate amount of observed values of variables, $x_1, \ldots, x_n$. Let data set $D = \{(x_1(1), \ldots, x_n(1)), \ldots, (x_1(M), \ldots, x_n(M))\}$ be M measurements of n variables. For example, these measurement can be a set of n protein expression levels measured within the ONL (Section 7.2.1). The problem of learning a Bayesian network from data has been studied extensively [34, 42, 60]. Learning a network model on a set of variables $x_1, \ldots, x_n$ requires inferring the graph of dependencies between them, as well as parameters θ consisting of local conditional probabilities, $p(x_i|\mathbf{pa}(x_i))$.

If the graph structure G is known, the parameters θ can be estimated from the data D by maximum likelihood estimation or Bayesian estimation. The likelihood of the data D given parameters θ for a known structure G is

$$L(\theta; D) = P(D|\theta) = \prod_{i=1}^{M} P(x_1(i), \ldots, x_n(i)|\theta). \tag{3.20}$$

For maximum likelihood estimation, parameters θ^*_{ML} is estimated as

$$\theta^*_{ML} = \arg\max_{\theta} L(\theta; D). \tag{3.21}$$

When the number of measurements M is small, maximum likelihood estimation tends to overfit the model parameters to the data. Bayesian methods reduce overfitting by using available knowledge about the parameters in the form of a prior distribution $P(\theta)$. By Bayes rule,

$$P(\theta|D) = \frac{P(D|\theta)P(\theta)}{P(D)} \tag{3.22}$$

and the estimated parameter θ^*_{MAP} is

$$\theta^*_{MAP} = \arg\max_{\theta} P(D|\theta)P(\theta). \tag{3.23}$$

Learning structure G from data is a very challenging problem [34, 42]. The most common approach to discover the structure of a Bayesian network from the data is to define a space of graph models to consider, and set up a scoring function that evaluates how well a model predicts the data. The scoring function is the logarithm of the posterior probability of the network structure given data

$$Score(G; D) = \log P(G|D) = \log P(D|G) + \log P(D), \tag{3.24}$$

where $P(D|G) = \int_\theta P(D|G, \theta)P(\theta|G)d\theta$. An alternative scoring function is an asymptotic approximation to the full posterior probability called Bayesian information criterion (BIC), which is defined as follows:

$$\log P(G|D) \approx \log P(D|G, \hat{\theta}) - \frac{\log N}{2}|G|, \tag{3.25}$$

where D is the data, N is the number of samples, $|G|$ is the dimension of the model, and $\hat{\theta}$ is the maximum likelihood estimate of the parameters.

To model the retinal detachment process, a Bayesian network is constructed with quantitative features derived from retinal images under different experimental conditions. The resulting causal network structure models interesting associations between protein expressions (e.g. rod opsin and glial fibrillary acid protein (GFAP)) in a quantitative manner that is reproducible (Chapter 7).

3.5 Summary

We introduced a number of methods that we use to attack biological problems. In the following chapters, we present how these methods are applied for segmentation, classification, and statistical modeling. We use a mathematical framework based on condition theory to estimate the size of photoreceptor nuclei which leads to an automated nucleus detection (Chapter 5). In order to segment the ONL from the retinal images, SVM and GPAC are used (Chapter 6). Finally, a Bayesian network is used as a statistical modeling method to discover underlying interaction between proteins in response to retinal detachment (Chapter 7).

Chapter 4

Detecting Cell Nuclei

"The cell is the center of the universe."

Jeffrey Price

Cell addition and loss are important biological events in development and pathology. As a result, counts of cells and nuclei from histological sections provide quantitative information central to studying changes in cells, tissues, and organs. While progress in understanding changes in such parameters as cell structure or protein expression has been rapid during the past few decades, methods for determining cell number have remained limited.

In this chapter, we propose a method for detecting nuclei, and therefore cell bodies, from a 2-D digital micrograph. The proposed approach provides an accurate, simple, and reliable method to count cells, nuclei, or other objects in sectioned materials. The proposed nucleus detector has a number of advantages over manual analysis and other currently available or proposed automatic/semi-automatic methods including objectivity, simplicity, and applicability.

4.1 Introduction

4.1.1 Motivation

Cell addition and loss are important biological events in development and pathology. As a result, counts of cells and nuclei from histological sections provide quantitative information central to studying changes in cells, tissues, and organs. For example, the neuron number is a fundamental determinant of brain function [83] and the number of photoreceptors is a common measurement of visual function of retina [66, 55, 43, 71, 27]. While progress in understanding changes in such parameters as cell structure or protein expression has been rapid during the past few decades, methods for determining cell number have remained limited. Determining the numerical density of cells in sectioned materials is difficult. Indeed, even the most rigorous studies rarely claim precision greater than $\pm 10\%$ [83]. Consequently, only marked changes or effects can be analyzed with confidence. For example, the measurements have been done on only a few sparse locations throughout the retina [77, 4]. The total cell number of a whole retina is often extrapolated based on the measured data from a few locations. Such an extrapolation method can easily mislead us to a biased conclusion depending on the sampling location (See section 5.3.2). It has been determined that the larger the tissue and steeper the gradients in cell density, the greater the margin of error. Several solutions to this problem have been proposed, but they require significant resources in order to complete a morphometric analysis. For example, as we mentioned in Section 2.4 in Chapter 2, the outer nuclear layer (ONL) in each image taken by a confocal microscope with a 40x magnification oil immersion

lens, represents $1/2,000,000,000^{\text{th}}$ (a two billionth) of the whole retina. Moreover, most of these methods still require manual counting, which is tedious and time consuming, regardless of whether a 2-D or a 3-D methodology is employed. Problems that demand greater accuracy and reliability cannot be resolved with current manual methods.

4.1.2 Related work

Image analysis methods have been developed for nucleus detection or segmentation. In the past, algorithms developed for automatic micrograph analysis have been very task specific and are not easily extendable to analysis of different types of images such as those generated by immunofluorescence. The watershed transform has been widely used in segmenting nuclei from images [50, 46]. The intuitive description of a watershed transform is quite simple: if we consider the image as a topographic relief, where the height of each point is directly related to its gray level, and consider rain gradually falling on the terrain, then the watersheds are the lines that separate the lakes (actually called catchment basins). Generally, the watershed transform is computed on the gradient of the original image, so that the catchment basin boundaries are located at high gradient points. While the watershed transform separates the boundary between clustered cells, it often results in over-segmentation, especially when the image is noisy and the intensity within a cell is varied. Other common methods are based on morphological operators and gray level thresholding [63, 18]. These methods work well for segmenting cells in images with sparse density, however, these methods do not work for segmenting clustered cells. Additionally, there are some commercial softwares that provide

object-counting and feature detection [1, 2]. However, these tools often fail to provide reliable results and require intensive user interaction in order to obtain user-given initialization or parameter settings for accurate results. Furthermore, these tools are not designed to analyze immunofluorescent images, which present unique challenges, especially in tissues like the retina:

- cells are densely packed (600 cells in 512 × 100 pixels),
- uneven staining and local variation in the surface of a tissue can cause intensity variations within cell layers (Figure 4.1 (a)),
- non-uniform DNA distribution inside the nucleus can cause intensity variations within individual cells (Figure 4.1 (b)).

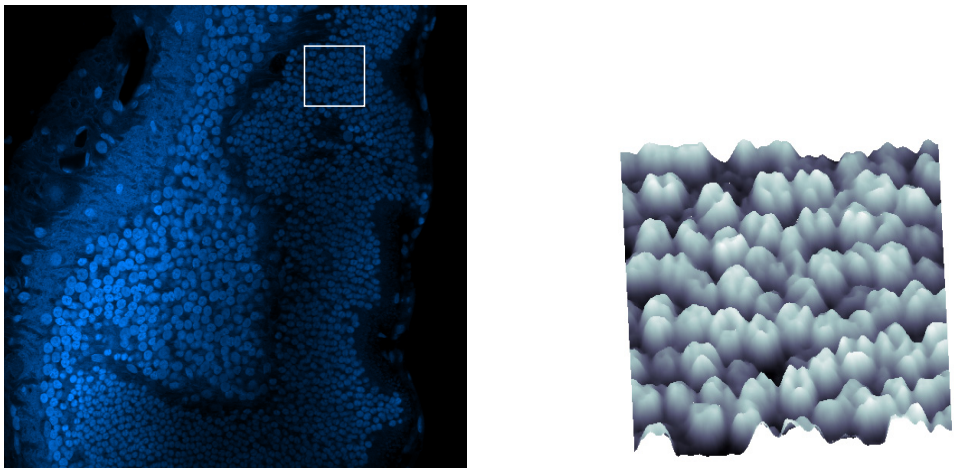

(a) (b)

Figure 4.1: Challenges in detecting nuclei from retinal images. (a) An example image of a 7-day detached cat retina stained with the nuclear dye, TO-PRO. Intensity variations caused by uneven staining and local variation in surface due to retinal folding. (b) 3-D surface plot of a rectangular region in (a). Each nucleus is represented by multiple peaks caused by variation of DNA distribution within a cell.

There is a need for robust methods for automatically counting nuclei with consistently high accuracy and reliability in large sets of digital micrographs. We present here a methodology for detecting nuclei, and therefore cell bodies, from 2-D digital micrographs. The method is motivated by automatically detecting photoreceptor nuclei within the ONL for characterizing the cell death in response to retinal detachment. The counting of photoreceptor nuclei is automated, reducing tedious, time consuming, and routine manual counting. The performance of this nucleus detector/counter is evaluated by comparing the results with manual counts. The nucleus detector correctly counts nuclei within the ONL with an average error of 3.67% (ranging from 0 to 6.07%), and nuclei within the inner nuclear layer (INL) with an average error of 8.55% (ranging from 0 to 13.76%). Both manual counting and nucleus detector result in the same conclusion; *the number of cells within the INL does not change in response to 3-day retinal detachment.* This is the first time that cell death in the INL have been counted, verifying an earlier qualitative prediction of cell survival in the inner retina in response to retinal detachment [27]. The proposed method is actively used in Steve Fisher's lab for providing quantitative information to prove/reject various hypotheses of the response of the retina to detachment and reattachment [37, 26, 28].

This chapter is organized as follows. We first introduce a nucleus detector (Section 4.2). In order to have a scientific basis for selecting optimal parameters of the method, we mainly focus on retinal images, in particular the ONL, since it has been previously shown that the number of photoreceptors decrease after detachment [4, 43]. Specifically, we detect fluorescent labeled photoreceptor nuclei from confocal images of control and degenerating feline retina as a result of retinal

detachment (Section 4.2.3). To show that the proposed method can be applied to many types cells and imaging without significant effort of parameter tuning, we also tested it with images of various types of cells acquired using transmitted light and epi-fluorescent microscopy (Section 4.3).

4.2 Nucleus Detection

The basis of the study is a set of immunofluorescent retinal images which have been collected by confocal imaging for understanding the mechanisms underlying the loss and recovery of vision following retinal detachment and reattachment. The stacks of serial optical sections, often termed a z-series, are collected from a 100 μm thick retinal tissue section and only a single optical focal plane image from each z-series is used to count nuclei within the specific focal plane (See Figure 2.14). Counting the superimposed nuclei in multiple depth planes can be avoided by using a single plane image instead of a multiple focal plane superimposed image (composite or projection view).

Photoreceptor cells have received the greatest attention in these studies since photoreceptor outer segment degeneration and cell death are considered a major effect of detachment. Previously it has been shown that the number of photoreceptors decrease after detachment [4, 43] (Figure 4.2). Such degeneration of photoreceptors has been measured in various ways in different studies [45, 43, 55]: 1) the number of rows of nuclei in the ONL, 2) the area of the ONL, 3) the thickness of the ONL, and 4) the number of nuclei in the ONL. The values of these measurements are usually represented as change over time which is then used as an index of photoreceptor degeneration. It has been verified that the ONL appears

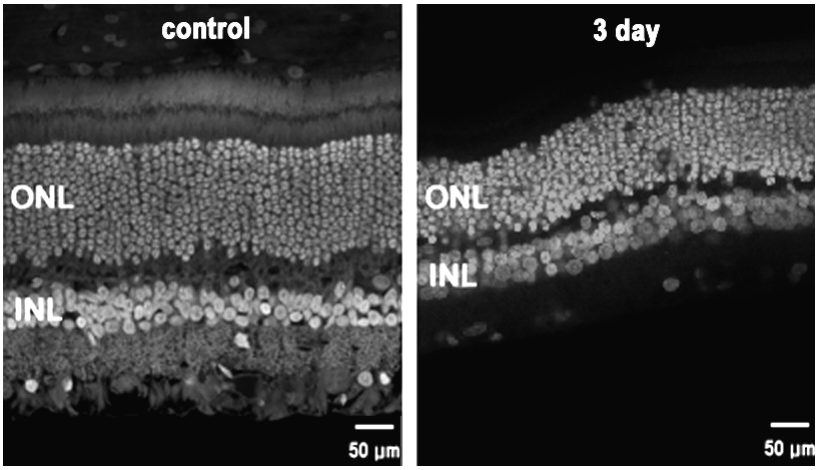

Figure 4.2: Confocal images of normal and detached retinas stained with the nuclear dye, TO-PRO. For visualization purposes, the images are converted into gray scale images. After a 3 day detachment the ONL appears to be thinner than the control attached tissue.

to be much more loosely packed with nuclei compared to normal as a result of loss of cells following detachment [43, 27]. ONL thickness or area may not always give an accurate measure of cell loss, since thickness or area are varied depending on the location of tissue or the distortion of tissue (e.g. retinal folding). We therefore use the number of nuclei in the ONL to compare with results obtained using the newly developed automated nucleus detector.

4.2.1 Nucleus as a blob

Filtering is a very general technique of transforming image gray levels in some way so as to enhance certain features [32, 69]. Template matching is a simple filtering method for detecting a particular feature in an image. If the appearance of a particular feature in the image is known accurately, one can try to detect it using template matching. The template used in this matching is a subimage that

looks just like the image of the object. A similarity measure is computed which reflects how well the image data match the template for each possible location.

Figure 4.2 shows a confocal image of a normal feline retina illustrating the nuclear layers of the retina. In the image, nuclei can be approximated as simple, nearly circular shaped *blobs*. Therefore, our study focuses on developing an efficient detection solution for the nuclei, a class of blob-like structures, by modeling them as roughly convex local intensity distributions whose iso-level contour is approximately circular with some irregularities. First, a *blob* model is needed to generate the template for the nucleus. A single plane image will always show a slice of the individual nuclei. The boundary of each nucleus shows up as strong intensity discontinuities in an image (Figure 4.3 (a) and (b)).

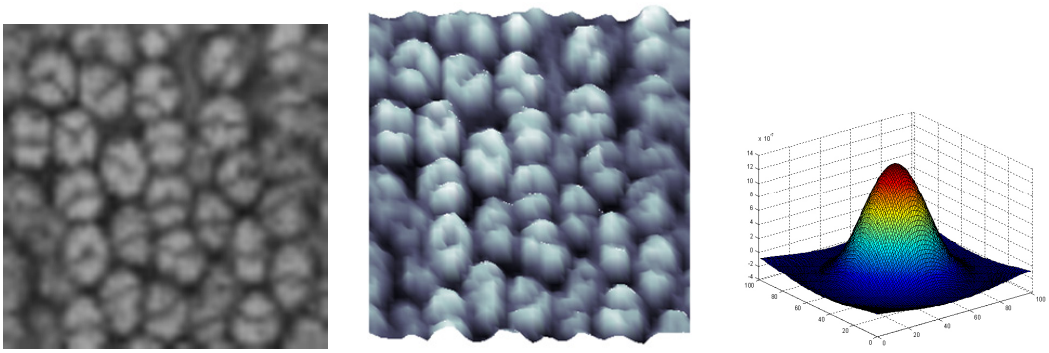

(a) (b) (c)

Figure 4.3: Cells in the ONL. (a) Example image of the ONL within a feline retina stained by TO-PRO. TO-PRO stains double stranded nucleic acid in nuclei, which appears much brighter in certain parts of the cell. Such intensity variation is associated with the DNA distribution within these cells. (b) 3-D surface plot of (a): the height of each point on the 3-D surface corresponds to the intensity of each pixel in the image. Each nucleus is represented by multiple peaks caused by variations in the DNA distribution within a cell, however, it can be modeled as a uni-modal intensity distribution shown in (c). The model is used as a template to detect nuclei in an image.

While the intensity of a nucleus often has a uniform distribution, the intensity distribution of some nuclei has multiple peaks (Figure 4.3 (a) and (b)). These multiple peaks within a nucleus are caused by non-uniform DNA distribution inside a nucleus. Since nuclear staining such as TO-PRO stains double stranded nucleic acid in nuclei, the staining appears much brighter in certain parts of the cell. However, the intensity distribution can have a single peak inside each nucleus after the appropriate amount of Gaussian blurring. After Gaussian blurring, the profile of a nucleus becomes a ridge with smooth changes in gray level. Therefore, a *blob* can be modeled as a 3-D surface generated by rotating a ridge profile around its central axis (Figure 4.3 (c)). If the nuclei is modeled as this blob with some additive Gaussian noise, an optimum linear blob detector can be designed by rotating the second derivative of a Gaussian around its central axis. In the image processing literature, this filter is well approximated by the Laplacian of Gaussian (LoG) [12]. The general idea of the LoG is to detect edges and lines in images by determining the peak point of the ridge as accurately as possible given the ridge profile is corrupted by certain amount of Gaussian noise. LoG has been utilized in the image processing community for detecting edges [69, 32]. In this work, the inverted Laplacian of Gaussian (LoG) is utilized as the blob detector. The nuclei are modeled as circular objects although some of these objects resemble ellipsoids. The objective in using a circular model, a very general shape model, is to achieve a rotation invariance in the detection. Otherwise it is possible to overfit the blob model to the training images.

4.2.2 Nucleus detector design

The blob centers are detected with the following two steps:

1. **Blob detector design** The LoG filter is designed such that the diameter of the filter is proportional to the average diameter of nuclei in the image. For example, the average size of photoreceptor nuclei in the feline retina is 4-6 μm so the diameter of the filter can be set as 5 μm. The filter size in μm can be easily converted to pixel size using the metadata embedded in a given image. The given retinal image is then filtered by the LoG. This operation results in a smooth continuous image of which the local maxima correspond to blob centers.

2. **Search for local maxima** Local maxima are searched from the filtered output. The minimum distance between blob centers is used as the search radius for the local maxima, and this parameter is defined to be proportional to the filter size.

In summary, the nucleus detector requires two inputs: 1) the cell size in μm or equivalent in pixels, and 2) the minimum distance between cells. The nucleus size to detect in biological tissues is usually well known. A schematic diagram for a nucleus detector is shown in Figure 4.4.

4.2.3 Evaluation of the nucleus detector

The goal of the nucleus detector is to generate counts of nuclei within the tissue layer of interest that are close to that obtained by manual counting. The manual count value, which is known as ground truth, is compared with the results

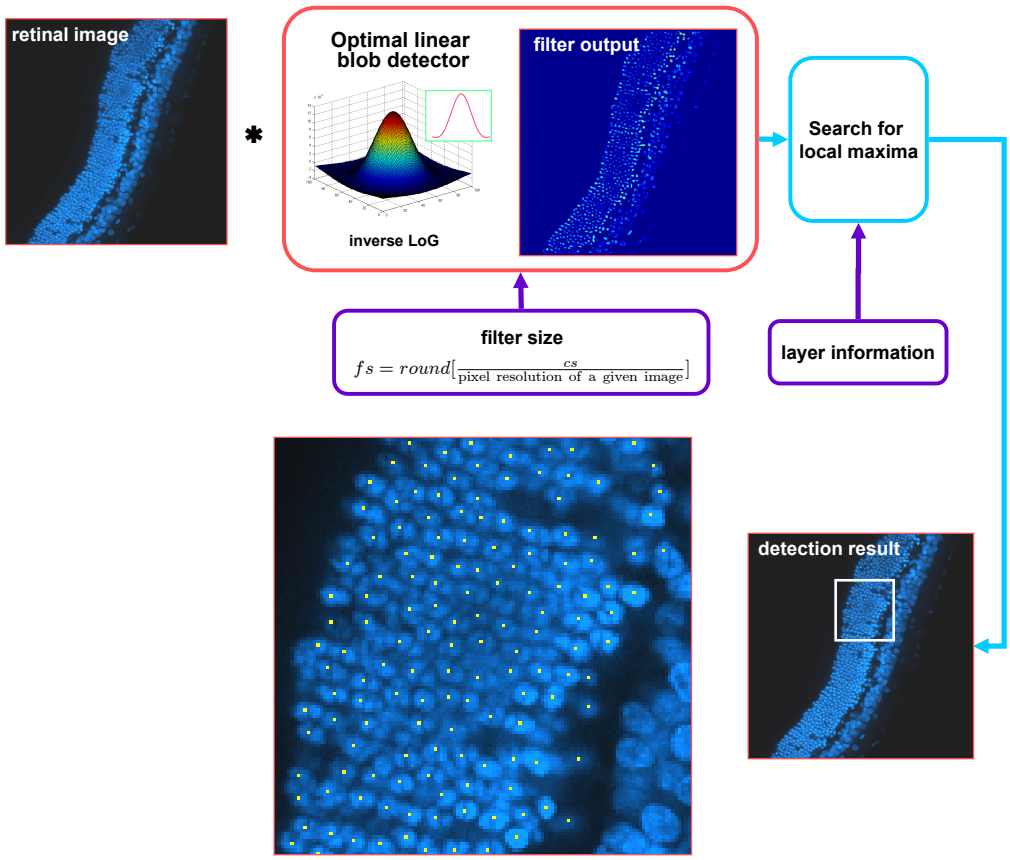

Figure 4.4: Schematic diagram of a nucleus detector: the blob centers are detected by filtering with the blob detector followed by searching for local maxima. Higher magnification of the rectangular region is shown to the left of the result image.

of the automatic nucleus detector using various combinations of parameters. To estimate optimal parameters of the nucleus detector, its performance is evaluated using error criterion as

$$E \triangleq \frac{1}{N} \times \frac{|ND - GT|}{GT}, \tag{4.1}$$

where N is the number of images in the training set, ND and GT is the number of nuclei detected by the nucleus detector and by manual counting, respectively.

The ground truth for 41 retinal images are obtained. These 41 images of normal and 3-day detached feline retinas (21 control images and 20 3-day detached retinal images) are generated with an Olympus FluoView laser scanning confocal microscope from tissue sections stained with TO-PRO. A single optical section image 0.5 μm thick from each z-series is used for counting to avoid counting superimposed nuclei in multiple planes. For each image, a mask to define the boundary of the ONL and the INL is created manually (Figure 4.5).

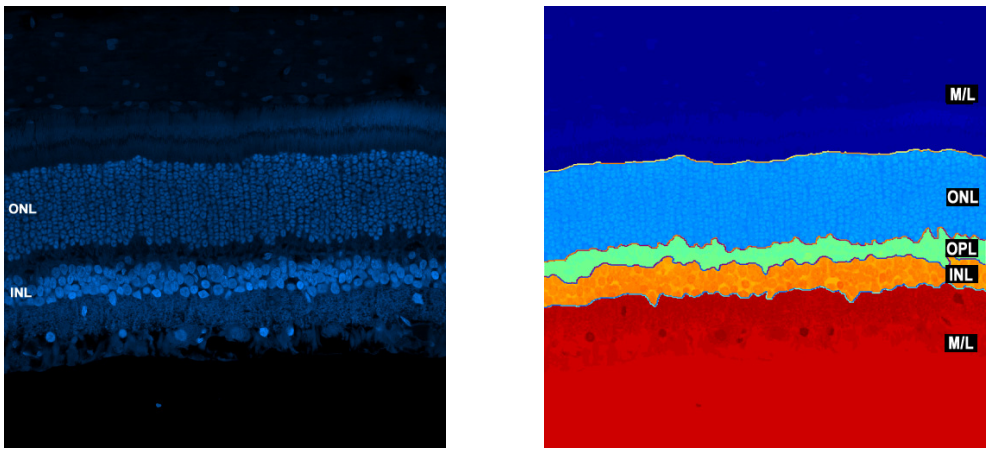

(a) (b)

Figure 4.5: Example image of a layer map, a schematic representation of the retinal layers, created from a retinal image. (a) Confocal image of a normal cat retina stained by TO-PRO. (b) Layer map of (a). Boundaries of layers are outlined manually.

The same data set is used for manual counting to create ground truth. Each image is manually counted three times independently to measure intra-observer variation. Due to the small data set, the leave-one-out cross-validation method is employed to evaluate the detector's performance. That is, the nucleus detector is trained 41 times, each time leaving out one image from the training data set, and using only the omitted image to compute the error. The resulting estimates of generalized error are used for choosing the optimal parameters for the nucleus detector.

The performance of the proposed nucleus detector depends on two factors. First, a filter size and standard deviation σ determined by how well the the filter approximates the shape of a nucleus. Second, the minimum distance between blob center is dependent on how well the local maxima are determined. Since we search the filter output for local maxima, σ does not affect the performance of the nucleus detector. Thus, we vary two parameters: cell size (cs) in μm and the proportion (p) of the minimum distance between blob centers and filter size (fs), where fs is defined as $round[\frac{cs}{pixel\ resolution\ of\ a\ given\ image}]$ ($round[x]$ is the integer closest to x). The parameter cs is varied by five different values from 4 to 8. The range of the values is determined by the cell size within the ONL. The parameter p varies from 0.1 to 1 in steps of 0.1. Thus, we have a total 5×10 combinations, and 41 runs are conducted for each combination. We find the nucleus detector achieved a maximum performance (i.e. a minimum error) at $cs = 5\ \mu m$, $p = 0.5$. In practice, additional training is not needed and users simply can apply the above parameters to the retinal images given that image resolution is known. The filter size can be computed automatically using image resolution information extracted

from the image. For example, when the image resolution is 0.324 μm per pixel, the filter size is computed as $round[\frac{5\ \mu m}{0.324\ \mu m/pixel}]$, that is, 15 pixels. In other words, the filter size is automatically tuned to the cell size given a retinal image with the image resolution. Then we apply the optimized nucleus detector to the data set.

The nucleus detector approximates the number determined by manual counting. The average absolute error of the nucleus detector is 3.67% ranging from 0 to 6.07% for the ONL. Considering intra-observer variation is 1.8%, the results from our nucleus detector is promising. The nucleus detector does not systematically overestimate or underestimate the number of nuclei compared to the manual counts. The summary of test result is shown in Figure 4.6. The first 23 images are collected as high pixel resolution, 0.324 μm per pixel and the rest of images are collected as 0.621 μm per pixel. The nucleus detector provide consistent results regardless of the pixel resolution of the image.

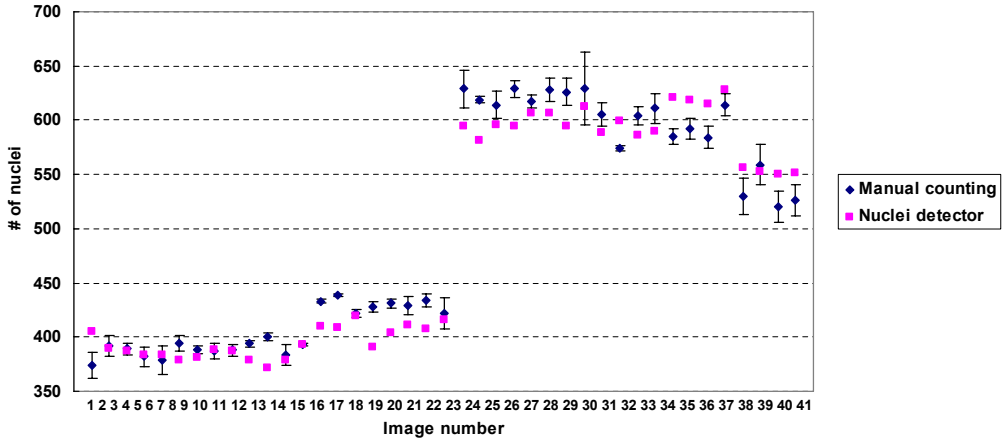

Figure 4.6: A summary of test results of 41 images. Blue dots denote manual counting and the error bar of each blue dot indicates intra-observer variation. Pink dots represent the result of the automated nucleus detector. The first 23 images from the left are collected as a high resolution, 0.324 μm per pixel and the rest of images are collected as 0.621 μm per pixel. The nucleus detector provides consistent results regardless of the pixel resolution of the image.

Even though we do not have ground truth of (x,y) coordinates of detected nuclei, the locations of detected nuclei overlayed on the image seem visually acceptable (Figure 4.7 (a) and (b)). Note that the contrast of the image shown in Figure 4.7 (b) is not high enough to assure visibility so that variation among the three manual counting results of a given image become relatively high at 3.37%.

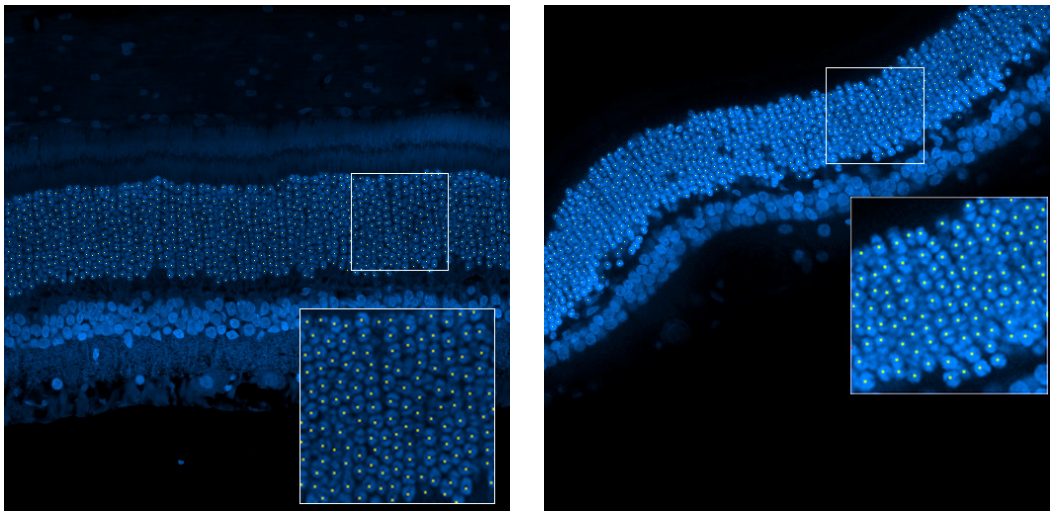

(a) (b)

Figure 4.7: Application of the nucleus detector to retinal images. (a) Confocal image of a normal cat retina stained by TO-PRO. Detected cell centers are marked with yellow points. 688 cells are detected with 0.5% error compared with manual counts (690 cells). (b) Applying the nucleus detector to diagonally oriented confocal image of a 3-day detached cat retina stained by TO-PRO. The image was acquired with poor contrast. Detected cell centers are marked with yellow points. 606 cells are detected with 3.5% error compared with manual counts (628 cells).

We also apply the nucleus detector to the INL of the same 41 retinal images. The number of cells within the INL from each image is manually counted three times. The average variation for the INL is higher than that of the ONL as 3.1% ranging from 0.78 to 8.41%. Since the INL consists of three different types of cells

that are packed closely together, the boundaries of optically sliced cell bodies within the INL are poorly defined. Those ill defined boundaries result in large variation in manual counting. The average absolute error of the nucleus detector is relatively high (8.52%) ranging from 0 to 13.76% for the INL. Large variation in manual counting for the INL results in a large error for the nucleus detector.

4.3 Experimental Results

In general, a good nucleus detector should satisfy the following three criteria: 1) accurate so that it can approximate manual counting; 2) simple and computationally efficient, providing reliable results; and 3) applicable to a wide variety of image types with minimal user interaction including parameter settings or preprocessing of the given image. To show that our nucleus detector satisfies these three criteria, we apply it to various sets of retinal images (e.g. confocal images of cat retina and transmitted light microscope images of mouse retina) as well as other images commonly generated (e.g., fluorescent cell images).

4.3.1 Applying cell counting to retinal detachment

Automated nuclear counts are used to verify the finding that the number of photoreceptors decrease in response to a retinal detachment. In the feline model, retinal detachment leads to the death of some photoreceptor cells [43, 16, 23]. Figure 4.8 shows the average number of photoreceptor nuclei per mm^2 of retina in control eyes and those with 3-day detached retinas using the manual counting method. The control retina have, on average, 37503 nuclei/mm^2. After 3 days of

detachment, this number is reduced to an average of 33590 nuclei/mm^2 (Student's t-test[1] p$\leq$0.0001). The average number of photoreceptor nuclei is not exactly the same as the manual count, however, the number is not statistically different from the manual count (p=0.01 $<$ 0.05). The nucleus detector captures relative differences in cell density between normal and 3-day detached cases and reaches the same conclusion as manual counting (Figure 4.8). In addition, the variances of manual counts are larger than those of the nuclei detection results indicating that nucleus detector performs better than manual counting by providing statistically similar result to manual counting yet smaller variation of the result.

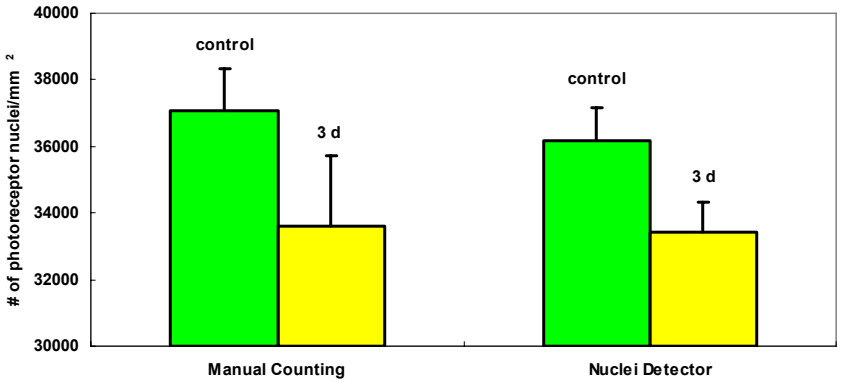

Figure 4.8: A comparison of manual and nucleus detector counts of the average number of photoreceptor nuclei per mm^2 of retina in normal and 3-day detached retina. Manual counts. The control retina had, on average, 37503 nuclei/mm^2. After 3 days of detachment, the cell count is reduced to an average 33590 nuclei/mm^2 (p$\leq$0.0001). Nucleus detector counts. The control retina had, on average, 36164 nuclei/mm^2. After 3 days of detachment, the cell count is reduced to an average 33417 nuclei/mm^2 (p$\leq$0.0000007). Both manual counting and the nucleus detector result in the same conclusion; *the number of photoreceptor is reduced in response to 3-day retinal detachment.*

[1]Student's t-test is a statistical hypothesis test for two groups in which the test statistic has a Student's t distribution if the null hypothesis is true [82]. The t-test assesses whether the means of two groups are *statistically* different from each other. The returned p value stands for the proportion of the area under the curve between t and ∞, if one wants to measure the confidence C, $C = 1 - 2p$. When p is less than 0.05, two groups are considered significantly different.

For the INL, manual counts in 3-day detached retinas would not be considered statistically different from those in normal retinas (p=0.05309>0.05) (Figure 4.9). Thus, both manual counting and the nucleus detector result in the same conclusion; *the number of cells within the INL does not change in response to 3-day retinal detachment*. This is the first time that the number of cells in the INL have been counted verifying an earlier qualitative prediction of cell survival in the inner retina in response to retinal detachment [27].

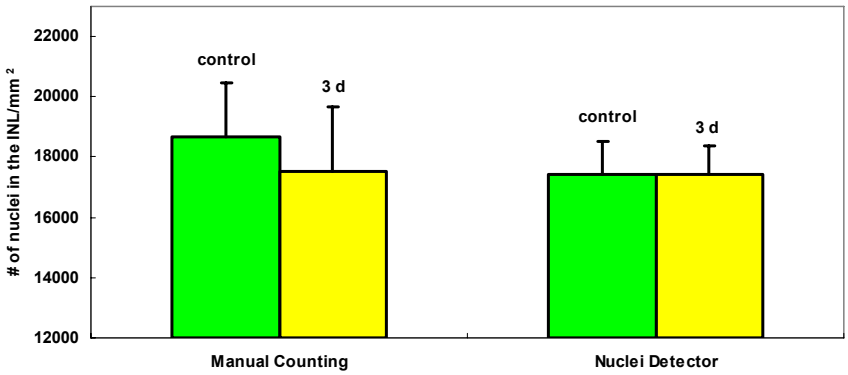

Figure 4.9: The average number of nuclei within the INL per mm^2 of retina in normal and 3-day detached retina. Manual counts. The control retina had, on average, 18659 nuclei/mm^2. After 3 days of detachment, the cell count is reduced to an average 17516 nuclei/mm^2 (p=0.05309>0.05). Nucleus detector counts. The control retina had, on average, 17501 nuclei/mm^2. After 3 days of detachment, the cell count is reduced to an average 17435 nuclei/mm^2 (p=0.9755>0.05). Both manual counting and the nucleus detector reach the the same conclusion; *the number of cells within the INL does not change in response to 3-day retinal detachment*.

4.3.2 Application to large field of view images

We apply the nucleus detector to a mosaic consisting of eight overlapping images of 3 day detached cat retina (Figure 4.10).

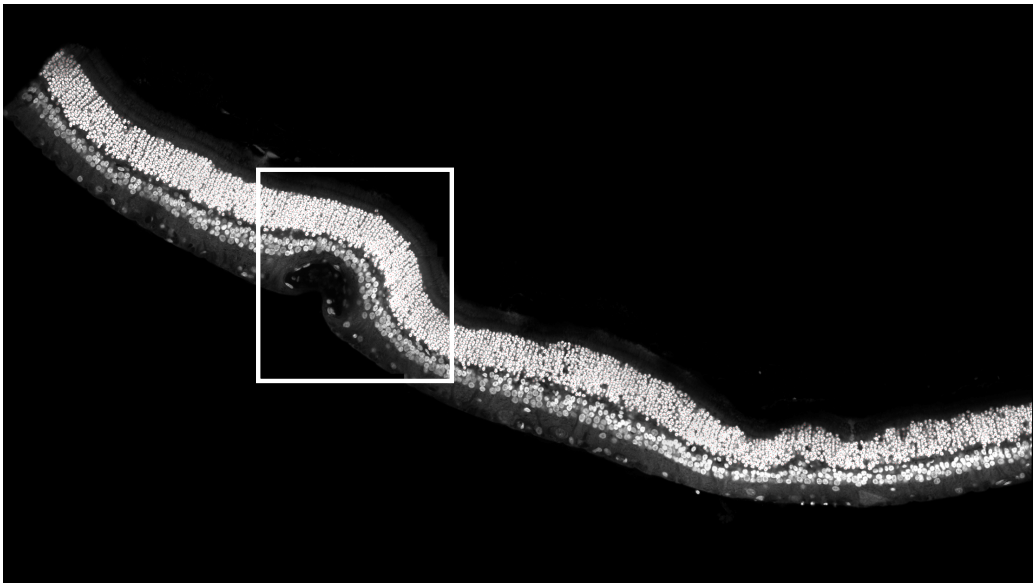

(a)

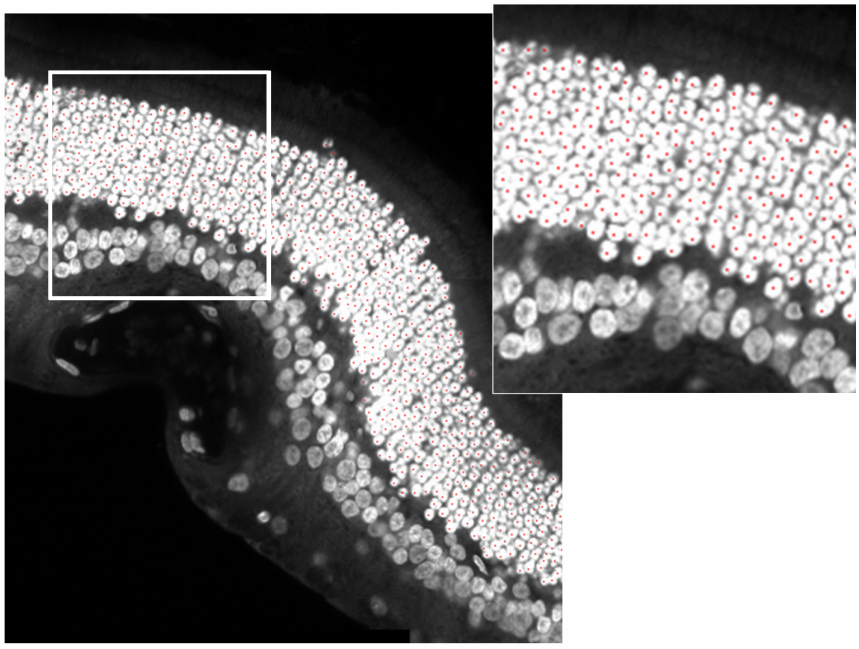

(b)

Figure 4.10: Application to large images. (a) A 2.8 mega pixel montage automatically assembled using eight confocal images of 3-day detached cat retinas stained with TO-PRO. Detected cell centers are marked with red dots. A portion of image (a) boxed is displayed at higher magnification and subsequently the boxed area in (b) is shown at higher magnification.

These images are acquired with 5 to 20% overlap in order to align multiple images automatically. The registration technique used is based on the automatic detection of feature points; the estimation of the transformation is obtained using robust estimators on the putative matches obtained matching the intensities of the point neighborhoods [41]. This technique has been widely used to register remote sensed images. To ensure high quality results containing the maximum amount of original unchanged data blended without blur and abrupt intensity differences, a modern blending technique is used [24]. By using a mosaic, the photoreceptor nuclei can be counted over a large area of the cat retina without sampling within a tissue. There is a large amount of work to estimate cell numbers from the average cell density of the region in which counting boxes are distributed [3, 35, 83]. From this work, it has been determined that the larger the tissue and steeper the gradients in cell density, the greater the margin of error. The proposed nucleus detector overcomes these potential errors because no assumptions are made about size, shape or regional difference in cell density. Therefore, it provides not only reliable results with greater confidence but also greater insight into relationships between cellular responses and the location of the sample in the retina.

4.3.3 Applicability to varying sample preparation

Application to laser scanning confocal images stained with antibodies

We apply our method to confocal images stained with various antibodies that did not recognize nuclear antigens. Thus, in the images used, the antibodies do not identify the nuclei above background levels. Since confocal retinal images are generated by using fluorescence, only specific regions where fluorescent dye

molecules bind are visualized. Therefore, the brightness range within the image is very small. If the antibody does not bind to the ONL, then the ONL usually appears as a dark region where the intensity value of a pixel is close to zero (Figure 4.11 (a)). The histogram shown next to the image is a plot of number of pixels at each of the 256 possible brightness levels. The narrow peak indicates that only a few of the levels are represented. Since the brightness range within the image is very small, there is not enough contrast to visualize structures within the ONL. Therefore, the visibility of the ONL structures should be improved by stretching contrast so that the value of pixels are reassigned to cover the entire available range, thus making the nuclei visible. We apply a histogram equalization method [69] to the image so that individual nuclei within the ONL can be discriminated (Figure 4.11 (b)). This histogram plotted with the image in Figure 4.11 (b) now shows counts of pixels for gray levels that are spread out across the available brightness scale.

The results show that the proposed method estimates the location of a cell body even though the antibody used does not recognize and bind to nuclear portions of the cell (Figure 4.11). In this context, cell counting does not need to be limited to results obtained with nuclear specific stains such as TO-PRO and DAPI. Furthermore, our nucleus detector performs better than manual counting especially where the contrast of the region is low. The contrast of images is computed by using Michelson's contrast measure[2][54].

[2]Michelson's contrast measure is used to measure the contrast of a periodic pattern and defined as follows:

$$C = \frac{f - b}{f + b}, \tag{4.2}$$

where f and b is the maximum luminance and the minimum luminance values, respectively, in the image. C varies from 0 to 1.

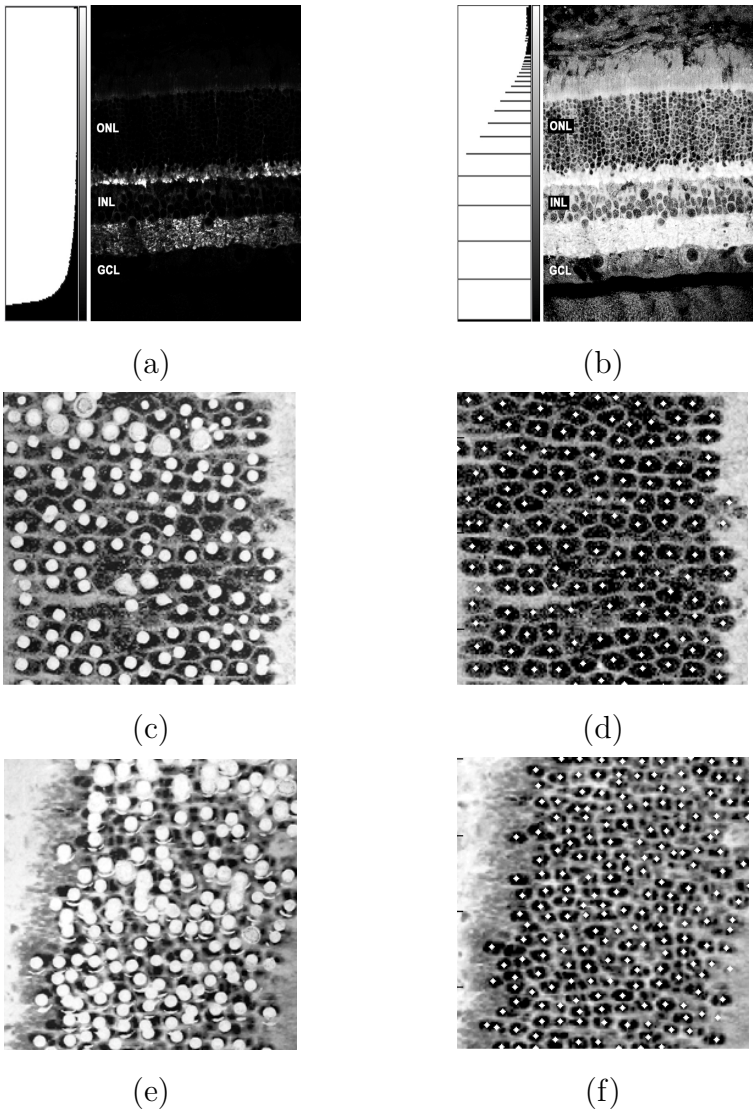

Figure 4.11: Application to images stained with various antibodies that are not specific to nuclei. (a) Example of a single labeled image of synaptic terminals (anti-synaptophysin). The staining did not provide any contrast to nuclei. (b) Histogram equalized image shows a full range of black to white values. (c) and (d) Histogram equalized images of the retina labeled with anti-vimentin; (e) and (f) Histogram equalized images of the retina single labeled with anti-neurofilament. A comparison of images manually counted and counted with the nucleus detector are shown. (c) and (e) Manually counted images. The nuclei were counted on the printed paper by placing dots over the nuclei. The paper was scanned to create a digital image. (d) and (f) Nucleus detector. White dots on the image represent detected nuclei. Manual counting produces the result with large variations for the image with low contrast (C=0.5) (see footnote 2).

We define f as the mean gray-level value of nuclei in the image, and b as the mean gray-level value of a surrounding region. This definition of contrast is independent of the actual range of gray levels in the image, so is well suited for measuring contrast in histogram equalized image. Figure 4.11 (c) shows an example of a high contrast image (C=0.86). Both manual counting and nucleus detector produce a good result (Figure 4.11 (c) and (d)). When the contrast of the image is low (Figure 4.11 (e) (C=0.5)), the manual counting result shows a large variation in cell counts (23% of variation in three independent counting). Since our approach estimates local maxima of the filter output, the nucleus detector still can identify individual nuclei even when the contrast of the region is low or the intensity within the region varies dramatically.

Application to bright-field images of retina

We also apply the nucleus detector to images generated by transmitted light microscopy of normal mouse retina (Figure 4.12). The filter size is set to 30 pixels and the minimum distance between blob centers is set to 15 pixels (filter size×0.5), which is the same optimal parameter calculated from feline retina. There are two types of nuclei in the image: bright and dark nuclei. Since bright nuclei (denoted by white arrows in Figure 4.12) have a poor contrast (C=0.5), they are often missed by manual counting. The result shows that the proposed method can detect most of bright nuclei well without fine tuning of parameters.

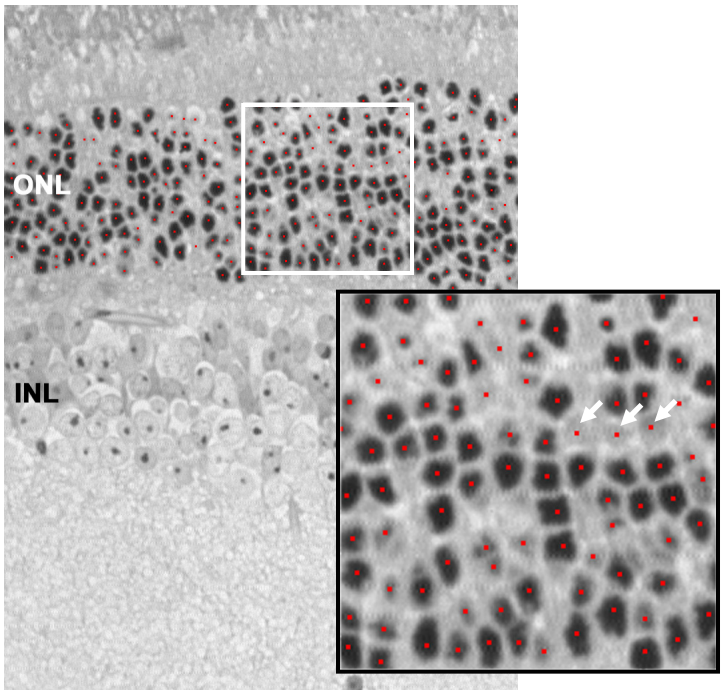

Figure 4.12: Light micrograph of a normal mouse retina. The tissue was embedded in resin and stained with Toluidine blue . The contrast between nuclei and the rest of tissue is low compared to specific nuclear dyes. In particular, bright nuclei denoted as white arrows display the poor contrast (C=0.5), they are often missed by manual counting. The proposed method can detect most of bright nuclei. Red dots on the image represent detected nuclei.

Application to other images

We test the proposed method with various images without tuning parameters. Figure 4.13 (a) shows an image of cultured cells and demonstrates that nuclei can be detected with a single filter even though the size of nuclei within the image are all different. Even though the blob is bigger or smaller than the designed filter, the value of filter output is still the local maximum at the center of the blob. Therefore, searching local maxima of the filter output enables detecting various sizes of blobs.

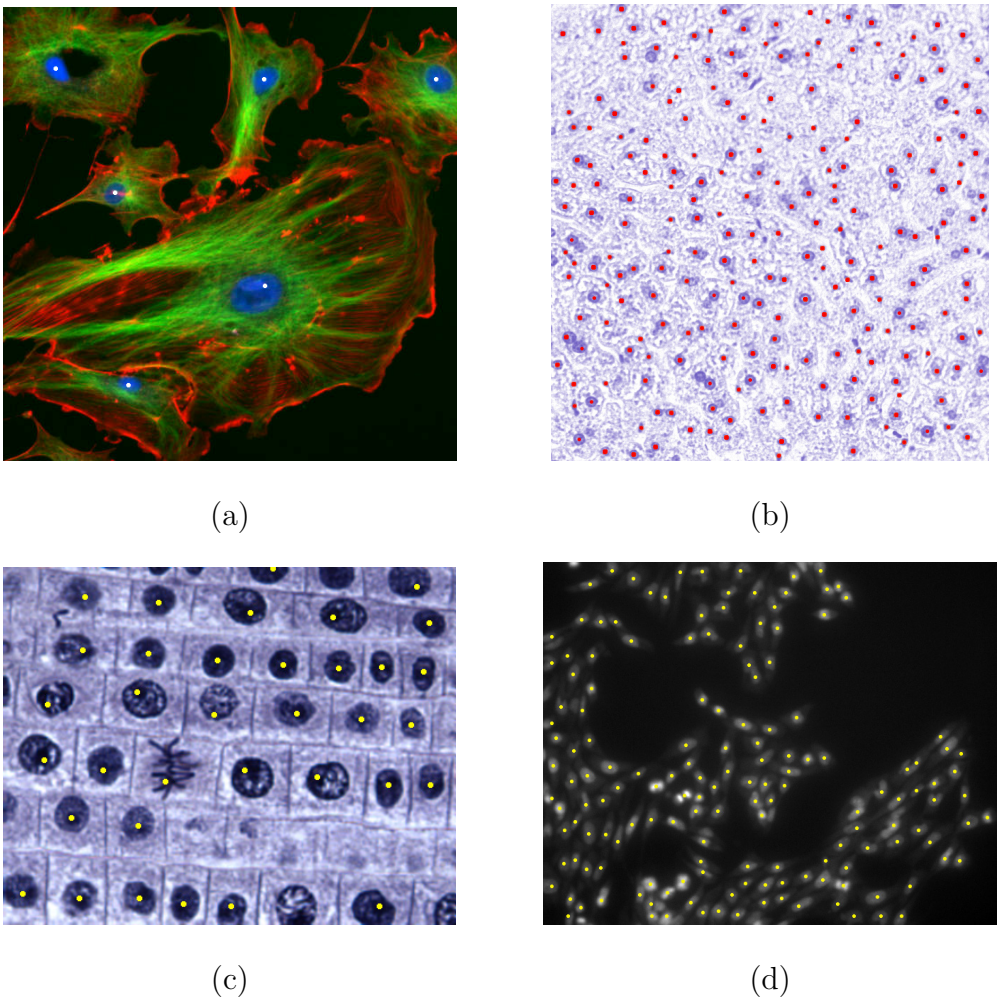

(a) (b)

(c) (d)

Figure 4.13: Application to nucleus detector to different types of images. (a) A fluorescent cell image acquired by an epi-fluorescent microscope (downloaded from [36]): actin (red), β-tubulin (green) and nuclei (blue). Six nuclei are detected. (b) A transmitted light microscopy of a tissue from the liver stained with H & E. 233 nuclei are detected. (c) An allium image collected by a transmitted light microscope. 33 cell bodies are detected (d) Adhering cell image stained with DAPI acquired by epi-fluorescent microscope. 158 nuclei are detected.

Similarly, Figure 4.13 (b) shows an image of tissue section collected from the liver that consists of various sizes of cell bodies stained with Haematoxylin and Eosin (H & E). All cells are composed of a nearly infinite combination of the various hues and shades of these two stains. By applying a single filter with a median size cell body within an image, we still can detect all cells successfully despite of poor contrast of an image. More results are shown in Figure 4.13 (c) and (d). Since the proposed method assumes the blob as a circular object, the filter output will have multiple local maxima within the blob using the filter designed for single-lobed blobs. Such multiple local maxima result in double detected cells. However, they can be easily eliminated by checking the number of local maxima within each connected component. Estimating local maxima can result in detecting some false positive blobs, but they could also be eliminated by tuning the parameters.

4.4 Summary

We described a nucleus detector that automatically detects the number of nuclei in digital micrographs and can thus be used for counting cells. Initially, we evaluated the performance of the nucleus detector with confocal images of feline retina but found it useful for a wide variety of preparations. For detecting photoreceptor nuclei, the nucleus detector performs very well with an average error of 3.67% ranging from 0.00 to 6.07%. The advantages of the proposed method are its simplicity and reliability to detect any blob-like structures such as nuclei. Moreover, it is computationally efficient so it is applicable to use across large expanses of tissue eliminating the need for regional sampling which causes errors. It

is especially valuable for tissue with a steep gradient in cell number, i.e. with distinct layers, such as brain and retinal tissue. Additionally, the proposed method can be used on a variety of sample preparations or imaging methods, indicating its widespread applicability. However, the method may not work correctly when the cell size and shape vary too dramatically since the method assumes that the cells have similar size and round shape. The proposed nucleus detector has been implemented as a plug-in for the public domain NIH image processing and analysis program, ImageJ [36]. The plug-in, ITCN (Image-based Tool for Counting Nuclei), has been visited 2784 times and the JAR file has been downloaded 1049 times from April to October 2006. The nucleus detector with sample images and instructions are also available at the Center for Bio-image Informatics.

Chapter 5

Photoreceptor Nucleus Detection and Its Applications

Quantifying the deformation of retinal tissue after injury is crucial in understanding and characterizing the functional effect of cellular changes. We extend the nucleus detection method in Chapter 4 and propose *a fully automated* nucleus detection approach for counting photoreceptor nuclei within the outer nuclear layer (ONL). We automatically detect a cell size by identifying the intrinsic structure of a point neighborhood within the ONL based on condition theory [86] (see Section 5.2). Based on the nucleus detection results, we also automatically measure the thickness of the ONL and the local cell density within the ONL. These measurements provide the first thorough quantitative analysis of retinal images. Our results not only verify previous conclusions about retinal restructuring during detachment, but also provide us with new insights into the regional responses in the ONL (see Section 5.3).

5.1 Introduction

Although quantifying the deformation of retinal tissue after injury is important for understanding the functional effect of cellular changes, there are only few quantitative measures: the number and density of photoreceptor nuclei within the ONL, and the thickness of the ONL. These measurements are currently done manually and it is not often feasible to perform manual analysis on all samples collected. Thus the measurements have been done on only a few sparse locations throughout the retina [77, 4]. For example, the total cell number of a whole retina is often extrapolated based on the measured data from a few locations. Such an extrapolation method can easily mislead us to a biased conclusion depending on the sampling location (See section 5.3.2).

In this chapter, *a fully automated* nucleus detection approach for counting photoreceptor nuclei within the ONL is proposed. Any user input is completely eliminated by segmenting a region (ONL) and estimating filter size based on condition theory. The automated approach allows a large sample size for analysis and leads to a reduction in sampling error. Based on the nuclei detection results, we introduce the first thorough quantitative analysis for retinal images not only corroborated by conclusions derived from manual measurements and qualitative assessments, but our analysis also provides significant information about local structural changes during retinal detachment [10, 9].

This chapter is organized as follows. We first propose a fully automated method tailored to detect photoreceptor nuclei within the ONL from confocal images of retinas (Section 5.2). The mathematical framework for identifying the characteristic dimension of a cell size is provided in Section 5.2.2 and the approach

is experimentally evaluated. Finally, a novel method to quantify the structural distortion of a retina based on the nucleus detection result is introduced. The nuclei within the ONL are automatically detected and based on the results, the thickness and density profiles of the ONL and their distortion indices are computed (Section 5.3).

5.2 Photoreceptor Nucleus Detection

We mainly focus on fully automating photoreceptor nucleus detection from the retinal images collected by confocal imaging. A schematic diagram of our approach is shown in Figure 5.1. A given image is segmented by statistic-based clustering (Section 5.2.1). Within the resulting segmented region, ONL, the cell size (e.g. photoreceptor cell size) is estimated based on condition theory (Section 3.1), and the filter size and the minimum distance between cells are computed based on the determined cell size. The rest of the approach is the same as the nucleus detector described earlier (Figure 4.4).

5.2.1 Statistic based clustering

Since we are interested in detecting photoreceptors within the ONL, the first step is to delineate the ONL. The confocal images stained with nuclear dyes (e.g. TO-PRO or DAPI) visualize all nuclear layers in a retinal image. One simple way to segment these nuclear layers is thresholding: individual pixels in an image are marked as 'nuclear layer' pixels if their value is greater than a defined threshold value and as 'background' pixels otherwise [69, 32]. Typically, a resulting image

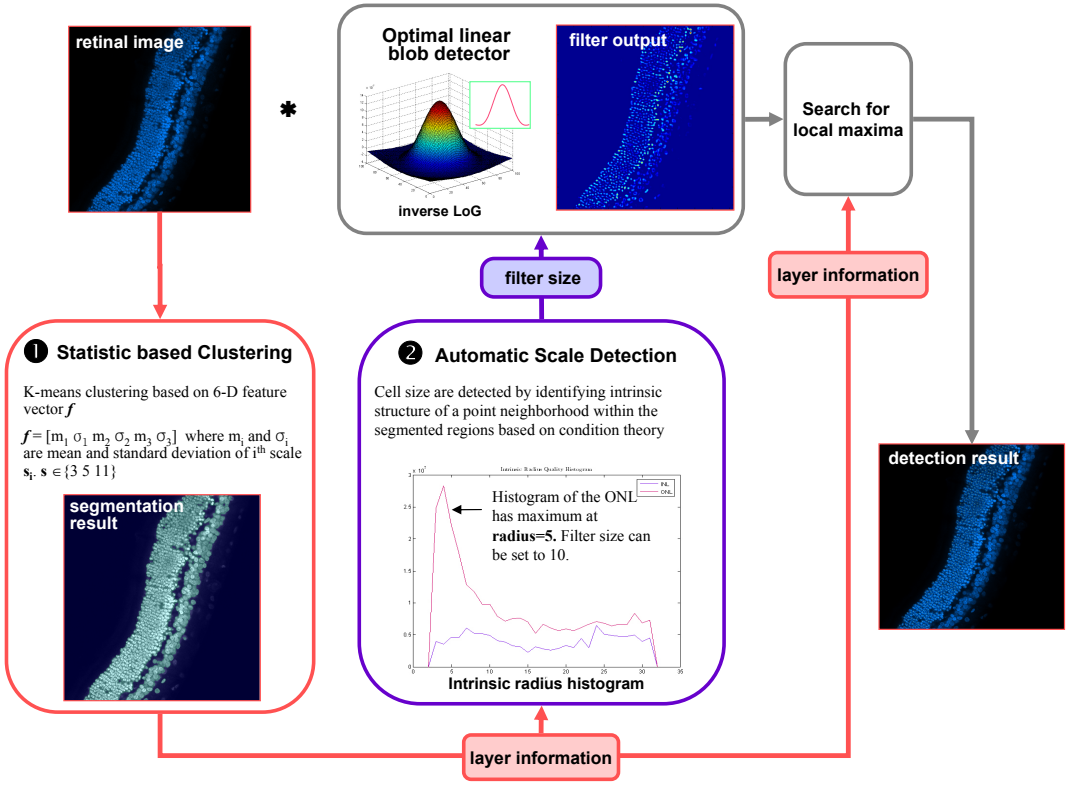

Figure 5.1: A schematic diagram of a fully automated nucleus detection method. The ONL is automatically segmented by statistic based clustering and cell size is detected by identifying the dominant characteristic dimension of the ONL. Using automatically detected cell size and segmented area, the blob centers are detected by filtering with the blob detector followed by searching local maxima.

is a binary or two-level image, using black and white or other colors to distinguish the regions. The key parameter in thresholding is the threshold itself. A common approach to choose a threshold is to create a histogram of the image pixel intensities and choose a threshold as a value between two peaks. The histogram approach assumes that there is some average value for the background and object pixels, but many image histograms do not have clearly defined peaks that correspond to structures in the image. The retinal image is a typical example whose

histogram does not form distinctive peaks due to intensity variation caused by uneven staining. Moreover, the range of intensity of nuclear layers varies dramatically across the images. Such variations are caused by an uneven staining across the tissue section, which in turn leads to inconsistent setting of laser intensity, gain (Section 2.3.3). Therefore, applying simple thresholding to a set of images will result in inconsistent segmentation.

To cope with intensity variations in nuclear layers, we introduce a statistic-based clustering based segmentation. The main idea is to cluster all pixels within an image into two classes, nuclear layer and background, in order to capture the global characteristics of the image. For each pixel, the mean and standard deviation of various size of N×N neighborhood are computed and used as a feature vector (Figure 5.2 (a)).

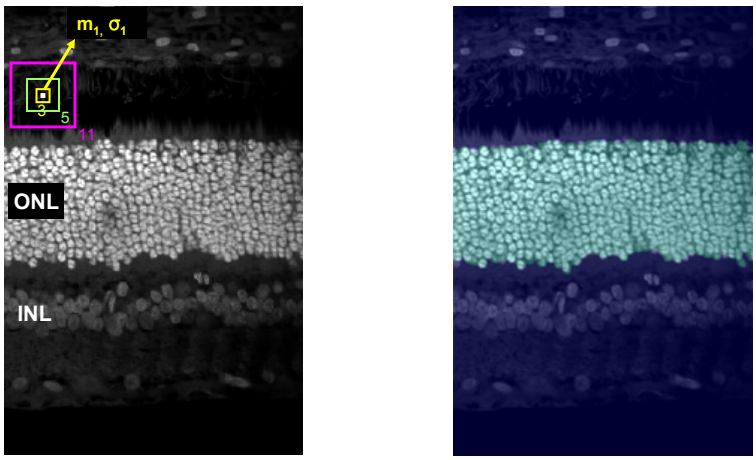

(a) (b)

Figure 5.2: Statistic based clustering. (a) Example image of normal cat retina stained with TO-PRO illustrating nuclear layers. (b) Segmentation result overlayed on its original image. For each pixel in the image, a feature vector $\mathbf{f} = [m_1, 0.5 \cdot \sigma_1, m_2, 0.5 \cdot \sigma_2, m_3, 0.5 \cdot \sigma_3]$ is calculated where scale $\mathbf{s_i} \in \{3, 5, 11\}$. and then clustered into two classes by K-means clustering.

The mean values of each pixel in nuclear layers are higher than those in background (Figure 5.3 (a), (b), and (c)). Using the average intensity value of each pixel instead of the intensity value itself, allows a robust segmentation of nuclear layers despite their intensity variation. The standard deviation captures texture information present in an image. Since each nuclear layer consists of different types of cells, it presents a similar texture in different scales. Figure 5.3 (d), (e), and (f) show computed standard deviation of 3×3, 5×5, and 11×11 neighborhood of each pixel. The combination of these standard deviations of each pixel provides a clear distinction between the ONL and the other nuclear layers. In summary, a feature vector consists of mean and standard deviation of n different scales,

$$\mathbf{f} = [m_1, \omega \cdot \sigma_1, \ \cdots \ m_n, \omega \cdot \sigma_n], \tag{5.1}$$

where m_i and σ_i are the mean and standard deviation of the i^{th} scale s_i, $\mathbf{s} \in \{3, 5, 11, \cdots\}$, and ω is defined as $0 < \omega \leq 1$. ω plays the role of a weighting factor. The resulting feature vectors are classified using K-means clustering. K-means clustering [21, 5, 48] is a simple unsupervised learning algorithm that classifies or groups objects based on features into K clusters. The clustering is done by minimizing the sum of squares of distances between data and the corresponding cluster centroid. Figure 5.2 (b) is a segmentation result overlayed on its original image illustrating a successful segmentation of the ONL. More results are shown in Figure 5.4. In Figure 5.4 (b), the ONL and the inner nuclear layer (INL) are segmented accurately. The INL can be easily excluded by selecting the biggest segmented region from the result, or changing a weight for a standard deviation. While Figure 5.4 (c) shows more dramatic intensity variations within the image, all nuclear layers are segmented correctly.

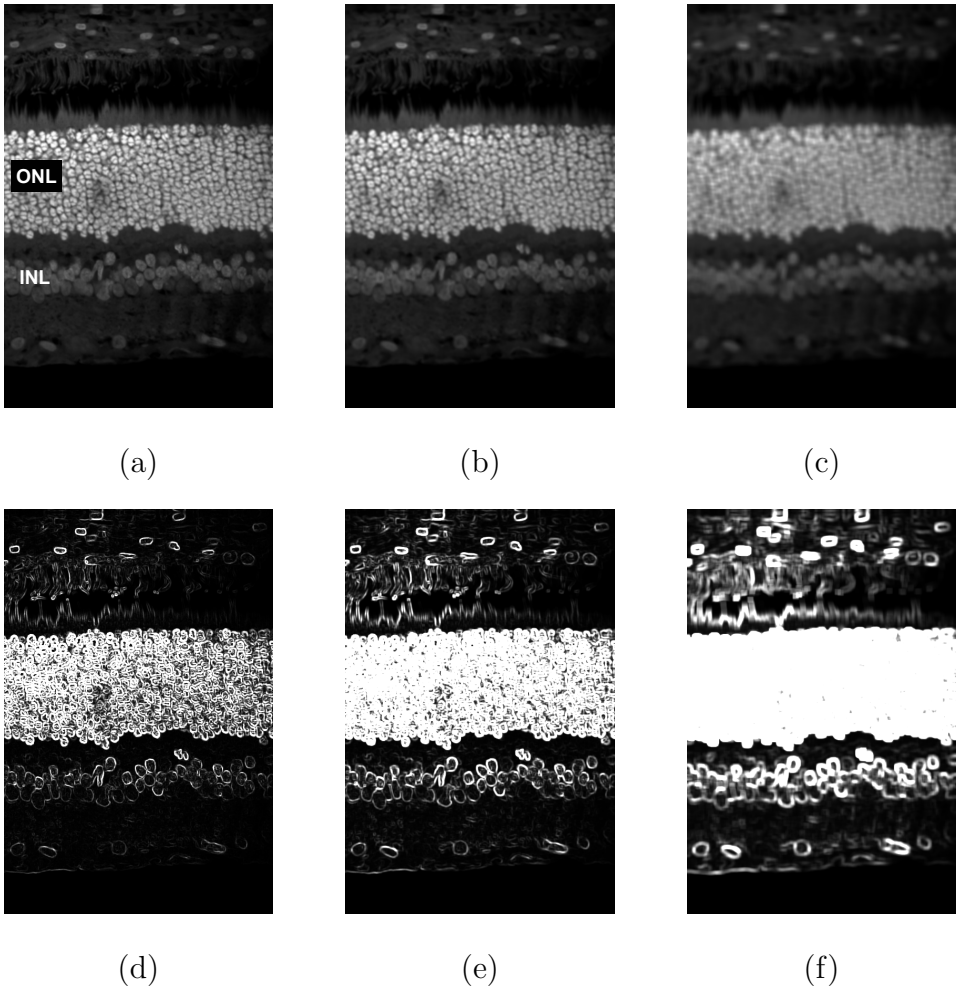

Figure 5.3: Application of filters at various scales to Figure 5.2. (a), (b), and (c) Applying average filters to the image. Each pixel in the image contain the mean value of 3×3, 5×5, and 11×11 pixel neighborhood respectively. The mean values of each pixel in nuclear layers are higher than those in background. (d), (e), and (f) Standard deviation of 3×3, 5×5, and 11×11 pixel neighborhood. The results capture the texture at different scales. The combination of these standard deviations of each pixel provides a clear distinction between the ONL and the other nuclear layers.

However, the method can not produce a reliable result from the image stained with antibodies which do not stain DNA, since only specific regions in the image are visible by fluorescent dyes. Most of layers including the ONL usually appear as dark regions, thus the intensity information can not give enough information to discriminate the nuclear layers from other regions.

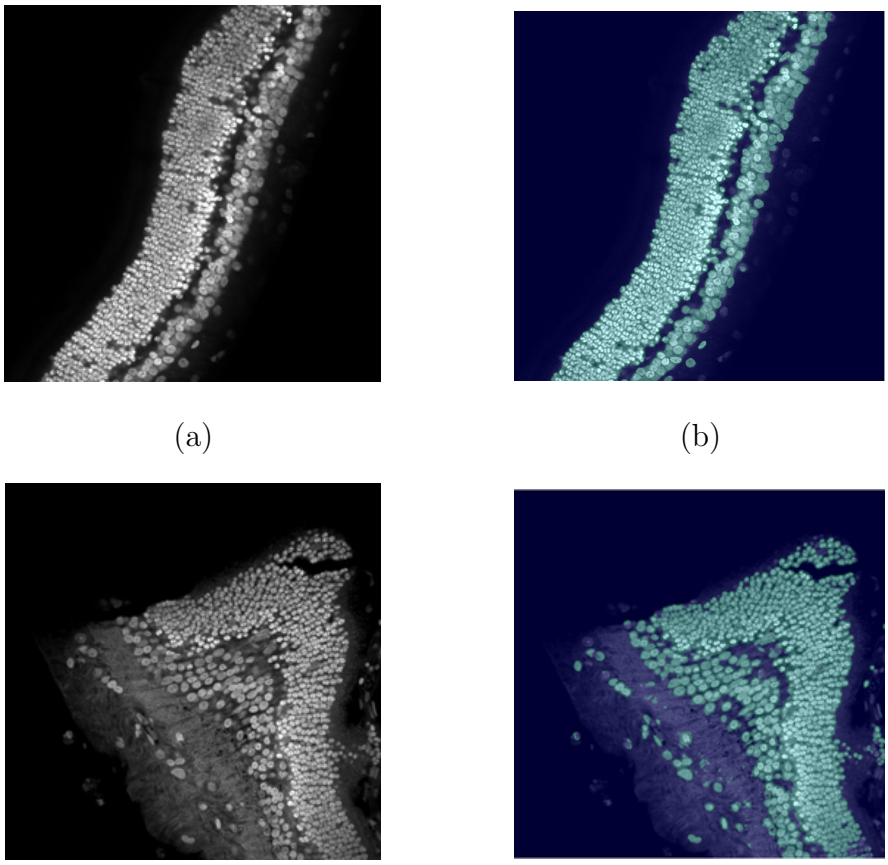

(a) (b)

(c) (d)

Figure 5.4: Applying statistic based clustering to images of 3-day and 7-day detached retinas. (a) 3-day detached cat retina stained with TO-PRO. (b) Segmented result of (a). $\mathbf{f} = [m_1, 0.5 \cdot \sigma_1, m_2, 0.5 \cdot \sigma_2, m_3, 0.5 \cdot \sigma_3]$ is calculated where scale $\mathbf{s_i} \in \{3, 5, 11\}$. The ONL and the INL are segmented accurately. The INL can be easily excluded by selecting biggest segmented region from the result. (c) 7-day detached retina. (d) Segmented result of (c). The feature vector is computed similarly.

5.2.2 Applying condition theory to a nucleus detection

We apply a condition theory based framework to retinal images stained with TO-PRO and acquired using four different magnification factors (Figure 5.5). The same photoreceptor nuclei are displayed in different scales.

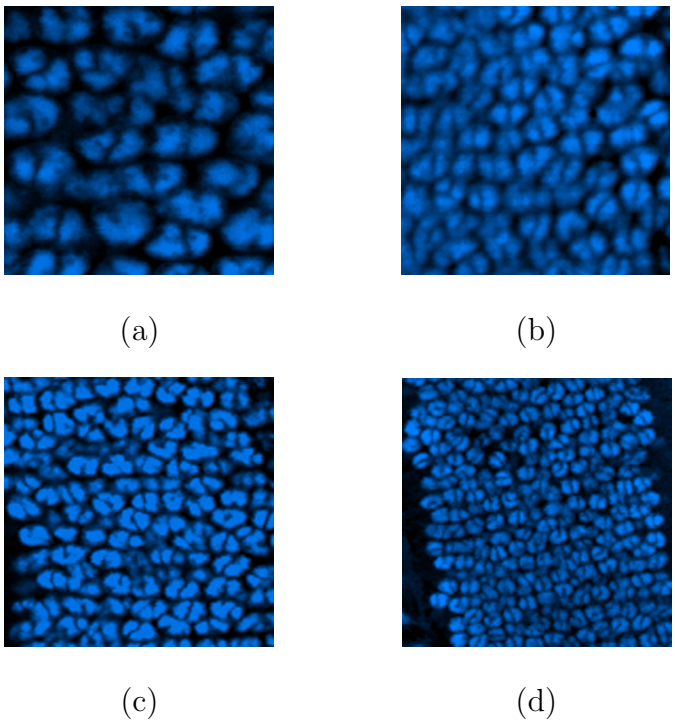

(a) (b)

(c) (d)

Figure 5.5: Example images of the ONL stained with TO-PRO and acquired with different magnification factors. The same photoreceptor nuclei are displayed in different scales. (a) The image is collected with a pixel resolution, 0.621 μm per pixel. (b) The resolution is 0.414 μm per pixel. (c) The resolution is 0.3241 μm per pixel. (d) The resolution is 0.207 μm per pixel.

To detect the photoreceptor nuclei within the ONL, we follow three steps:

- Identify the ONL from the image.
- Verify the presence of dominant characteristic dimensions r^* within the ONL.

- Estimate the cell size, assuming their dimension is proportional (via known constant) to r^*.

Since we already segment the ONL by statistic based clustering (Section 5.2.1), we focus on the second and the third steps in this section.

Identifying the dominant characteristic dimensions of the ONL

Let M be the region corresponding to a given segmented ONL. To identify its dominant characteristic dimension, M is spatially sampled at the points $\boldsymbol{x}_1, \ldots, \boldsymbol{x}_N$ and at each point we calculate the condition number (3.4) for the radii $r_1, \ldots, r_n$ using the ∞-Schatten norm[1]

$$\hat{K}_{\boldsymbol{T}_{\boldsymbol{\theta},\boldsymbol{x}}}(\Omega_r(\boldsymbol{x})) = \frac{1}{\|A^{\dagger}(\Omega_r(\boldsymbol{x}))\|_{\infty,S}} = \sigma_4(A(\Omega_r(\boldsymbol{x}))) \tag{5.2}$$

where $\sigma_4(A(\Omega_r(\boldsymbol{x})))$ denotes the fourth (i.e. the smallest) eigenvalue of the matrix A[2]. This norm measures the maximum distortion produced by the noise in the intensity pattern in $\Omega(\boldsymbol{x})$. The value of r for which the condition number $\hat{K}_{\boldsymbol{T}_{\boldsymbol{\theta},\boldsymbol{x}}}$ has a local minimum are used to compute an histogram whose peaks identify the dominant characteristic dimensions of the layer M.

[1]The c-Schatten norm of a matrix $M \in \mathbb{R}^{h\times k}$ is defined as the c-norm of the vector formed by the matrix singular values, i.e. :

$$\|M\|_{p,S} = \left[\sum_{i=1}^{\min\{h,k\}} \sigma_i(M)^c\right]^{\frac{1}{c}}$$

where $\sigma_i(M)$ denotes the i^{th} singular value of M.

[2]For sake of completeness, the expression of the building blocks of A for the transformation (3.7) is:

$$A(\boldsymbol{y}_i) = \frac{\partial \boldsymbol{I}}{\partial \boldsymbol{y}}(\boldsymbol{y}_i) \begin{bmatrix} 1 & 0 & y_1 - x_1 & -(y_2 - x_2) \\ 0 & 1 & y_2 - x_2 & y_1 - x_1 \end{bmatrix}$$

Figure 5.6 (b) shows the points $\boldsymbol{x}_1, \ldots, \boldsymbol{x}_N$ that are sampled from the ONL. We perform a probabilistic sampling instead of a uniform sampling. The main purpose of using a probabilistic sampling is to avoid selecting the corner points within the ONL. In general a corner point remains very distinctive even after being perturbed by noise, and therefore its condition number is smaller than those of other points within an object (i.e. points within a cell body). However, its histogram presents a characteristic dimension of corners created by the cell membrane, not a cell body. To estimate the dimension of a cell body, we sample the points which belong to the inside of a cell so that the sampled points can contribute to estimate a characteristic dimension of cells. First, we segment the region containing cell bodies by an adaptive thresholding followed by morphological operations, and compute the Euclidean distance transform of the inverted resulting binary image. For each pixel belongs to the background, the distance transform assigns a distance between the pixel and the nearest nonzero pixels of the image (i.e. background). The closer a pixel $\boldsymbol{d}$ to the cell center, the higher the distance value in the result image. We use the distance value of each pixel as a random variable, and define the probability density function as follows,

$$f(\boldsymbol{d}) = e^{\frac{-(d_{max}-\boldsymbol{d})}{\sigma}}, \tag{5.3}$$

where $\sigma = \rho(d_{max} - d_T)$, d_{max} and d_T denotes the maximum value of the distance values of the image and the threshold value respectively. When the distance value of the pixel is close to d_{max} (the pixel is close to the cell center), the pixel is likely to be selected in the sampling process.

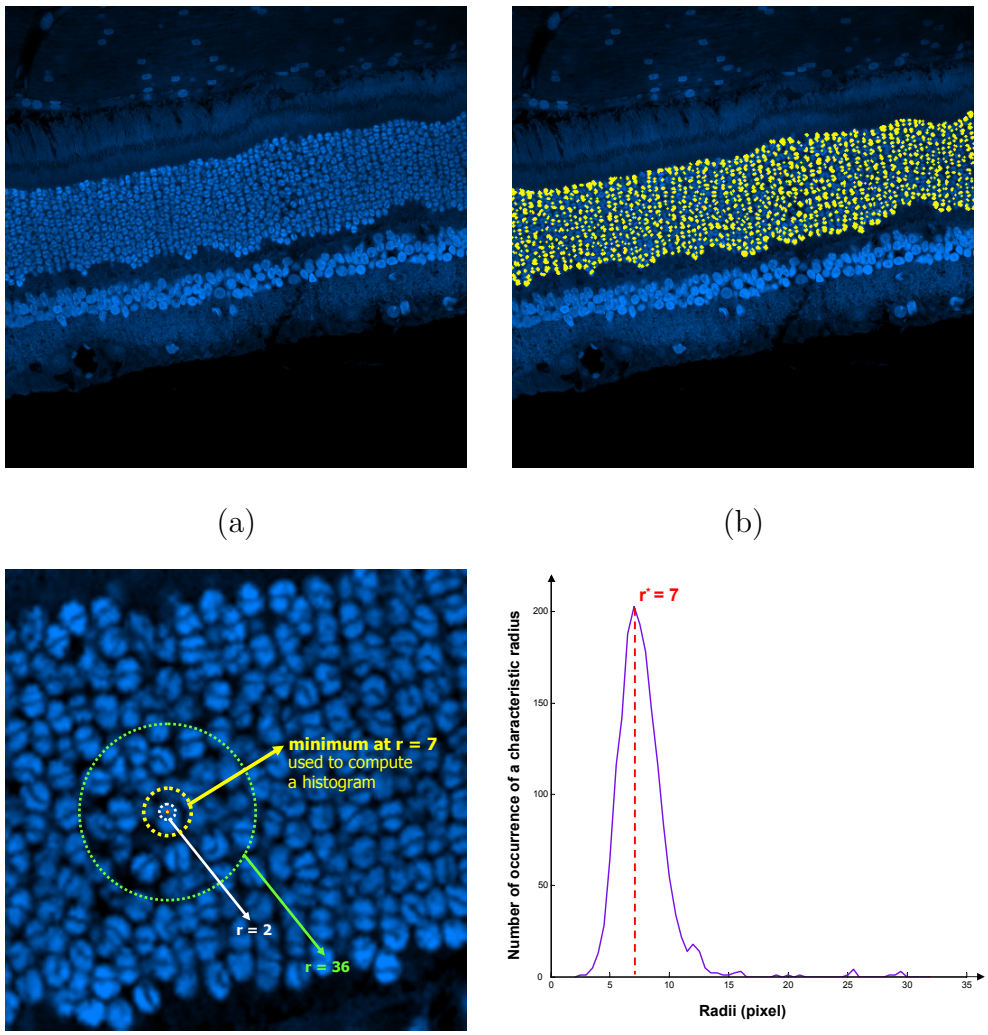

Figure 5.6: Identifying the dominant characteristic dimensions of the ONL. (a) An example image of a normal cat retina stained with TO-PRO. (b) The yellow dots indicate the location of which the ONL is sampled in order to construct the histogram (shown in (d)). (c) Illustration of computing a histogram. For a given point, the condition number of circular neighborhoods ranging from radius 2 pixels to 36 pixels. The value or the radius r for which condition number has a local minimum (in this example, $r = 7$) is used to compute the histogram. (d) A histogram of the characteristic radii of all sample points. The histogram present a very distinctive peak at 7 pixels that identifies the characteristic dimension of the ONL.

For each sampled point, the condition numbers are computed from neighborhoods $\Omega_r(\boldsymbol{x})$ where the radius $2 \leq r \leq 36$ (with increments of 0.5 pixels) and the condition number which has a local minimum. In this example, $r = 7$, is used to construct a histogram (Figure 5.6 (c)). The histogram is then computed using the values of the characteristic radius $2 \leq r \leq 36$ with increments of 0.5 pixels (Figure 5.6 (d)). The peak at $r^* = 7$ pixels reflects the characteristic dimension of the cells that comprise the ONL. Sometimes it may happen that the histogram presents two peaks that have similar height; this effect is due to the presence of repeating intensity patterns that are composed by more than just one fundamental unit (e.g. the membrane of the cell and its nucleus). To cope with these situations we select, among the peaks that have similar height, the one that is associated to the larger radius. In the implementation, rather than scaling the differentiation kernel to compensate for the exponential decrease of the amplitude of the derivatives, we choose to wrap the neighborhood $\Omega(\boldsymbol{x})$ on a normalized lattice obtained by sampling the unit circle.

Counting the photoreceptor nuclei within the ONL

In Section 4.2, we showed that the nucleus detector could detect photoreceptor nuclei with an average error of 4% compared to manual counting, when the cell size is known. The filter size f_s depends on the size of the cell and consequently on the image resolution. Here we propose to bind the filter size to the dominant characteristic dimension of the ONL using the approach described above. More specifically, the filter size is set as follows,

$$f_s = 2\lceil pr^* \rceil + 1 \tag{5.4}$$

where p is a scaling factor that depends on the structure of the image (and *not* on its resolution). In general, we expect the histogram to return a characteristic dimension slightly larger than the true size of the cell ($p < 1$) if the intensity pattern inside the cell is fairly uniform and, a dimension slightly smaller ($p > 1$) if the intensity pattern inside the cell contains relevant details. This is due to the fact that local minima of the condition number appear when the radius of the neighborhood is large enough to include a portion of the image that can disambiguate rotations and scalings despite the effects of the noise. An optimal p for the dataset is estimated by using the leave-one-out cross validation method.

5.2.3 Experimental results

The proposed method is applied to a set of 25 confocal retinal images stained with TO-PRO. We consider four groups of images acquired using different magnification factors as shown in Figure 5.5. The scaling factor p is set to 0.486 computed by the leave-one-out cross validation method. The performance of the method is also compared with an analogous approach that identifies the characteristic dimension of a neighborhood via the stationary points of the image Laplacian [56]:

$$L(\Omega(\boldsymbol{x})) = \left| \sum_{\boldsymbol{y}\in\Omega(\boldsymbol{x})} w(\boldsymbol{y}-\boldsymbol{x}) \sum_{j=1}^{m}\sum_{i=1}^{n} \frac{\partial^2 \boldsymbol{I}_j}{\partial y_i^2}(\boldsymbol{y}) \right|$$

In this case the stationary points and the actual value of the Laplacian are used to compute the histogram introduced above. The filter size is computed using equation (5.4) and the scaling factor p is set to 1.138.

The first experiment quantifies the performance achieved by the proposed ap-

proach in detecting the radius of the cells that compose the ONL.

Figure 5.7 illustrates the detected radii of 25 images by the proposed method, the method based on the image Laplacian, and the true sizes computed from the metadata.

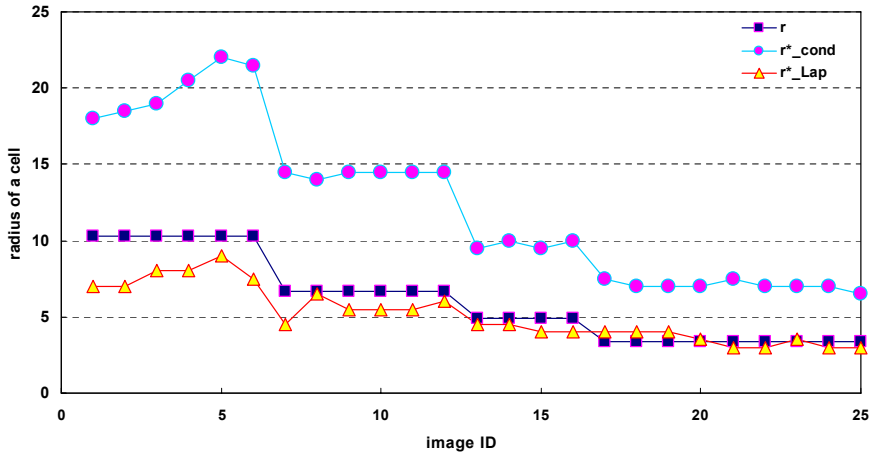

Figure 5.7: Results of detecting the radius of the cells that comprise the ONL. The radius of true cells, r, in each image are denoted by a rectangular marker. The proposed method (denoted by a circular marker) estimates a cell size larger than the true size, yet consistently. On the other hand, the result based on the image Laplacian (denoted by a triangle marker) usually underestimate a cell size. When the true cell size is small ($r < 5$), Laplacian based method fails to discriminate the cell size in two different scales (Figure 5.5 (c) and (d)) correctly.

The proposed method (denoted by a circular marker) estimates a cell size larger than the true size, yet consistently. On the other hand, the result based on the image Laplacian (denoted by a triangle marker) tends to produce histograms that have multiple spurious peaks and usually underestimate the characteristic dimension of a layer. For example, when true cell size is small ($r < 5$), Laplacian based method fails to discriminate the cell size in two different scales (Figure 5.5 (c) and (d)) correctly. This can probably be explained by the fact that the image

Laplacian is constructed from the second derivatives of the image and therefore tends to be more sensitive to small spurious structures that characterize the intensity pattern. The results are summarized in Table 5.1 and are compared with the method based on the image Laplacian described above. The relative errors between the true radius r and the estimate r^* are defined as

$$e_{r,Cond} = \frac{|r - pr^*_{cond}|}{r}, \quad e_{r,Lap} = \frac{|r - pr^*_{Lap}|}{r}.$$

Table 5.1: Summary of the automatic estimation results. Results are averaged over all images belonging to the same group. For each method we list the mean m, the median med, and the standard deviation σ of the relative error.

Type	r	$e_{r,Cond}$			$e_{r,Lap}$		
		m	med	σ	m	med	σ
A	10.3	0.08	0.07	0.06	0.14	0.14	0.00
B	6.7	0.05	0.05	0.01	0.09	0.07	0.07
C	4.9	0.03	0.03	0.03	0.06	0.06	0.01
D	3.4	0.02	0.00	0.04	0.15	0.17	0.16
Total	-	0.04	0.05	0.04	0.12	0.07	0.11

In the second experiment, we tune the filter size using the estimation of the cell radius obtained with the method presented here. The results are summarized in Table 5.2 and the performance is compared with a manual counting result (4.1) and the nucleus detector counts using the true cell size. The performance of the proposed method compares satisfactorily both to the case where the true cell dimension is known a priori (and is used to tune the size of the filter) and to the case where the cells are counted manually.

Table 5.2: Comparison between manual counts (N) and nucleus detector counts ($\hat{N}_{prior}$ and $\hat{N}_{cond}$) where the filter size is tuned by known priors and the proposed method.

Type	N	ND (nucleus detector counts) known priors		proposed method	
		$\hat{N}_{prior}$	$E_N, prior$ (%)	$\hat{N}_{cond}$	$E_N, cond$ (%)
A	218	204	6.42	282	29.36
	227	219	3.52	273	20.26
	189	178	5.82	207	9.52
	192	183	4.69	186	3.13
	195	179	8.21	168	13.85
	208	189	9.13	189	9.13
B	374	369	1.34	350	6.42
	392	371	5.36	352	10.20
	389	370	4.88	358	7.97
	388	367	5.41	356	8.25
	384	371	3.39	362	5.73
	428	378	11.68	366	14.49
C	412	422	2.43	450	9.22
	450	465	3.33	465	3.33
	453	482	6.40	515	13.69
	440	473	7.50	473	7.50
D	847	836	1.30	744	12.16
	773	790	2.20	790	2.20
	740	754	1.89	754	1.89
	736	759	3.13	759	3.13
	692	721	4.19	649	6.21
	700	734	4.86	734	4.86
	724	736	1.66	736	1.66
	751	730	2.80	730	2.80
	795	790	0.63	859	8.05
Total		-	4.49	-	8.60

Image type A,B,C,D are shown in Figure 5.5

5.3 Application to Quantify Structural Distortion of Retinal Tissues

In this section, we propose a novel method to quantitatively analyze and characterize structural distortion of a retina after injury. We automatically detect nuclei within the ONL in a retinal image (Section 4.2). Based on the nucleus detection results, we also automatically measure the thickness of the ONL, the local cell density within the ONL, and the distortion indices within the ONL (Section 5.3). These measurements not only verify previous conclusions about retinal restructuring after detachment, but also provide us with information about the regional responses within the layer of photoreceptor nuclei (Section 5.3.2).

5.3.1 Local thickness and density

Median extraction

To calculate the local thickness and density, the precise ONL boundary must be extracted from the image. We convert the (x,y) coordinates of detected nuclei centers into *on* pixels in a binary image. The ONL extraction is performed by two morphological operations on the binary image. First, a closing operation on the nuclei centers provides an approximation of the ONL. We use a disk with a diameter approximately six times the size of the photoreceptor as the structuring element. The relatively large diameter size ensures that the ONL can be extracted without any holes. Second, the morphological closing result is dilated by half a photoreceptor size, thereby extending the ONL to encompass the nuclei on the layer boundaries. Because there are large variations in intensity within the ONL,

segmenting the ONL using the nuclei detection results ensures that every detected photoreceptor nucleus is properly included within the ONL.

The ONL boundary is not naturally smooth and is usually curved along its length, therefore we compute a median curve and use it as the basis for the thickness and density measurement. Having segmented the ONL, we compute the median curve by pruning the skeleton of the ONL. The median extraction is summarized below. First, we use the *divergence-ordered thinning* algorithm proposed by [20] to calculate the total outward flux for each ONL. For every pixel p inside the ONL, the Euclidian distance $d(p)$ from p to the nearest boundary pixel is calculated. The result is a distance map D shown in Figure 5.8 (a).

(a) (b) (c)

Figure 5.8: Median extraction from the ONL. (a) Distance map D. (b) Total outward flux Φ. (c) Extracted medial axis overlayed on the nuclei detection result.

Next we compute the unit gradient of D using the $\vec{g}(p) = \nabla D(p)/|\nabla D(p)|$. From $\vec{g}(p)$, we calculate the total outward flux given by:

$$\Phi(p) = \sum_{i=1}^{8} < \vec{g}(p_i), \vec{n}_i >, \tag{5.5}$$

where p_i is an 8-connected neighbor of p and $\vec{n}_i$ is the unit vector pointing from p to p_i. The total outward flux result is shown in Figure 5.8 (b).

At pixel locations near the median, the gradient $\vec{g}(p)$ diverges and thus the flux $\Phi(p)$ is positive. Conversely, at locations where the gradient converges, the flux is negative. Using the outward flux map, the rough skeleton of the ONL is extracted by truncating all negative values of $\Phi(p)$ and thresholding the truncated result. The threshold level is chosen to minimize the variance of values above and below the threshold. Figure 5.8 (c) shows the result of this skeletonization step overlayed on the nuclei detection result. We prune the skeleton by removing side branches to extract the median curve. Information from the outward flux result is used to determine which side branch to disconnect. The final median curve is smoothed using cubic-spline interpolation. The smoothing is necessary to filter out noisy pixels resulting from the skeletonization.

Thickness and density profile

Once the median curve is extracted, it can be used to measure the thickness and density along the entire length of the ONL. For every location s_i along the median curve, a line $l(s_i)$ orthogonal to that median location is constructed and extended outward to the ONL boundaries (Figure 5.9 (b)). The thickness at location s_i is defined as the length of $l(s_i)$. Thickness measurements along the entire length of the median provide a continuous thickness profile as shown in Figure 5.9 (d). To compute the density at each median location s_i, a sliding region $A(s_i)$ bounded by $l(s_i - k \cdot ds)$ and $l(s_i + k \cdot ds)$ is constructed, where k is an integer parameter controlling the size of $A(s_i)$ and ds is the finite length element between adjacent median points (Figure 5.9 (c)). The density is defined as the number of nuclei located inside $A(s_i)$ divided by the area of $A(s_i)$. Figure

5.9 (d) shows the thickness and density profiles of the ONL in Figure 5.9 (a). The vertical line in the profile plots indicates the thickness and density of the ONL at location s_i in Figure 5.9 (c).

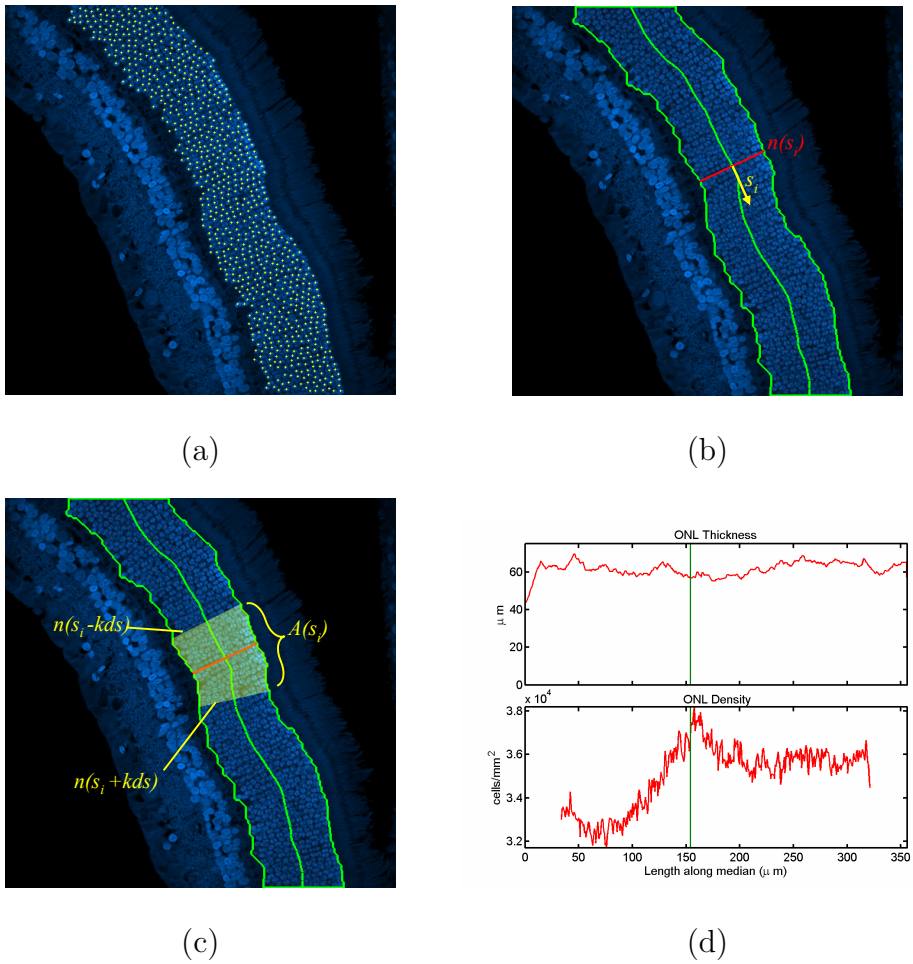

(a) (b)

(c) (d)

Figure 5.9: Thickness and density profile of the ONL. (a) The nuclei detection result. (b) Thickness. At every median element s_i, construct a line $n(s_i)$ orthogonal to s_i that extends to the boundary of the ONL. (c) Extracted median curve overlayed on the nuclei detection result shown in (a). (d) Thickness profile (top) and density profile (bottom). The vertical line in the profile plots indicates the thickness and density of the ONL at location s_i in Figure 5.9 (c).

Distortion index

Since thickness and density profiles provide information about local structural distortions in the ONL, it is useful to analyze the individual image. It is, however, difficult to compare these profiles with those computed from other images since the length of the median curve varies across the images. In order to quantify a global structural distortion of the ONL, we compute a distortion index of the thickness profile that is defined as

$$d_{thickness} = \frac{\sqrt{\frac{1}{N}\sum_{i=1}^{N}(t_i - m_T)^2}}{m_T}, \tag{5.6}$$

where $m_T = \text{mean}\{t_i\}$ and t_i = thickness at location (x_i, y_i) points on the median curve of the ONL. Similarly, we can compute a distortion index for the density profile. The more structural changes in the ONL, the larger the distortion indices. For example, $d_{thickness}$ for a normal retina is usually less than 0.2, and increases after detachment. The distortion index is useful for comparing the structural distortion among tissues from two or more different experimental conditions.

5.3.2 Experiment results

We demonstrate the capability of our method to extract multiple biologically meaningful measurements from images of cat and mouse retinal tissues.

Quantifying a structural distortion of *cat* retinas after detachment

We present the results of applying the proposed method to mosaicked images of control (9 images), 3-day detached (8 images), and 7-day detached (9 images) retinas (Figure 5.10).

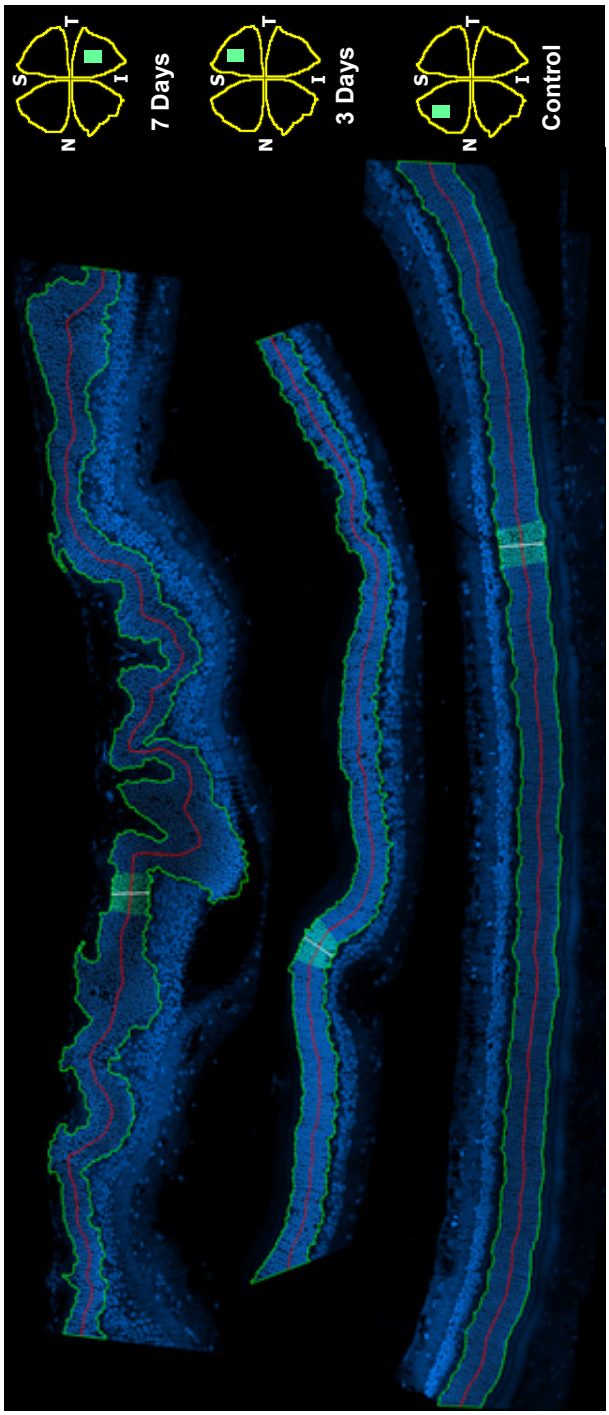

Figure 5.10: Mosaicked images of control (9 images), 3-days detached (8 images), and 7-days detached (9 images) cat retinas. Analysis results are overlayed on the images. In the right panel, the location of tissue sections are displayed as a green rectangle on the retinal quadrants.

To detect nuclei within the ONL, we first create a mask of the rough boundary of the ONL for each mosaicked image by a statistic based clustering (Section 5.2.1). After nuclei detection, we generate the ONL thickness and density profiles, and their distortion indices. In Figure 5.10, the detected nuclei centers, extracted ONL boundary, and the median curve of the ONL are overlayed on the images. The right panel illustrates a wholemount retina with four retinal quadrants (superior temporal (ST), superior nasal (SN), inferior temporal (IT), and inferior nasal (IN)). The green rectangle on each retinal quadrants denotes the location of tissue sections. To measure the global change in ONL thickness and density, we average the thickness and density measured over all points on the median curve (Figure 5.11). After 3-day detachment, the average thickness of the ONL is decreased to an average of 49.22 μm compared to control retina (62.94 μm, p$\leq$0.05).

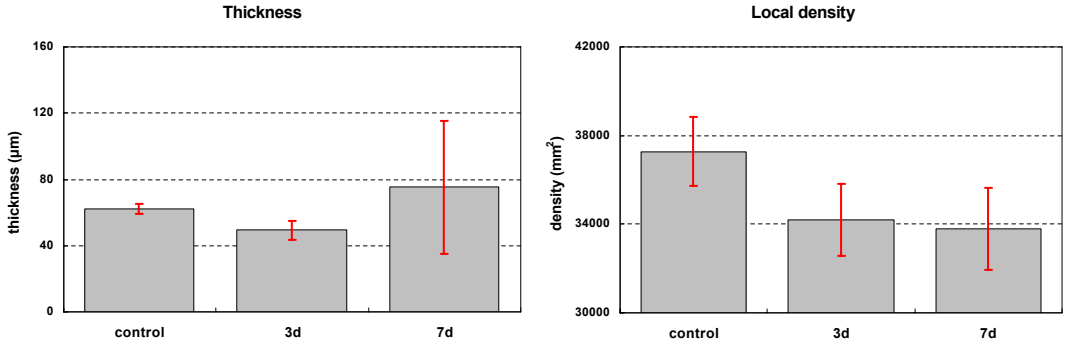

(a) (b)

Figure 5.11: Average thickness and density of control 3-day, and 7-day detached retinas shown in Figure 5.10. (a) Average thickness. The average thickness of the ONL is decreased from 62.94 μm in a control retina to 49.22 μm in a 3-day detached retina. The thickness of a 7-day detached retina is 75.31 μm due to retinal folding. Thickness changes are all significant (p$\leq$0.05). (b) Average local densities of the control, 3-day, and 7-day detached retina are 37283 nuclei/mm^2, 34180 nuclei/mm^2, and 33786 nuclei/mm^2 respectively. The density changes between normal and 3-days detached is significant (p$\leq$0.05), but there is no clear change between 3 days and 7 days detachment.

Similarly, average local cell density is decreased from 37283 nuclei/mm^2 to 34180 nuclei/mm^2. The quantitative cell counts and ONL thickness measurements confirm *the number of photoreceptors in the ONL decrease in response to retinal detachment*. This is the first thorough quantitative analysis that has been done, verifying earlier qualitative prediction in [27]. The average local densities of 7-day detached retina is 33786 nuclei/mm^2 indicating no clear change between 3 days and 7 days of detachment ($p>0.05$). The thickness of a 7-day detached retina, however, is increased to 75.31 μm with distinctively large variation of σ=40.17, which can be explained by a structural distortion of the tissue called retinal folding.

Figure 5.12 shows the ONL thickness and density profiles for each image. After detachment, the profiles of thickness and density vary irregularly. The changes in the profiles provide the information about the structural changes in the layer.

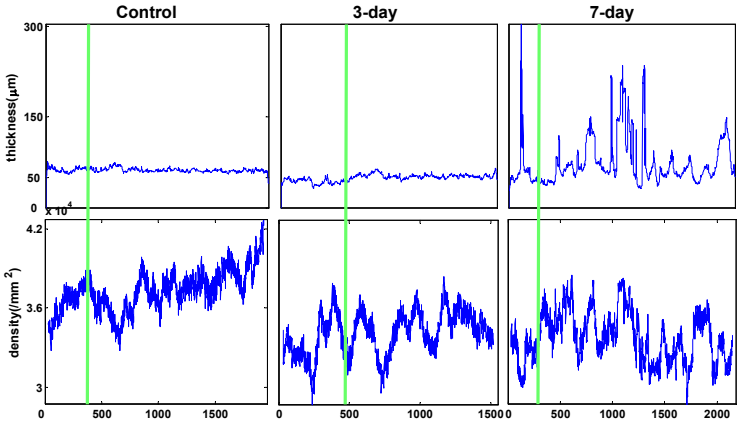

Figure 5.12: Thickness profiles (top) and density profiles (bottom). The distortion indices of the thickness profiles are increased from 0.05 to 0.11, and to 0.53 after 3-day and 7-day detachment respectively. After 3-day detachment, the distortion index of the density profile do not change significantly from 0.04 to 0.05. After 7-day detachment, the distortion index of density is increased to 0.06 indicating a large variation in cell density.

Notably, the peaks in the thickness profile indicate the locations where the retina has been folded by cellular movement, death, or growth. Such retinal folding in the retina results in an increase in the average thickness with large variation after 7-day retinal detachment shown in Figure 5.11 (a). To quantify the structural distortion, we compute distortion indices of thickness and density profiles from each image. The distortion indices of local cell density do not change significantly after 3-day detachment from 0.04 to 0.05. Usually a distortion index of a normal cat retina is less then 0.05. After 7-day detachment, the distortion index of density profile is increased to 0.06 indicating a significant variation in cell density. The distortion indices of thickness are slightly increased from 0.05 to 0.11 after 3-day detachment yet indicate no significant structural distortion. After 7-day detachment, the distortion index is increased from 0.11 to 0.53 suggesting significant regional deformation of a tissue. This information can not be extracted from traditional morphometric analysis. The thickness and density profiles, and their distortion indices clearly indicate that there are two critical problems of estimating the average measurement from sampled tissue sections:

- The extrapolated measurements can lead us to a biased conclusion based on the measured location. For example, if we measure the thickness and density at the location denoted as a green line in each profile shown in Figure 5.12, we might infer the naive conclusion that there is no significant changes in a cat retina after 7-day detachment. When a tissue has steeper gradients in cell density, the marginal error caused by sampling within a tissue become larger.

- Average thickness and density can not capture the structural distortion such

as retinal folding; even though the average thickness and local cell density do not change significantly, the distortion index of thickness profile indicates significant structural distortions in response to retinal detachment.

Quantifying a structural distortion of *mouse* retinas after detachment

We apply the nucleus detector to mosaics consisting of 13 overlapping images of control and 10 overlapping images of 3-day detached mouse retina. ONL thickness and density profiles for each image are also shown in Figure 5.13 (b). Figure 5.14 (a) and (b) show examples of retinal tissues with overlaid detected nuclei centers.

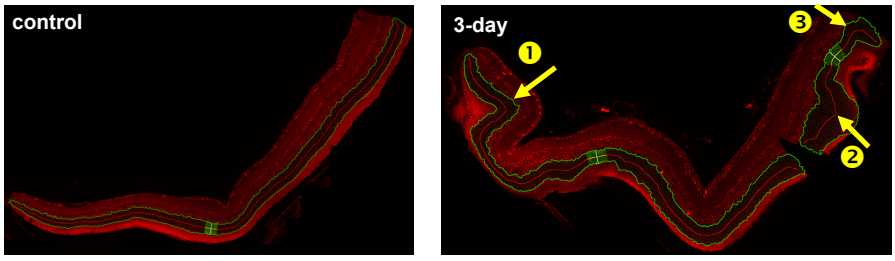

(a)

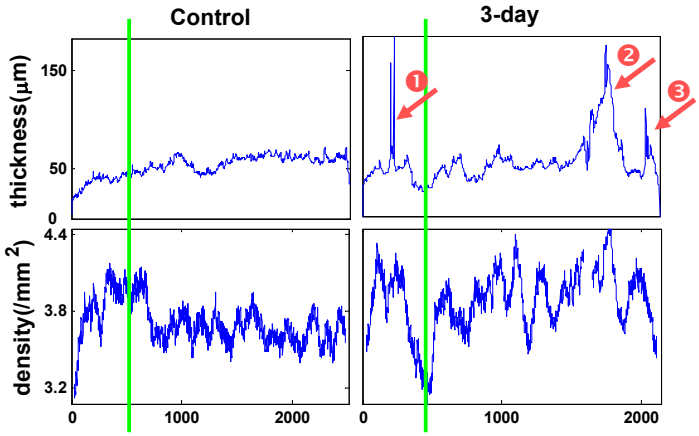

(b)

Figure 5.13: Analysis result with thickness and density profile of mouse retinas. (a) confocal images of control (Figure 5.14 (a)) and 3-day detached retina (Figure 5.14 (b)). (b) Thickness profiles (top) and density profiles (bottom).

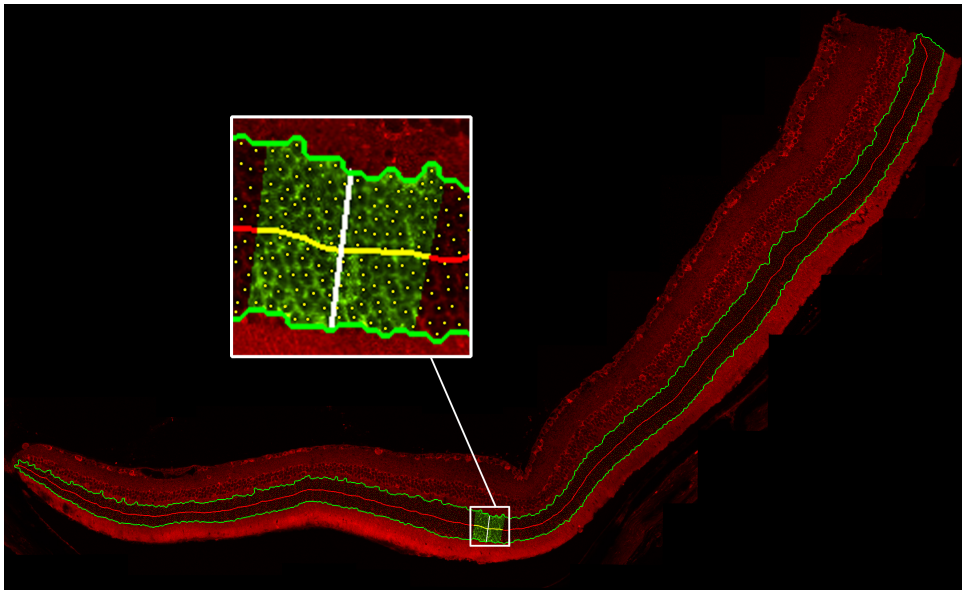

(a)

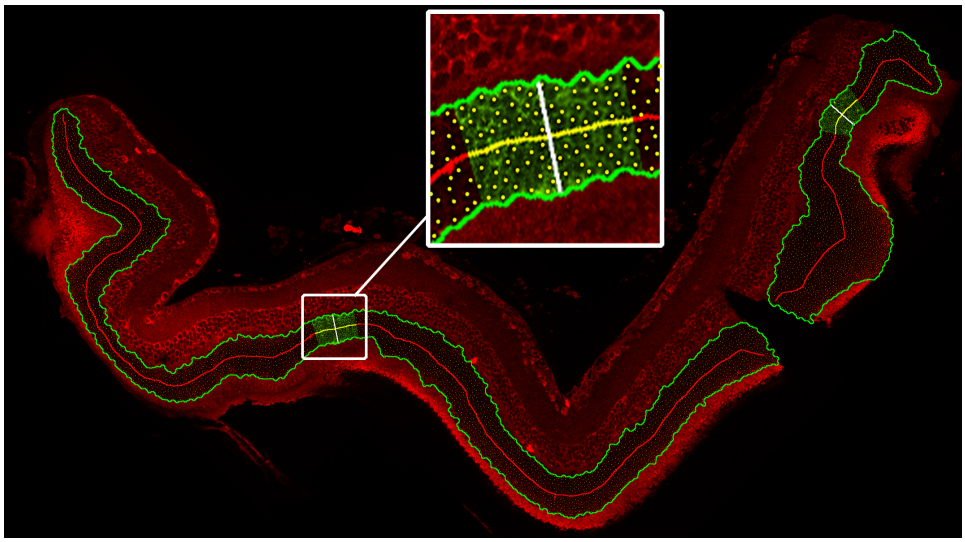

(b)

Figure 5.14: Analysis result of normal and detached mouse retinas. (a) Mosaicked 13 confocal images of a control mouse retina injected with bromodeoxyuridine (BrdU). The boundary and median curve of the ONL are displayed, and detected cell centers are marked. (b) Mosaicked 10 confocal image of a 3-day detached mouse retina.

After detachment, the profiles of thickness and density vary irregularly. Similar to the profile of a cat retina, the peaks in the thickness profile (denoted with arrows) display the locations where the retina has been folded by cellular movement, death or growth. The distortion index of the thickness profile is increased from 0.16 to 0.28 after detachment. The distortion index of the density profile also increased to 0.05 in a 3-day retina compared to 0.03 in a control retina. Significant level of distortion index of the density profile in the mouse retina is 0.04.

To compare the analysis results to those of traditional morphometric analysis, we calculate the mean and standard deviation (Figure 5.15 (a) and (b)).

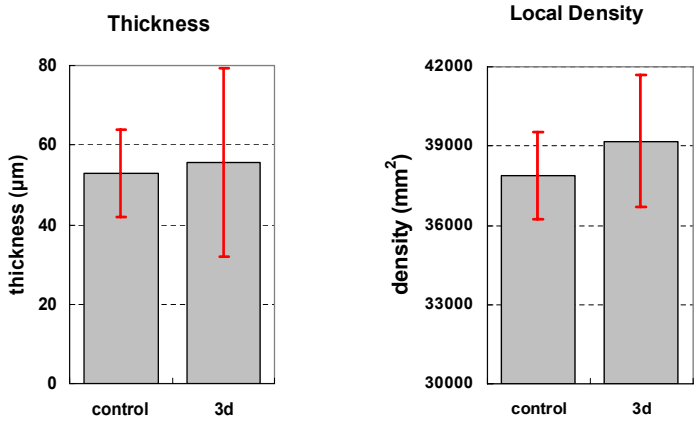

(a) (b)

Figure 5.15: Thickness of the ONL and photoreceptor cell density in mouse retinas. (a) Average thickness of control (Figure 5.14 (a)) and 3-day detached retina (Figure 5.14 (b)). The thickness of the control and detached retina are 52.94 μm (σ=11.04) and 55.66 μm (σ=23.75) respectively. (e) Average local densities of the control and detached retina are 37090.8 nuclei/mm^2 (σ=1652.58) and 38856 nuclei/mm^2 (σ=2487.53) respectively.

The control retina has 37626 nuclei/mm^2 and the detached retina has 40826 nuclei/mm^2. Both the average ONL thickness and local density are greater in the 3-day detached retina with 55.66 μm and 38856 nuclei/mm^2 (52.94 μm and

37091 nuclei/mm^2). Even though the average thickness and local cell density do not change significantly, the distortion indices of thickness indicate significant structural distortions in response to retinal detachment. The structural distortion of mouse retinas has been reported, however, it has not been able to be quantified. The distortion indices provide a new way to quantify different levels of distortions of mouse retinas which can not be captured by traditional analysis, such as cell density and thickness.

5.4 Summary

We propose fully automated method that verifies the existence of a dominant characteristic dimension (i.e. cell size or scale) in the ONL and estimates the radius of the cells that compose the layer, despite the resolution and orientation at which these images were acquired. This algorithm has been used to automatically tune the size of a filter designed to count the cells within the ONL. The performance of the proposed method compares satisfactorily both to cases where the true cell dimension is known a priori (and is used to tune the size of the filter) and to the case where the cells are counted manually. We also want to remark that the approach presented here is general and applicable to a wide variety of biological images (such as brain tissues) acquired using different imaging methods (such as transmitted light microscope). In the future, we plan to apply the proposed method to other layers (e.g. the INL) to estimate the size of multiple types of cells.

We also presented a novel method to compute multiple quantitative measures from a single set of confocal microscope images of retinas: total cell counts,

thickness and density profiles, the distortion indices of the profiles, the average thickness, and the average local density [10]. We demonstrate that the tools developed here provide a new way to interpret and characterize the structural differences of retinal tissue under different experimental conditions. The resulting quantitative measurements corroborate the cellular changes previously observed to occur following retinal detachment in both human and animal models [27]. We found that quantitative analysis based on nuclei detection not only corroborated conclusions derived from manual measurements and qualitative assessment, but also provided significant information about different levels of distortions caused by different forms of regeneration including retinal detachment. For example, we can characterize the function of intermediate filament proteins (glial fibrillary acid protein (GFAP) and vimentin) by quantifying the structural distortion of genetic mutant mice [80]. This is the first verification of earlier qualitative prediction of the functional effect of the intermediate filament proteins.

Chapter 6

Retinal Layer Segmentation

"It has been said: The whole is more than the sum of its parts. It is more correct to say that the whole is something else than the sum of its parts, because summing up is a meaningless procedure, whereas the whole-part relationship is meaningful."

Kurt Koffka

Layer segmentation and classification greatly simplifies the image analysis tasks for understanding of the events initiated by retinal detachment such as: counting photoreceptor nuclei within the outer nuclear layer (ONL), counting bipolar cells within the inner nuclear layer (INL), and measuring the axon outgrowth toward the INL. This also facilitates important analysis in localizing cells and detecting changes in protein distribution (e.g. the change in rod opsin levels in response to retinal detachment). The ONL is especially good for image segmentation since the layer has a consistent pattern; this is due to the structural similarity of cell bodies among rods and cones (Section 2.1.4). It is also important

to identify the ONL to locate all other layers since the patterns of other layers are not as consistent as that of the ONL, and are more difficult to recognize without knowledge of relationships between the retinal layers. In this way, the ONL serves as a baseline for understanding the cellular changes under a degenerative condition, and identifying the other layers. In this chapter, we propose segmentation methods which provide a reliable map of the retinal layers within an image.

6.1 Introduction

A vertical section of a retina illustrates its complexity and highly patterned architecture. Since each layer has a different structure which consists of the group of cell bodies or synaptic terminals, the intact architecture of layers is crucial to retinal function [55]. Thus, changes in the integrity of the layers serve as an index of retinal function after injury. Moreover, the information about the integrity of the layers is used for localizing specific cells and analyzing the effects of genes, drugs, stress, and protective factors on retinal integrity.

Layer segmentation and classification greatly simplifies the image analysis tasks for quantifying and characterizing the events initiated by retinal detachment including: counting photoreceptor nuclei within the ONL (Chapter 4), counting bipolar cells within the INL, and measuring the axon outgrowth toward the INL. This also facilitates important analysis in localizing cells and detecting changes in protein distribution (e.g. the change in rod opsin levels in response to retinal detachment). The ONL is especially good for image segmentation since the layer has a consistent pattern; this is due to the structural similarity of cell bodies among rods and cones (see Section 2.1.4). It is important to identify the ONL to locate

all other layers since the patterns of other layers are not as consistent as that of the ONL, and are more difficult to recognize without knowledge of relationships between the retinal layers. Additionally, the death and degeneration of photoreceptors have been considered the primary effect of detachment [53]. Identifying the ONL which consists of cell bodies of photoreceptors serves as a baseline for understanding the cellular changes under a degenerative condition.

There is no previous work of segmenting retinal layers from the images. Most of the work in biomedical image analysis has focused on the segmentation and visualization of macro biological structures such as tissues, organs and bones [62, 19, 22, 67]. On the other hand, an approach using *micro* biological structures (e.g. cellular or subcellular organism) is still in its infancy. As was pointed out in [62], the image domains of microbiological studies are diverse due to the complexity of cell functions and resulting diversity of the expressed molecules and their relationships. Segmenting a micrograph is often more challenging than segmenting medical images, since much less heuristics can be made about the signal intensities or the shape of the object [62]. These characteristics discriminate microscopic image analysis from most of classical medical image analysis that can use prior knowledge of anatomical structure to improve segmentation and visualization of macro biological structures. Thus, algorithms developed for micrograph segmentation have been very task specific.

The nature of immunofluorescent retinal images including inherited complexity of micrograph hampers applying existing segmentation methods directly (addressed in Section 2.4.1). An important assumption in segmenting regions is that the regions are generated from a stationary source. Retinal image regions,

however, are not statistically homogenous. Further difficulties in retinal images include visible variation. For example, the same layer can show a different structure depending on the antibody used, and the same antibody can be visualized as different colors. An additional consideration is that fluorescence intensity usually is not even across the tissue section, because labeled structures are not uniformly distributed within the tissue or individual cells. For example, each image from the same tissue may be collected with different laser intensity setting so a particular area of interest can be brought out in details, even though other regions of the cell or tissue are obscured in that image. Typically this means prior domain knowledge about retinal images is needed for improving segmentation. Even though the retinal images are very complex, there is a lot of high-level information, *metadata*, which is embedded in or attached to the image ranging from the pixel resolution to antibody labeling, source of a sample (e.g. animal id) and status of a sample (e.g. normal or detached). Thus, the key to solving the addressed problem is to combine such rich high-level information with low-level features extracted from image.

The main goal in this chapter is to segment retinal layers from the images to facilitate further quantitative analysis. We first segment the ONL based on a low-level feature, texture. Texture provides abundant information about the inherent visual structure in the image, in particular the ONL. Using texture analysis as a foundation, we propose a multiple layer segmentation method. We build a set of rules which maps antibody information embedded in metadata to layers within an image and use them to classify the segmented regions within an image (based on low-level features) into layers. Tile based representation of layers is useful in

categorizing images in database and narrowing search regions. In order to extract quantitative information by further analysis, we seek a segmentation methods for extracting precise boundaries of the layers. We revisit the ONL segmentation problem and propose a new method of accurately segmenting the boundary of the ONL within an image accurately.

This chapter is structured as follows. We first propse a tile-based ONL segmentation based on a texture feature (Section 6.2). We found that a low-level image feature, texture, plays an important role. The result is promising but still is limited by the heterogeneity of the retinal images. In Section 6.3, we extend the tile-based segmentation of the ONL to multiple layers (seven main layers) by associating domain specific information (layer and neighbor information) and low-level features (texture and intensity). The segmentation result demonstrates the applicability of high-level information to handle the visual variations of retinal images. In order to extract quantitative information by further analysis, the ONL segmentation problem is revisited and a new segmentation method is proposed for extracting the precise boundary of the ONL in retinal images (Section 6.4). We utilize nuclei density as a new feature to improve the pixel pairwise similarities within a framework of variational segmentation, graph partitioning active contours (GPAC). The segmentation of the ONL provides immediate benefits for quantifying cellular responses associated with retinal detachment.

6.2 Tile-based ONL Segmentation

Even though each layer has a different cellular structure, the layer boundaries are not always visible or distinguishable from each other. Some proteins are not

localized in specific layers. For example, the lectin-labeled cells with varied morphologies (green in images of Figure 6.1 (b)) are distributed throughout the layers. Moreover, after retinal detachment, the amount and the location of protein expression are shifted into different layers dramatically, and the typical stratification of these layers are no longer evident. However, the ONL has a consistent pattern regardless of antibodies used (Figure 6.1) due to the structural similarity of cell bodies among rods and cones.

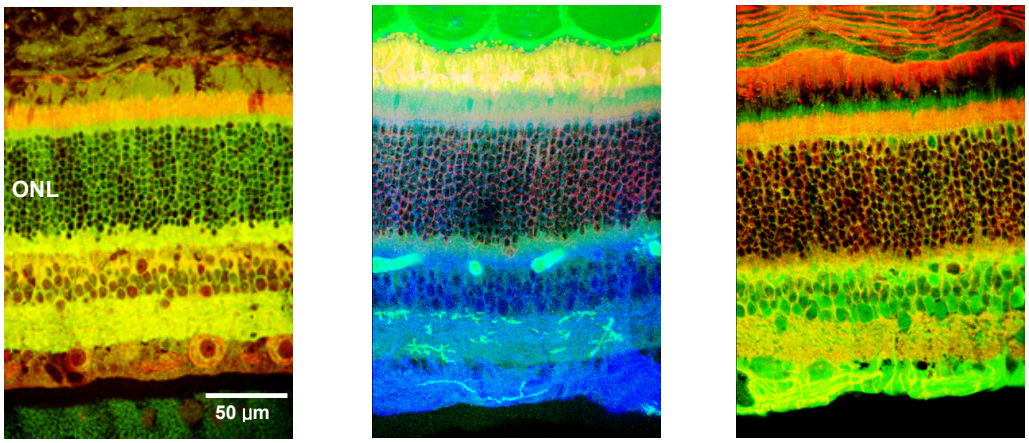

(a) (b) (c)

Figure 6.1: Histogram equalized images illustrating consistent pattern within the ONL regardless of antibodies used. (a) Double labeled image of photoreceptors (anti-cytochrome oxidase (CX); red) and pre-synaptic terminals (anti-synaptophysin; green). (b) Triple labeled image of rod photoreceptors (anti-rod opsin; red), lectin-labeled cells including microglia (isolectin B4; green), and Müller cells (anti-glial fibrillary acid protein (GFAP); blue). (c) Double labeled image of Müller cells (anti-CD44; red and anti-GFAP; green).

Identifying the ONL enables locating the other layers whose patterns are not as consistent as that of the ONL. For this reason, we focus on segmenting and annotating the ONL within retinal images. We use Gabor filters [51] to demonstrate the feasibility of the texture feature for characterizing spatial patterns within lay-

ers (Section 6.2.1). Support vector machines, a supervised learning approach, are adopted to learn the distribution of texture vectors corresponding to layers (Section 3.2). The support vector machine (SVM) trial for identifying the ONL in the normal cat retina achieved about 90% accuracy (Section 6.2.2). The classification result can serve as preliminary labels (coarse labels) for further multiple layer classification (Section 6.3).

6.2.1 Texture analysis of the ONL

Normalization

Since every image might be collected with a different magnification factor depending on the experimental conditions or the cellular structure of interest, the pixels within each image have different size with respect to their magnification (i.e. μm per pixel). The texture patterns of the ONL display in different scales, which can cause different responses of Gabor filter outputs, and in turn, mislead the classification of the ONL. To avoid this, the pixel size is normalized to the highest resolution among images, 0.228 μm per pixel, using metadata.

Since Gabor filter outputs increase monotonically with the contrast of an input image, it is often difficult to determine how closely the local image structure matches. For example, the particular level of response could indicate appropriate structure at moderate contrast or inappropriate structure at high contrast. In order to obtain more direct information about local structure not confounded with contrast, normalization with respect to the contrast is necessary [7]. The normalization is especially critical for immunofluorescent retinal images because of the intensity variation of the retinal images; the labeled structures are not

uniformly distributed within the tissue or individual cells, and each image from the same tissue may be collected with different laser intensity setting to bring out a particular area of interest. Such an intensity variation of the structure results in a great variation of the filter responses, confusing the structural differences among layers. A histogram equalization is used to normalize this intensity variation.

After preprocessing, we extract the MPEG-7 homogeneous texture descriptor (HTD) [51, 14] from every image block (64×64 pixels) in each image. We choose 64×64 pixels as a block size since we find that it is appropriate for discriminating the textures within the ONL from those in other layers based on Gabor filters. The texture descriptor for S scales and K orientations is given by

$$\mathbf{f}_{\mu,\sigma} = [\mu_I \ \sigma_I \ \mu_{0,0} \ \sigma_{0,0} \ \mu_{0,1} \ \sigma_{0,1} \ \ldots \ \mu_{S-1,K-1} \ \sigma_{S-1,K-1}]^T, \tag{6.1}$$

where μ_I and σ_I are the mean and standard deviation of the pixel intensities of the images. $\mu_{s,k}$ and $\sigma_{s,k}$ are the mean and standard deviation of the filter outputs $F_{s,k}(x, y)$. We use five scales ($S = 5$) and six orientations ($K = 6$) and eliminate μ_I and σ_I from the feature vector for the intensity invariance.

6.2.2 Experimental results

These 142 digital images of normal cat retinas were labeled with various combinations of antibodies and collected using a BioRad 1024 confocal microscope. We extract MPEG-7 HTD from each image block (64×64 pixels) in 142 images resulting in 39466 blocks. Ground truth labels are created manually for testing purposes. The SVM [38] is trained using a randomly selected half of the image blocks (19733 blocks). Since the distribution of a feature vector is complex to

separate with a linear hyperplane, polynomial (3.11) and radial basis function (RBF) (3.12) kernels are employed.

In the first experiment, we tested the performance of SVM with two types of kernels using the test set (19733 blocks) which is not used for training. The summarized results are shown in Table 6.1. In order to provide a quantitative evaluation of the results, we compute four different measures: *precision*, *recall*, *specificity*, and *accuracy*[1]. Note that the majority of data is negative (∼ONL), and here specificity and accuracy will always be high as long as the classifier is not predicting too many positives. Precision and recall suggest that the SVM is a good classifier. Both the polynomial and the RBF kernel, perform well and the difference between them is marginal as shown in Table 6.2.

Table 6.1: Summary of the ONL classification using SVM

Kernel	Results			
	TP	TN	FN	FP
Polynomial	3670	14515	1224	324
RBF	3690	14509	1204	330

TP: true positive, TN:true negative, FN: false negative, and FP: false positive.

Table 6.2: Quantitative evaluation of the classification result.

Kernel	Measures			
	Precision	Recall	Specificity	Accuracy
Polynomial	0.918	0.749	0.922	0.921
RBF	0.917	0.753	0.923	0.923

[1] Precision is the probability of positive prediction of the ONL that are correct ($\frac{TP}{TP+FP}$). Recall (sensitivity) is the probability of the both the ONL and ∼ONL that are predicted correctly ($\frac{TP}{TP+FN}$). Specificity is the probability of prediction of ∼ONL that are correct ($\frac{TN}{TN+FN}$). Accuracy is the probability of the overall prediction that are correct ($\frac{TP+FP}{TP+TN+FP+FN}$).

In the second experiment, the trained SVM is applied to identify the ONL in a given image (Figure 6.2).

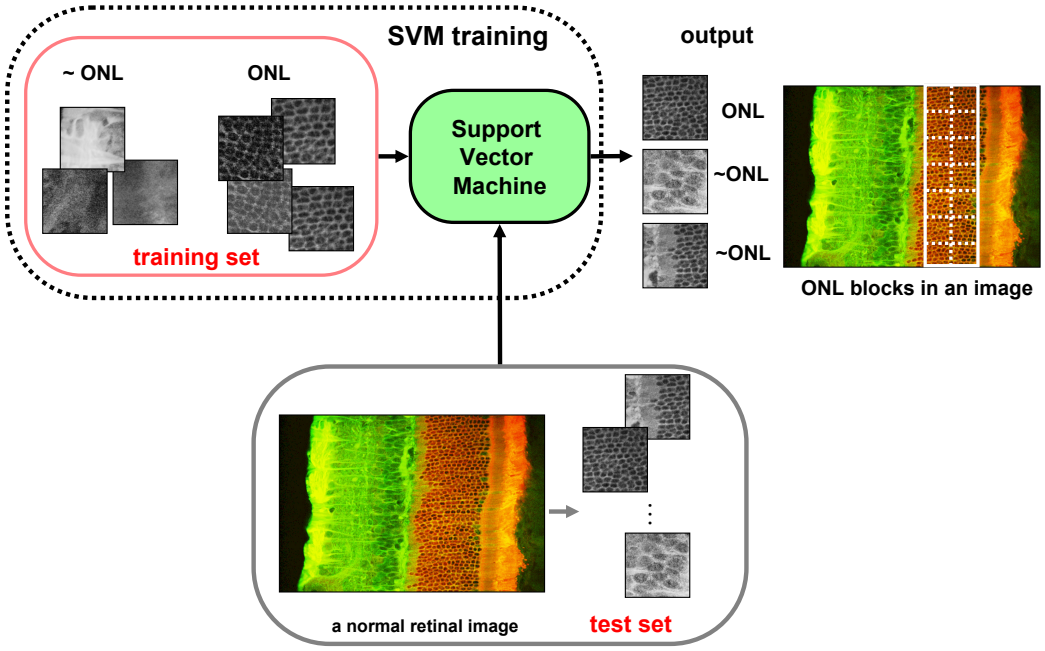

Figure 6.2: Application of the SVM to identify the ONL within a retinal image.

A given image is first divided into image blocks (64 × 64 pixels) and MPEG-7 HTD is extracted from each block. Each feature vector is fed to the SVM which classifies the ONL from other layers. After classification, all image blocks within an image are mapped to binary labels (i.e. 1 if the block is classified as the ONL and 0 if otherwise). To improve the classification results, we remove the isolated blocks that are classified as the ONL (more likely to be false positive) and correct the falsely assigned ∼ONL blocks by examining neighborhood labels. The accuracy when applying to 142 normal images is quite promising as an average of 90% ranging from 74 % to 96%.

6.3 Tile-based Multiple Layer Segmentation

In the previous section, we demonstrate that a texture feature is useful for characterizing the spatial patterns formed by the proteins, especially identifying the ONL. However the texture features alone are not enough to completely segment and classify retinal layers due to the heterogeneity of the retinal images. To automatically segment multiple layers in a retinal image, domain specific or context information is needed. We develop a novel multiple layer segmentation method by combining low-level image features (intensity and texture) with high-level (biologically meaningful) information. A schematic diagram for automatic layer classification is shown in Figure 6.3.

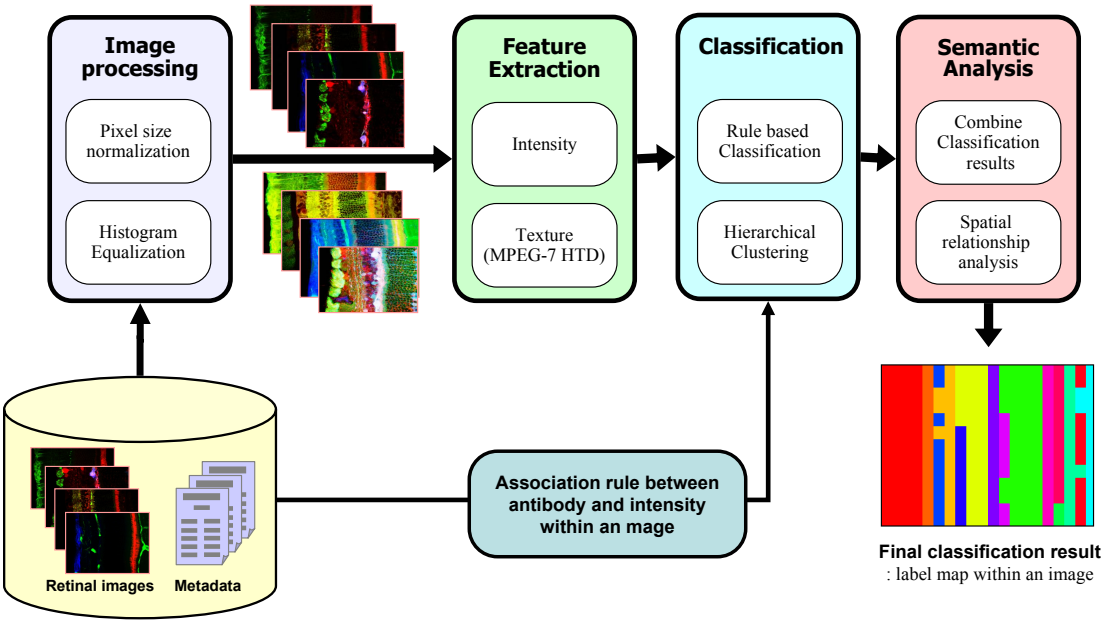

Figure 6.3: Schematic diagram of a multiple layer classification.

Using metadata associated with the images and knowledge about the relationship between antibodies and proteins, a set of rules about the structural relationships between layers and the visual appearance of layers, is generated (Section 6.3.1). For a given image, we assign a preliminary label (a coarse label) to each image block based on texture and intensity characteristics of each block (Section 6.3.2). The resulting coarse label maps are combined as a single label map of layers through a reconciliation of mutually conflicting classifications (Section 6.3.3). The final labels are refined by iterative spatial relationship analysis.

6.3.1 Rules for a retinal layer map

We focus on the images of normal cat retinas that are generated from tissue sections and labeled with various combination of antibodies. For immunofluorescent images, the specific protein in a tissue is visualized by the indirect antibody technique described in Section 2.3.3. The fluorochrome conjugated to the secondary antibody determines the color of the image. That is, the tissue stained with the antibody is collected as a pseudo colored image. In this image, high intensity corresponds to high concentration of the specific protein expression and the rest of an image appears as dark regions (Figure 6.4 (b)). Thus relatively higher intensity within the image determines the subset of layers where the proteins are localized. For example, the high intensity region in the red channel of Figure 6.4 (b) shows the high concentration of rod opsin expression that are localized in the outer segments (OS) of rod photoreceptors. When the tissue is stained with multiple antibodies, the response to each antibody is combined to form a color image where the color represents to the protein response to each antibody.

Since the proteins are concentrated in different types of cells depending on their functions, the different proteins are usually localized in different layers. Hence the color is a useful feature to discriminate each layer.

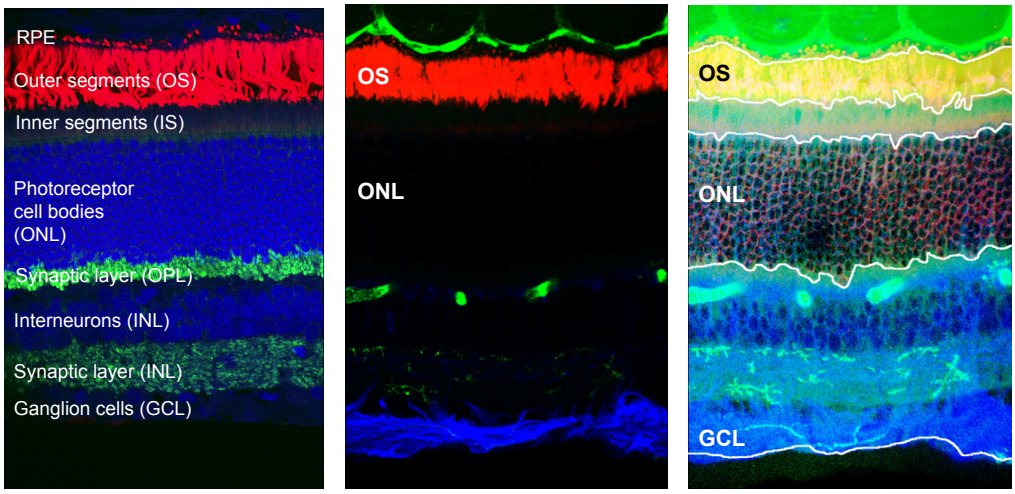

(a) (b) (c)

Figure 6.4: Example retinal image. (a) Confocal microscopy of a vertical section through a cat retina. (b) Triple labeled image of rod photoreceptors (anti-rod opsin; red), lectin-labeled cells including microglia (isolectin B4; green), and Müller cells (anti-GFAP; blue). (c) Histogram equalized image of (b). The boundaries of the layers are manually created and overlaid in white.

As shown in Figure 6.4 (a), a retinal image can be divided into seven main layers, ganglion cell layer (GCL), inner plexiform layer (IPL), inner nuclear layer (INL), outer plexiform layer (OPL), outer nuclear layer (ONL), inner segments (IS) layer, and OS layer. We define nine basic regions and the extra eight regions which are derived from two neighboring regions of the basic nine regions (Table 6.3).

Table 6.3: Coarse feature label for retinal layers.

Label	Meaning
BG	Background
GCL	ganglion cell layer
IPL	inner plexiform layer
INL	inner nuclear layer
OPL	outer plexiform layer
ONL	outer nuclear layer
IS	inner segment layer
OS	outer segment layer
RPE	retinal pigment epithelium
BG-GC	boundary between BG and GCL
GC-IP	boundary between GCL and IPL
IP-IN	boundary between IPL and INL
IN-OP	boundary between INL and OPL
OP-ON	boundary between OPL and ONL
ON-IS	boundary between ONL and IS
IS-OS	boundary between IS and OS
OS-RP	boundary between OS and RPE

A set of rules which maps antibody information in metadata to layers within an image is generated manually (Table 6.4). These rules determine the subset of layers presented with relatively higher intensity within the image. Characterizing the spatial patterns formed by these rules will induce another rule or clue for neighboring layers. These rules are used for coarse label assignments to each image block based on its intensity. Furthermore, new sets of rules such as the relationship between antibodies and clustered textures can be induced based on these rules by using association rule mining techniques. Note that these rules are specialized for the images of normal cat retinas.

Table 6.4: The rules between antibodies and retinal layers

	Rules (e.g. if (antibody = a_1) then (visible layer = l_1))
1	calretinin → GCL, INL
2	calbindin → INL
3	neurofilament → GCL, IPL, INL
4	synaptophysin → IPL, OPL
5	GFAP → GCL
6	vimentin → GCL
7	CD44 → IS
8	cytochrome oxidase (CX) → IS, OS
9	peanut agglutinin (PNA) → OS
10	alpha36H → OS
11	rod opsin → OS
12	ML-cone opsin → OS
13	S-cone opsin → OS
14	carbonic anhydrase II (CA) → GCL, IPL, INL, OPL, ONL, IS, OS
15	cellular retinaldehyde binding protein (CR) → GCL, IPL, INL, OPL, ONL cellular retinaldehyde binding protein (CR) → IS, OS
16	glutamine synthetase (GS) → GCL, IPL, INL, OPL, ONL, IS, OS

6.3.2 Segmentation based on low-level features

In the first step, image processing, pixel size is normalized to 0.228 μm and the histogram-equalized image of each image is generated as described in Section 6.2.1. There are two independent sets of feature classification results based on the texture and color (intensity). An input image is first partitioned into a 64×64 blocks and coarse layer labels are assigned using color characteristics and a set of rules shown in Table 6.4. The histogram equalized image is used for texture based clustering.

Rules based classification

Each channel image is converted to a binary image using a global threshold value computed by Otsu's method, which chooses the threshold to minimize the intraclass variance of the black and white pixels [65]. The output value of each block is determined by the proportion of *on*-pixels within a block as follows:

$$L_m(x,y) = \begin{cases} 1 & \text{if } p_m(x,y) > 0.5 \\ 0 & \text{otherwise} \end{cases} \tag{6.2}$$

where $L_m(x,y)$ is (x,y) blocks in the output label image L_m, m is the channel (for Figure 6.5, $m = 2$), and $p_m(x,y)$ is the ratio of the number of *on*-pixels to total number of pixels within a block. A set of rules (Table 6.4) is applied to each label image L_m using metadata associated with the image. Multiple label images are combined into a single label map $L_r(x,y)$. If there is conflict among multiple label images, the label is determined by the block whose $p_m(x,y)$ is maximum:

$$L_r(x,y) = L_m(x,y), m = \underset{m}{\operatorname{argmax}}\ p_m(x,y). \tag{6.3}$$

The example label map $L_r(x,y)$ is shown in Figure 6.5. The blocks without labels are defined as an unlabeled block. These unlabeled blocks can be assigned by the label map generated by texture based clustering, and the iterative spatial relationship analysis presented in Section 6.3.3.

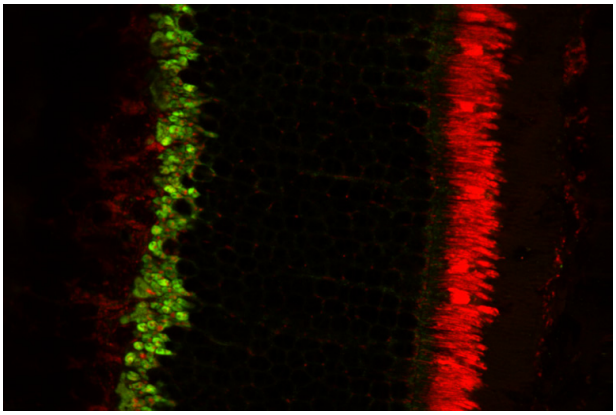

(a)

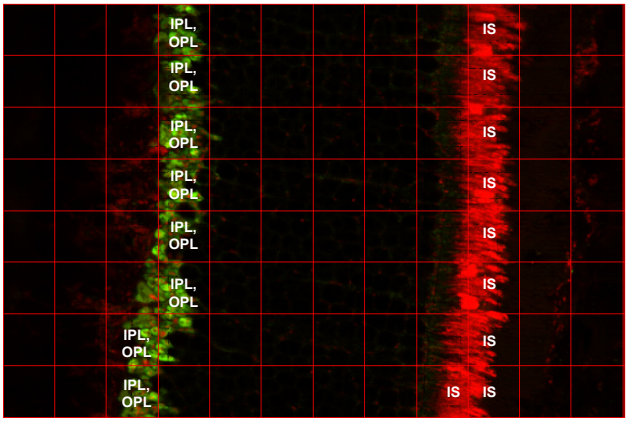

(b)

Figure 6.5: Result of coarse label assignment to each image block within an image based on the rule between antibodies and corresponding layers. (a) An example of double labeled image with antibody to cytochrome oxidase (CX) (red) and antibody to synaptophysin (green). (b) Localization of protein gives a layer information. Labels are assigned by using rule 4 and 11 in Table 6.4.

Clustering of texture features

We extract the MPEG-7 HTD from every image block (64×64 pixels) in each image. Since textures from other layers are not as consistent as that of the ONL, a SVM is not suited for multiple layer segmentation. While the same layer, from the same or different tissues and from different antibody staining, often illustrates highly varied textures *across* the images, texture is still useful for characterizing each layer *within* an image. We cluster the extracted texture descriptors using a hierarchical clustering instead of using a SVM (Figure 6.6). Figure 6.6 (a) shows an example retinal image stained with antibody to cytochrome oxidase (CX). The cluster is constructed from a hierarchical tree which is constructed using a distance between each pair of feature vectors (Figure 6.6 (b)). Figure 6.6 (c) shows the dendrogram used for obtaining clusters shown in Figure 6.6 (b). A constant threshold value is used for all images in the data set. All nodes below the threshold value are grouped into a cluster which is displayed with a unique color in the tree. For example, a group of nodes in the leftmost of tree (green in Figure 6.6 (c)) is grouped as *cluster 5* which corresponds to the ONL in Figure 6.6 (b). Different partitioning of features can be obtained by cutting the consensus tree at different heights (lower height yields more clusters). Note that the cluster that includes the most images blocks and the smallest distance among features within a cluster is the ONL. If an image consists of more than one channel, resulting cluster maps from multiple channels are combined to a single cluster map, $L_t(x, y)$. The cluster maps obtained from different channels may conflict with each other. To reconcile mutually conflicting results, the output label of conflicted block is assigned by the clustering result with a minimum distance within a cluster.

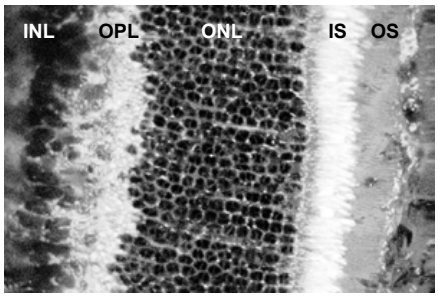

(a)

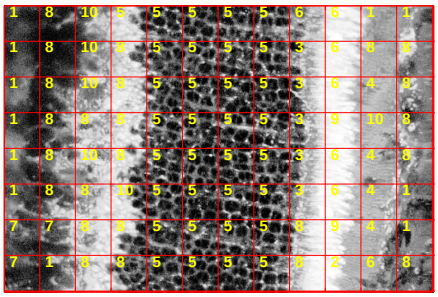

(b)

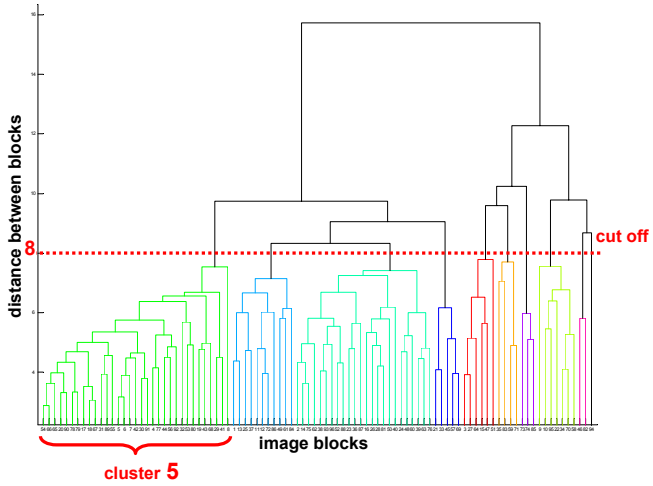

(c)

Figure 6.6: Example of hierarchical clustering result. (a) An example of a normal image labeled with antibody to CX. (b) Clustering result by hierarchical clustering. The number on the image block denotes the cluster id. (c) A distance tree (dendrogram) constructed using texture features. X and Y axis denote each image block (96 blocks in this example) and the distance between two image blocks respectively. The height of edges connecting two image blocks represents the distance between them in the feature space. The each group of nodes (image block) within the dendrogram whose linkage is less than threshold value is displayed in a different color.

6.3.3 Semantic analysis of layer labels

The initial result based on texture and color is two coarse label maps: the label map, $L_r(x, y)$, from rules based classification, and the label map, $L_t(x, y)$ from texture based clustering. The parallel results from different features can provide cues for semantic analysis to find potentially erroneous detections as well as missing labels. First, the label maps from color and textures are combined iteratively. Suppose we apply an algorithm such as Algorithm 1. The label map $L_r(x, y)$ generated using color and rules is comprised of the labeled (e.g. IS and IPL, OPL in Figure 6.5) and unlabeled blocks. The label map based on texture consists of the number of clustered blocks (e.g. 1, ..., 10 in Figure 6.6 (b)). Since a majority of blocks in $L_r(x, y)$ are usually unknown, the combined label map $L(x, y)$ is initialized based on texture based label map, $L_t(x, y)$. The blocks in $L(x, y)$ which have valid layer labels in $L_r(x, y)$ are first analyzed. If the clustered region from both maps coincide, the layer labels in $L_c(x, y)$ are assigned to the blocks in $L(x, y)$. Otherwise, the labels are assigned based on the confidence of the applied rules. Figure 6.7 shows the combined label map using Algorithm 1.

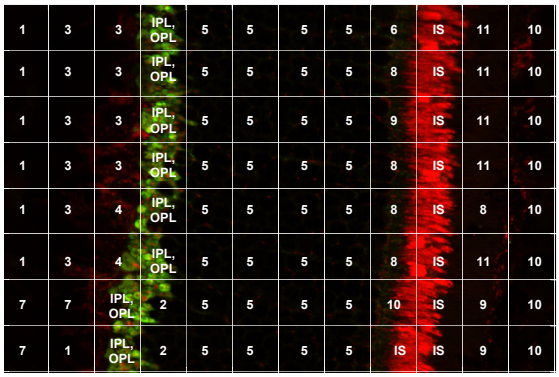

Figure 6.7: The combined label map.

Algorithm 6.1: Combining two label maps.

Input: two label maps based on color, $L_r(x, y)$ and based texture $L_t(x, y)$

Output: a combined label map $L(x, y)$

initialization;

$L(x, y) = L_t(x, y)$;

while *there is a conflict label between* $L_r(x, y)$ *and* $L_t(x, y)$ **do**

  for $k = 1$ *to* K **do** /* K: the number of labels $\in C_c$ of $L_r(x, y)$ */

    for $L_r(x, y) \in C_c(k)$ **do**

      $cid = L(x, y)$;

      find all blocks $L(x, y) \in \mathbf{C}(cid)$;

      if $L(x, y) \in C_c(k) \cap \mathbf{C}(cid)$ **then** /* both maps are agreed */

        $L(x, y) = L_c(x, y)$;

      else/* both maps are conflicted */

        if *a rule* $\in \{R_1, \ldots, R_{13}\}$ **then** /* a rule is confident */

          $L(x, y) = L_c(x, y)$;

        else

          $L(x, y) = L_t(x, y)$;

        end

      end

    end

  end

end

The combined map is refined using the domain knowledge–the spatial relationship between layers. This is an iterative process where the clustered image blocks interact with, support, or oppose each other, and finally come up with a more coherent and consistent label map. Figure 6.8 shows some of the intermediate steps.

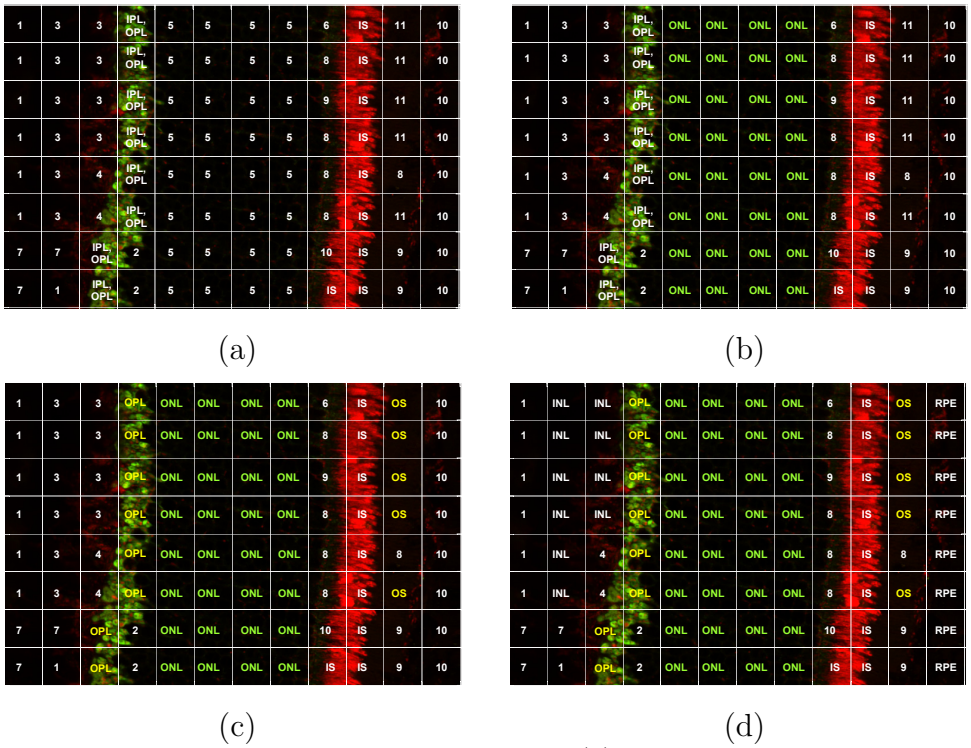

Figure 6.8: Refining the combined label map. (a) The combined map in Figure 6.7. (b) The largest cluster 5 is assigned to the ONL (denoted in green). (c) The second iteration, the label IPL, OPL is corrected as OPL using neighborhood information, and OS is assigned. (d) INL and RPE are assigned subsequently.

6.3.4 Experiment Results

We present the results of applying the proposed method to confocal images of retina. 142 digital images of normal cat feline retina are generated from tissue sections labeled with different combinations of 17 antibodies using a BioRad 1024

confocal microscope. Layer labels and a set of rules are generated manually using metadata and knowledge about the spatial relationship between protein and retinal layers (Table 6.3 and Table 6.4). Three types of features are used for the classification: intensity from a normalized images, texture features from normalized and histogram-equalized images, and spatial relationships among adjacent layers. The label of each block is assigned by combining the result of texture-based clustering and rule-based classification, and then spatial relationships between neighboring layers are applied to refine or correct falsely labeled blocks. The final label of each block in the image is compared to manually assigned labels of layers for each image block. 76% accuracy over 21475 tiles within 142 normal images is achieved. Figure 6.9 shows the final label map of Figure 6.5.

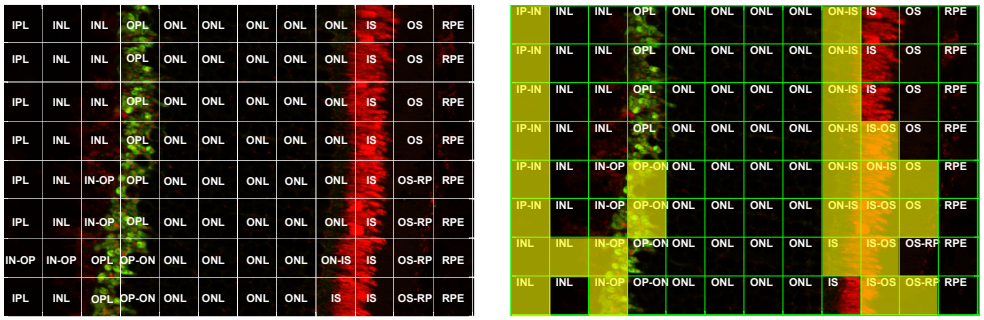

(a) (b)

Figure 6.9: Example final label map of Figure 6.5 (a). The final label map (a) and its ground truth (b). Yellow blocks overlaid on the ground truth illustrate the difference between the final map and its ground truth, suggesting most of errors are occurred in the boundaries of layers.

The yellow blocks overlaid on the ground truth (Figure 6.9 (b)) illustrate the error between the final map and its manual labeling. Most of the errors are caused by a block which contains a boundary between two layers, which can be interpreted as a typical problem of a tile-based approach. To improve the clas-

sification accuracy, a precise segmentation method needs to be developed rather than a tile based approach.

6.4 Pixel level ONL Segmentation

The main goal of the segmentation is to facilitate image analysis for understanding of the events initiated by retinal detachment. Therefore, it is important to extract the precise boundary of the layer, especially the ONL, to extract quantitative information by further analysis. Toward this motive, we propose a new method for segmenting the boundary of the ONL in retinal images. We employ GPAC to segment the ONL from the retinal images because of the versatility of GPAC; the information about pixels can be easily embedded in the similarity metric and it provides a robust result in spite of topology changes. To cope with the heterogeneity of retinal images, we exploit the nuclei density calculated using candidate nuclei positions (proposed in Chapter 4) as high-level information to improve the segmentation accuracy. In the following section, we introduce three similarity metrics used for segmenting the ONL.

6.4.1 Dissimilarities in the feature space

For the retinal images, we calculate three dissimilarities between pixels: color, texture, and nuclei density. These dissimilarities are calculated from histogram equalized images. We begin with dissimilarities using color, and add texture and nuclei density into the dissimilarity metric demonstrating the improvement of the segmentation.

Dissimilarities in color space

The dissimilarities using color features are evaluated as follows:

$$w_{col}(p_1, p_2) = \sqrt{\sum_{i=1}^{3} \Big(c_i(p_1) - c_i(p_2) \Big)^2} \tag{6.4}$$

where c_i represents each one of the color channels in the CIELab color space. Figure 6.10 shows the segmentation result of a retinal image. The results are greatly varied depending on the intensity of antibody labeling. While the ONL is perfectly identified and segmented (Figure 6.10 (b)), some of layers are confused together with the ONL (Figure 6.10 (d)).

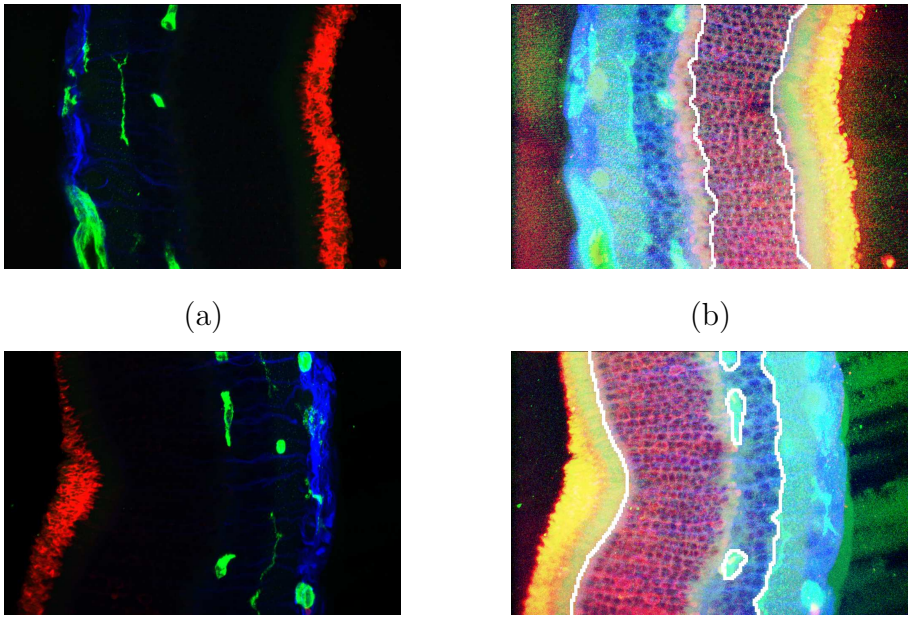

(a) (b)

(c) (d)

Figure 6.10: Segmentation of retinal images using color feature. The images are triple labeled with isolectin B4 (green), and antibodies to rod opsin (red), and GFAP (blue). (a) An example of a 1-day detached retina. (b) An histogram equalized image of (a) with detected boundaries. (c) An example of a 1-day detached retina.(d) An histogram equalized image of (c) with detected boundaries. Three layers (INL, OPL, and ONL) are segmented as the ONL.

Dissimilarities in color and texture space

As was shown in Section 6.2, the texture feature plays on important role in segmenting and classifying the ONL. Texture features are calculated using Gabor filters and the specifications of the Gabor filter bank used for extracting texture features are $S = 5$, $K = 6$, $U_l = 0.05$, and $U_h = 0.25$ [51]. For every pixel in the original image, a 30 dimensional feature vector is therefore generated and distances are evaluated in this 30 dimensional feature space:

$$w_{tex}(p_1, p_2) = \sqrt{\sum_{i=1}^{30} \Big(t_i(p_1) - t_i(p_2) \Big)^2}, \tag{6.5}$$

where t_i represents one of the output of the Gabor filters. The color and the texture features are combined with appropriate weights as follows:

$$w_{Tot}(p_1, p_2) = \alpha \; w_{col}(p_1, p_2) + \beta \; w_{tex}(p_1, p_2), \tag{6.6}$$

where α and β are two constants such that $\alpha + \beta = 1$. The segmentation result is improved by adding texture feature as shown in Figure 6.11. When the texture feature is combined with color, the segmentation result is greatly improved in the region which appears in similar color but consists of multiple patterns. For example, Figure 6.11 (c) shows that five retinal layers (left side of the boundary) are merged and segmented as a foreground (i.e. the ONL) using color. The texture feature helps to discriminate the ONL from other four layers resulting refined boundaries around the ONL.

Dissimilarities in color, texture, and nuclei density

Even though the segmentation result is improved by adding texture feature, there still remains the limitation of low-level features. The amount and the lo-

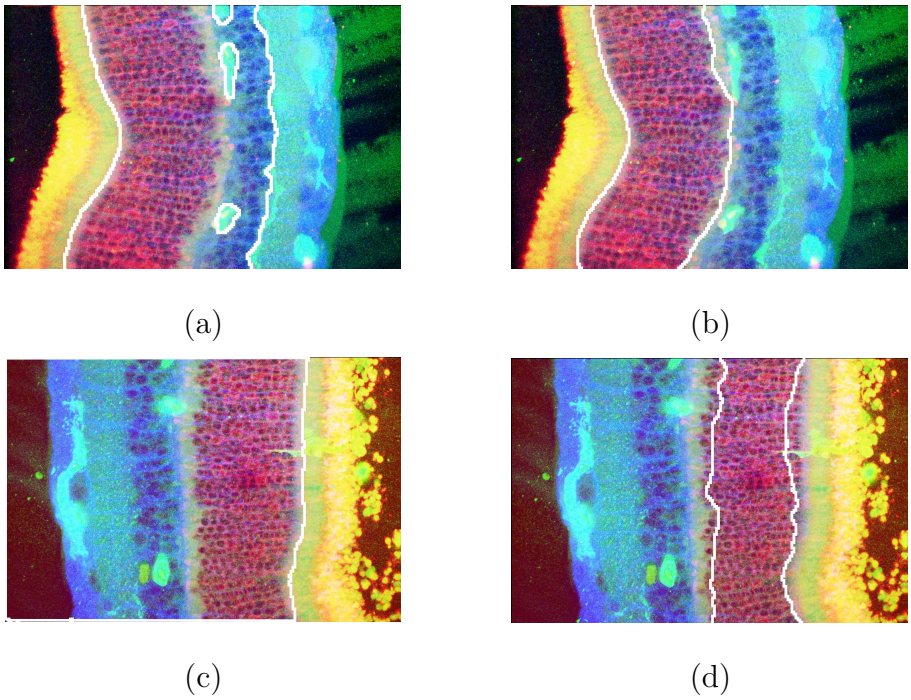

(a) (b)

(c) (d)

Figure 6.11: Segmentation of retinal images using color and texture. The images are triple labeled with isolectin B4 (green), and and antibodies to rod opsin (red), and GFAP (blue). (a) The segmented result using only color ($\alpha = 1$ and $\beta = 0$). The detected boundaries are overlaid on the image. (b) The segmented result of the same image (a) using color and texture ($\alpha = 0.5$ and $\beta = 0.5$). (c) The segmented result using only color ($\alpha = 1$ and $\beta = 0$). The left side of the boundary is segmented as the ONL. (d) The segmented result of the same image (c) using color and texture ($\alpha = 0.5$ and $\beta = 0.5$). The boundaries of the ONL are refined.

cation of protein expression are shifted dramatically after detachment, and the typical stratification of these layers are no longer evident. Multiple layers are often confused as the ONL since the layer boundaries are not always visible or distinguishable from each other. To obtain a robust segmentation result, we exploit high-level information of the ONL which is independent of the antibodies used. Considering that the ONL is the layer which consists of the cell bodies of the photoreceptors, we utilize the nuclei density as a high-level information. Nuclei

density is calculated from the candidate nuclei positions, given by the output of the nucleus detector (Chapter 4). The nucleus detector is designed for detecting photoreceptor cell bodies. As shown in Figure 6.12 (a), the candidate nuclei are accurately detected within the ONL and also detected outside of the ONL since no information about the boundaries of the ONL is provided. The detected nuclei outside of the ONL is not as dense as those within the ONL, therefore the density information can be used to discriminate the ONL from others.

For each candidate nucleus position, the nuclei density is calculated as follows:

$$n(p_i) = \max h(q), \;\; q \in [0, \ldots, 7], \tag{6.7}$$

where $h(q)$ is the histogram of candidate nuclei within the circle around each position of candidate nucleus. Choosing maximum value among eight bins enables us to obtain high values for the candidates belonging to the ONL which are located near the boundaries. The resulting image has a higher output value around the ONL and very low value in the rest of images (Figure 6.12 (b)).

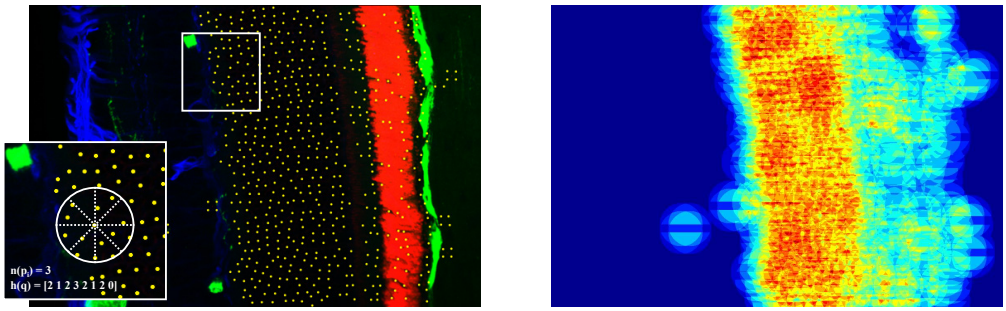

(a) (b)

Figure 6.12: Calculating a nuclei density feature. (a) Candidate nuclei positions (marked as yellow dots). A proportion of (a) boxed is displayed in higher magnification and the circle to compute the histogram of candidate nuclei is overlaid. For the candidate nucleus p_i on the center of the circle, $n(p_i) = \max h(q) = \max$ [2 1 2 3 2 1 2 0]. (b) The computed nuclei density.

The distances using nuclei density are evaluated as follows:

$$w_{nd}(p_1, p_2) = \sqrt{\sum \Big(n(p_1) - n(p_2 \Big)^2}. \tag{6.8}$$

The similarity matrices of Figure 6.14 computed from three features are shown in Figure 6.13. For computational efficiency, a similarity between a block and a pixel is computed for each pixel within an image. The Y axis denotes the number of pixels within an image (i.e. NM where N and M is the width and the height of an image) and the X axis represents the number of blocks (i.e. $\frac{NM}{B}$ where B is a block size). The similarity matrix computed from nuclei density illustrates that the nuclei density is effective to identify the similarity between the pixels corresponds to the ONL.

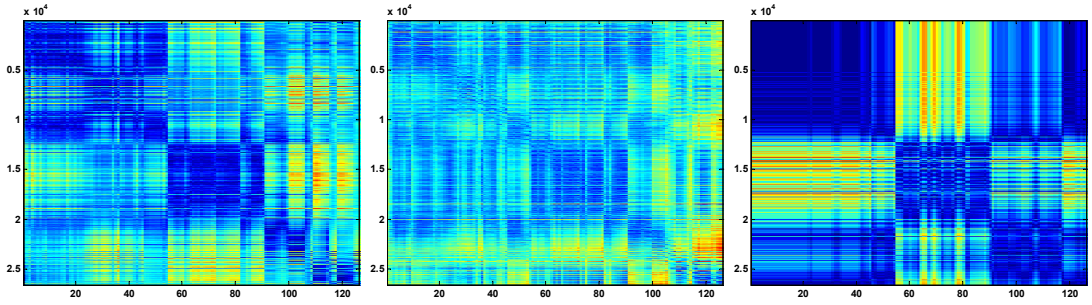

(a) (b) (c)

Figure 6.13: Similarity matrix representations. X and Y axes denote the number of blocks and the number of pixels within an image. (a) Similarity matrix computed from color using (6.4). (b) Similarity matrix computed from texture using (6.5). (c) Similarity matrix computed from nuclei density using (6.8).

The nuclei density is combined with the other features as

$$w(p_1, p_2) = \alpha \; w_{col}(p_1, p_2) + \beta \; w_{tex}(p_1, p_2) + \gamma \; w_{nd}(p_1, p_2), \tag{6.9}$$

where α, β, and γ are constants such that $\alpha + \beta + \gamma = 1$. The segmentation result is improved by adding nuclei density information. Figure 6.14 (a) shows

the segmentation result using color and texture illustrating the limitation of low-level features. Since the texture within the ONL and INL are similar, both the ONL and the INL are segmented as a foreground, the ONL. The nuclei density, however, within the ONL is greatly higher than that of the INL. The INL is easily excluded from the segmentation result as shown in Figure 6.14 (b).

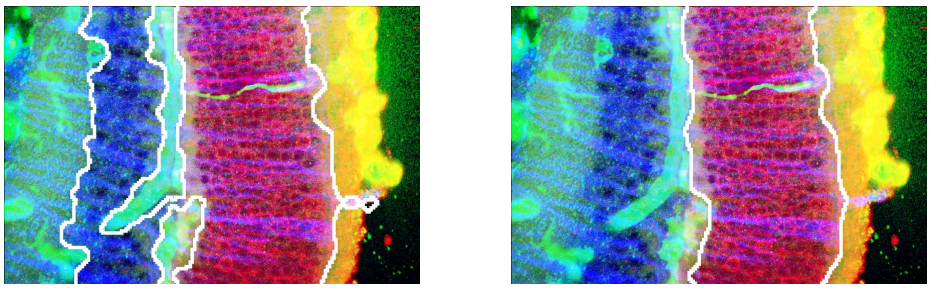

(a) (b)

Figure 6.14: Comparison of segmentation results by using different features. The image is triple labeled with isolectin B4 (green), and antibodies to rod opsin (red) and GFAP (blue). (a) The segmented result by using color and texture ($\alpha = 0.5$ and $\beta = 0.5$). (b) The segmented result by using color, texture, and nuclei density ($\alpha = 0.2$, $\beta = 0.2$, and $\gamma = 0.6$).

6.4.2 Experimental results

We present the result of applying the proposed method to a series of confocal images. 50 images of cat retina were generated from tissue sections under four different experimental conditions: 10, 14, 14, and 12 images from normal, 1-day, 3-day, and 7-day detached retinas. Images were labeled with isolectin B4 (green) and with antibodies to rod opsin (red) and GFAP (blue). The ground truth data, consisting of the boundaries for the ONL, is created manually. The dissimilarity measure $w(p_1, p_2)$ is computed as linear combination of color, texture, and nuclei density information as shown in equation (6.9). When only the color and texture

are used for segmentation, the best results are obtained by using the equal weight for them (i.e. $\alpha = \beta = 0.5$). Therefore, we vary only γ, and use an equal weight for color and texture, thus equation (6.9) is rewritten as follows:

$$w(p_1, p_2) = \alpha\ w_{col}(p_1, p_2) + \alpha\ w_{tex}(p_1, p_2) + \gamma\ w_{nd}(p_1, p_2). \tag{6.10}$$

The curve evolution for equation (3.17) has been implemented using a semi-implicit finite difference scheme with the curvature coefficient $\mu = 2000$ for all the experiments. Figure 6.15 shows the visual segmentation results of images under four different conditions ($\alpha = 0.2$, $\beta = 0.2$, and $\gamma = 0.6$).

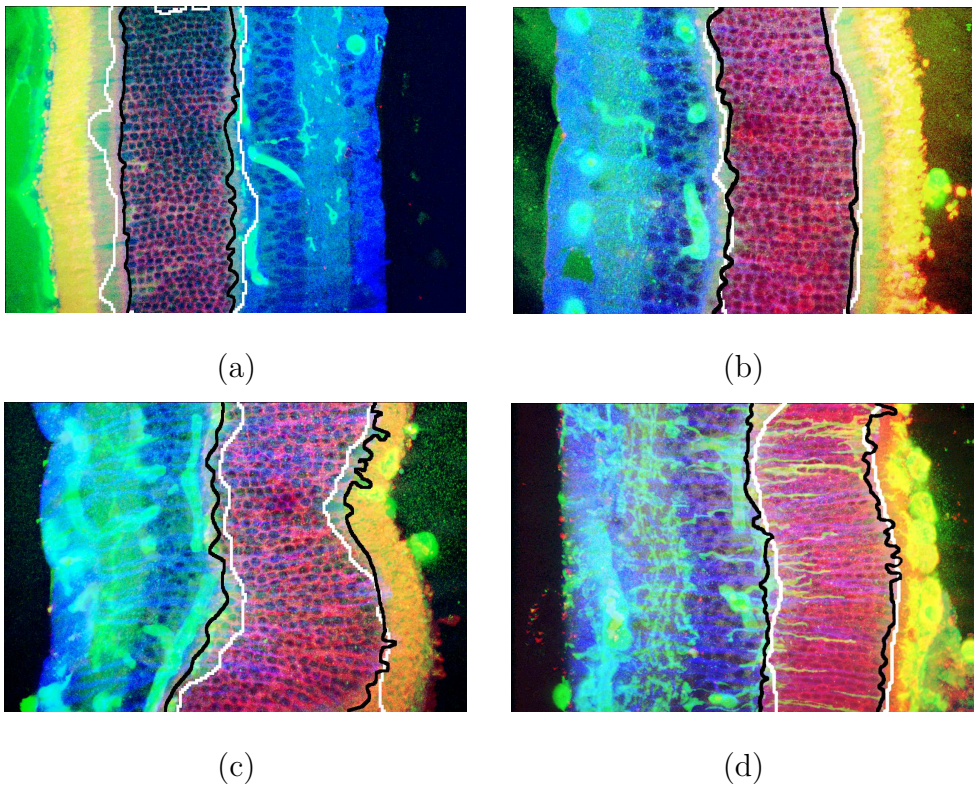

(a) (b)

(c) (d)

Figure 6.15: The segmentation result using color, texture, and nuclei density ($\alpha = 0.2$, $\beta = 0.2$, and $\gamma = 0.6$). The white boundaries are detected by the proposed algorithm and black ones are ground truth. (a) Normal. (b) 1 day after detachment. (c) 3 days after detachment. (d) 7 days after detachment.

The detected ONL boundaries are depicted in white and the ground truth in black. The ONL from the images under different conditions are segmented well despite of the variations in color and textures. The nuclei density increase the ability to capture the similarity between pixels within the ONL by enhancing the difference between pixels within the ONL and pixels within the other layers.

In order to provide a quantitative evaluation of the results, we compared them with the ground truth, computing *precision* (p) and *recall* (r) as measures of the accuracy of the segmentation[2]. In Figure 6.16, we present the F *measure*, the harmonic mean of precision and recall ($F = \frac{2pr}{p+r}$), varying the parameter γ (weight of nuclei density feature). The best score $F = 0.831$ is obtained for $\gamma = 0.6$, which means more weight for nuclei density and equal weight for color and texture as $\alpha = \beta = 0.2$.

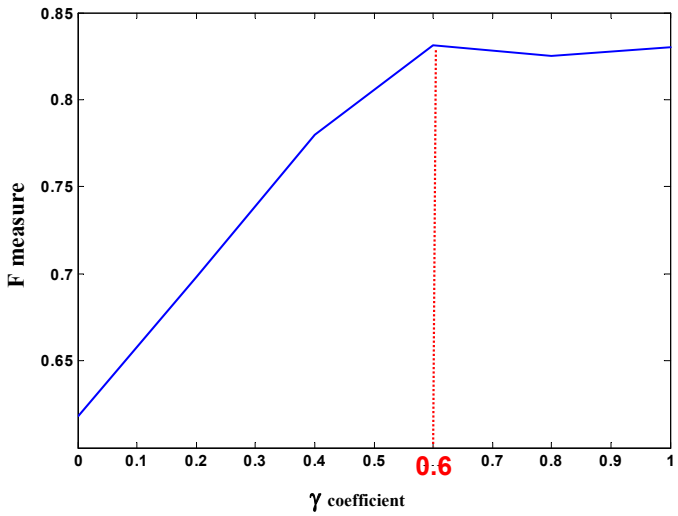

Figure 6.16: Quantitative evaluation of the results. F measure varying the parameter γ for the segmentation of the 50 images.

[2]Precision is the probability that a pixel, indicated as belonging to the ONL by the segmentation algorithm, is truly on ONL pixel. Recall is the probability that an ONL pixel is correctly detected by the algorithm.

We find that the performance does not degrade significantly by using a higher weight for nuclei density ($F = 0.825$ for $\gamma = 0.8$ and $F = 0.830$ for $\gamma = 1$), since the color and texture information is embedded while computing the candidate nuclei positions.

6.5 Summary

We described methods for segmenting and classifying the retinal layers which are able to manage the inherent complexity of retinal images due to the heterogeneity in regions/layers.

We proposed a tile-based ONL segmentation method based on texture, HTD. The SVM trial for identifying the ONL in the normal cat retina achieved promising result as an average of 92% accuracy. Additionally, the ONL segmentation was extended to multiple layer segmentation. The main idea is to combine low-level image features (color and texture) with high-level information (the relationship between antibodies used and retinal layers). A set of rules which maps an antibody used to visual appearance of layers within an image, was explored. For a given image, two coarse label maps were assigned based on color and texture. The resulting coarse label maps were combined as a single label map and refined by iterative spatial relationship analysis. The result of applying the proposed method to 142 images of normal cat retinas was an average accuracy of 76%. Most errors occurred in the block which contains a boundary between two layers, which is a typical problem of a tile-based approach. The segmentation results can be used as a basic semantic element in retinal image representation to locate cells of interest and to determine changes in protein distribution. We also find the segmentation

results useful for building a searchable database by image content [11].

Finally, we presented a method to accurately segment the boundary of the ONL in retinal images in the variational segmentation framework. We exploit the nuclei density calculated using candidate nuclei positions (proposed in Chapter 4) as a high-level information to handle the heterogeneity of the retinal images. The segmentation accuracy is greatly improved by using our nuclei density feature. The segmentation result is also useful for automating further analysis such as counting photoreceptor nuclei within the ONL and characterizing the structural distortions of the layers described in Section 5.3.

Chapter 7

Modeling The Retinal Detachment Process

"All models are wrong, but some models are useful."

Jitendra Malik

Retinal detachment continues to be a significant cause of visual impairment. There are surgical procedures that physically reattach the retina, however, the visual outcome is unpredictable in spite of the high rate of surgical success. For that reason, understanding the effects of detachment (and reattachment) become even more important. Confocal microscopy can yield insight into the nature of the cellular processes of a retina that have been disrupted by retinal detachment, and can provide information about the changes in cell morphology and the expression patterns of specific proteins associated with retinal detachment. Characterizing these changes may help us to understand the cellular mechanisms initiated by retinal detachment, and ultimately facilitate the discovery of therapeutic agents that may reduce the damaging effects of detachment or improve the outcome of

reattachment surgery. Quantitative measurements of the retina (e.g. photoreceptor cell density and thickness of the outer nuclear layer (ONL)) provide the basis of an understanding of biological changes to retinal detachment, however, they are not sufficient to explain the involvement of a cell's multiple constituents or multiple proteins in complex cellular mechanisms. This in turn requires quantitative modeling for learning the underlying relationships, to explain both relatively simple modules of molecular machinery of the cell, and to achieve system-level understanding of retinopathy (disease of retina) induced by detachment.

The primary objective is to model the retinal detachment process in order to understand the protein-protein interactions within the retinal cells as well as interactions between cells. The Bayesian network framework is ideally suited to study this problem. A Bayesian network is constructed with quantitative features derived from retinal images under different experimental conditions. The constructed network predicts causal influences of experimental conditions on thickness, cell density, and protein expression levels, which are traditionally reported relationships. The network also predicts interactions between proteins that have not been reported: a relationship among rod opsin, glial fibrillary acid protein (GFAP), and cell density. This predicted relationship is consistent with the trend captured by quantitative analysis and the tentative hypothesis. Furthermore, a Bayesian network is applied to characterize the effect of detachment in genetic mutant mice. A finding from the constructed network confirms the plausibility of a new treatment (gene therapy) by exploring the relationship between retinal detachment and genetic effects, where there is little knowledge of the relationships. The developed model is useful to interpret the experimental data and to develop

new hypotheses for future experiments.

7.1 Introduction

It is important to understand the fundamental cellular events that occur after detachment and reattachment that have the potential to significantly affect the return of vision after successful reattachment [27]. Recent advances in bio-molecular imaging, in particular confocal microscopy, promise to yield insight into the nature of cellular processes of the retina involved with retinal detachment, especially providing information about the changes in cell morphology and the expression patterns of specific proteins associated with retinal detachment. Characterizing these changes helps us to understand the cellular responses to retinal detachment and the generation of secondary effects due to detachment/reattachment.

Most of the analysis thus far has focused on identifying differential measurements, which provide a snapshot of the level of morphological changes for retinal layers and multiple proteins. While these quantitative measurements of a retina provide the basis of biological changes to retinal detachment, they are not sufficient to explain the complex cellular mechanisms. For example, a number of measurements have been developed to differentiate protein expression within Müller cells and rod photoreceptors corresponding to normal and detached retinas. Cell density and thickness profiles have been used to characterize the structural distortion of the ONL in response to retinal detachment. With these quantitative features, we can support the reported qualitative observations of individual events [27]: 1) GFAP within Müller cells are massively spread throughout the ONL; 2) rod opsin proteins are redistributed in the cytoplasm of the cells within the ONL; 3) cell

density and the thickness are decreased after detachment. However, a detailed interpretation of the relationship between these features which improves the understanding of the genesis of retinopathy of detachment remains incomplete; for example, it is still not well understood whether the upregulation of GFAP effects the change in cell density within the ONL. Moreover, there is increasing evidence that retinal detachment does not involve an independent cellular response, but a complex interaction between cells and their environment [27].

Figure 7.1 (from [53]) suggests a tentative hypothesis regarding the pathway of retinopathy of detachment. The hypothesis in Figure 7.1 is from the combination of a long series of results from studies of individual events. It requires the analysis of individual events, such as photoreceptor cell death, and the associated correlation among the results, such as hypertrophy of Müller cells and failure of glutamate recycling by Müller cells. Statistical modeling techniques are very useful in capturing such complex interactions between cells and their associated environments. To properly understand normal cellular responses and their changes in response to retinal detachment, we use a Bayesian network. Bayesian networks have a number of advantages for modeling the retinal detachment process. Bayesian networks can represent complex relationships among multiple interacting proteins and their probabilistic nature can accommodate the incomplete, noisy, and uncertain data which is inhererent in biological data. A detailed understanding of retinal detachment via modeling can provide opportunities to test therapeutic agents that may reduce the damaging effects of detachment or improve the outcome of reattachment surgery. This understanding may also reveal information that leads to an understanding of other causes of blindness rooted in retinal defects or injuries.

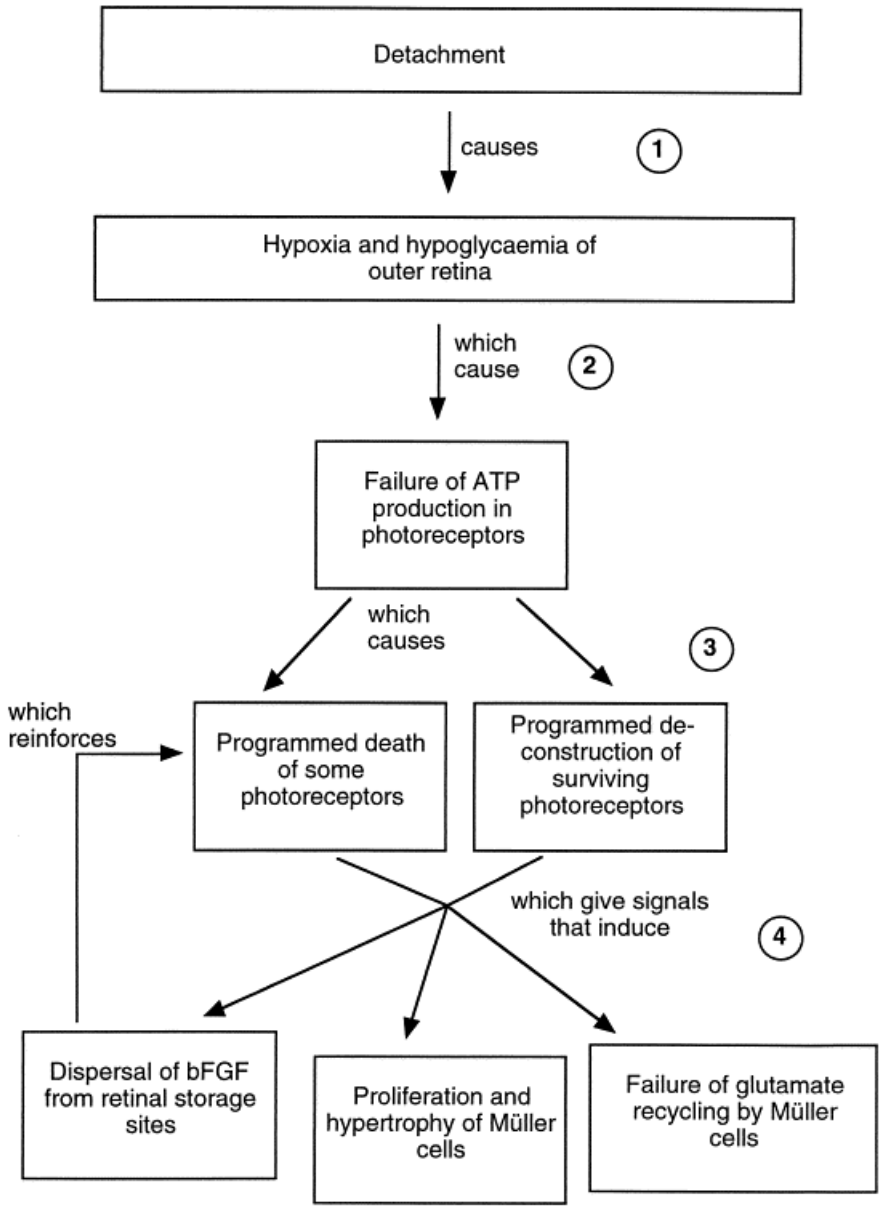

Figure 7.1: Hypothesis of the genesis of retinopathy of detachment. This is a graphical illustration of the conventionally accepted hypothesis in [53]. The first three stages of genesis have a relatively strong empirical base. The sequence of events at stage 4 is more speculative. [53] suggested that the glial responses to detachment are mediated by signals from surrounding neurons as they undergo death or deconstruction. The drawing is courtesy of Geoffrey Lewis [53].

This chapter is organized as follows. We first introduce a Bayesian network approach and its use in modeling the retinal detachment process (Section 7.2.1). The partially unknown structure of the network is learned from the experimental data so that the model can corroborate the observations and reproduce the data that have been observed. A complete network structure learned from the retinal images is presented. In Section 7.2.2, we introduce the interesting influence connection between rod opsin, GFAP, and cell density. This predicted relationship is supported by a quantitative analysis and a tentative hypothesis. Finally, the constructed Bayesian network is applied to characterize the effect of detachment in genetic mutant mice (Section 7.3). An interesting finding from the constructed network confirms the plausibility of a new treatment (gene therapy) by exploring the relationship between retinal detachment and the genetic defect, where there is little knowledge about these relationships.

7.2 Modeling Retinopathy using Bayesian Networks

A Bayesian network is a compact graphical representation of multivariate joint probability distributions for a set of variables. Nodes represent random variables (e.g. the thickness of the ONL) and arcs (directed lines between nodes) represent statistical dependence between variables. The network structure and parameters can be statistically inferred from the observed data. Since the network inference algorithm approximates the most likely model that closely predicts the observed data, a large amount of data is required to estimate the parameters of the network.

The number of features computed along the median curve of the ONL (e.g. local cell density, thickness, and protein expression level) provide a statistically large set of samples that enable Bayesian network inference to accurately predict the pathway of retinopathy. The first three stages shown in Figure 7.1 have a strong empirical support [53], and this partial structure is used to reduce the search space of possible models and also constrain the model approximations in a more biologically plausible way. Figure 7.2 shows one possible workflow for analyzing retinal images data using Bayesian networks.

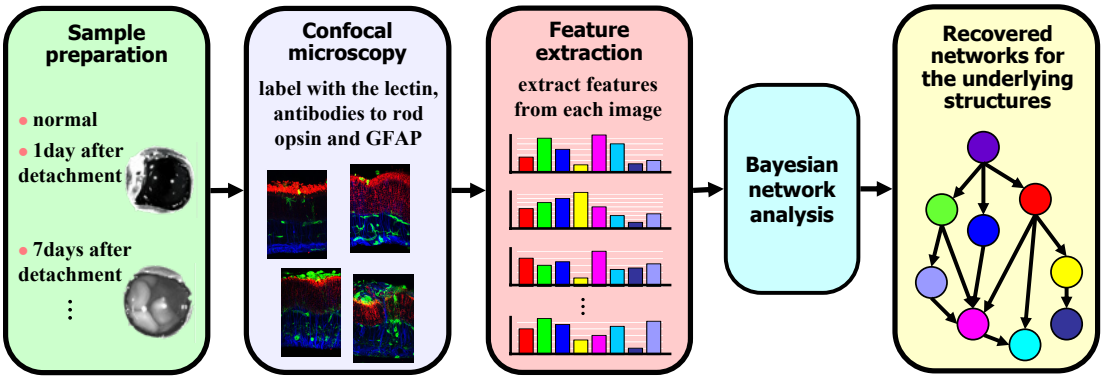

Figure 7.2: Workflow for analyzing retinal images using Bayesian networks.

7.2.1 Bayesian networks construction

We focus on modeling the events related to photoreceptor death/deconstruction, Müller cell proliferation, and microglial activation in response to detachment (Figure 7.3). Since these events are well studied [44], we can use the established observation as a biological basis to evaluate the relevance of the recovered structure. The main goal is to find the dependence among photoreceptors, Müller cells and microglia based on individual cellular responses.

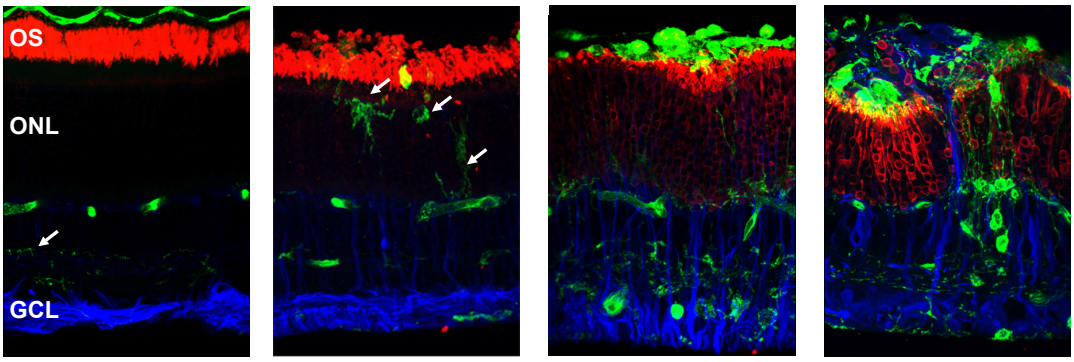

(a) (b) (c) (d)

Figure 7.3: A series of confocal images of normal and detached retina showing the labeling of rod opsin (red), microglial cells (green), and intermediate filament protein GFAP (blue). (a) Normal retina. Only the layer of rod outer segments (OS) labels heavily with antibody to rod opsin. The lectin (green) labels microglia in the inner plexiform layer (IPL) (arrow) and blood vessels in the retina and choroid. GFAP is concentrated in the endfeet of the Müller cells. (b) Retina detached for 1 day. Rod OS begins to degenerate, lectin labeled cells are observed, and Müller cells upregulate GFAP expression. (c) Retina detached for 7 days. Anti-rod opsin is present in the degenerating OS and in the plasma membrane of rod photoreceptors in the ONL. Lectin labeled cells with varied morphologies are distributed throughout the inner and outer retina and in the OS layer. Anti-GFAP labeling extends throughout the retina. (d) Retina detached for 28 days. Anti-rod opsin labeling illustrates the extensive OS degeneration and redistribution of protein. Numerous lectin labeled cells are present throughout retina and in the subretinal glial scar (arrow) labeled with anti-GFAP.

Compute features from retinal images

Images were collected from normal (attached) and detached retinas (1, 3, 7, and 28 days of detachment). For a given image, we measure the thickness, density, distortion indices of thickness and density, and protein distributions within the ONL. To calculate these features, the boundary of the ONL is automatically segmented using graph partitioning active contours (GPAC) with nuclei density information (Section 6.4). We compute a median curve and use it as a basis for

the measurements (Section 5.3). Once the median curve is extracted, it is used to measure the thickness of the ONL, the density of the photoreceptors, and the protein expression levels of rod opsin, lectin, and GFAP. For every location s_i along the median curve, a line $l(s_i)$ orthogonal to that median location is constructed and extended outward to the ONL boundary (Figure 7.4). The thickness at each median location s_i is defined as the length of $l(s_i)$. To compute the density and the protein expression levels, a sliding window $A(s_i)$ bounded by $l(s_i - k \cdot ds)$ and $l(s_i + k \cdot ds)$ is constructed, where k is an integer parameter controlling the size of $A(s_i)$ and ds is the finite length element between adjacent median points (Figure 7.4).

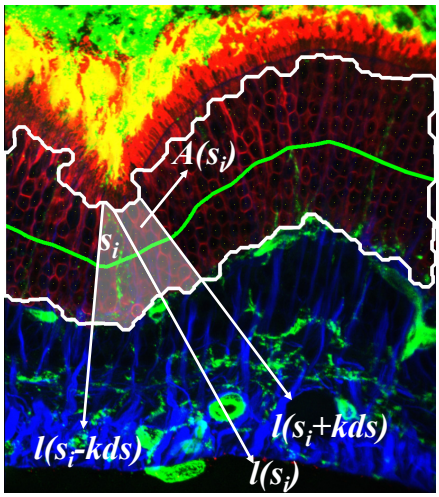

Figure 7.4: Extracting features from the ONL. The median curve, $\vec{l}(s_i)$, and highlighted region $A(s_i)$. At each median point s_i, the thickness is computed as a length of $l(s_i)$ and the density is defined as the number of photoreceptor nuclei within $A(s_i)$ divided by the area of $A(s_i)$. Similarly, the protein expression level is defined as the average intensity within $A(s_i)$.

The density is defined as the number of photoreceptor nuclei located inside $A(s_i)$ divided by the area of the $A(s_i)$. The protein expression level is defined as the

average intensity within $A(s_i)$. The distortion indices of the thickness and density are computed from the thickness and density profiles within a sliding window $A(s_i)$. In summary, eight features are used as a complete data set: thickness at s_i, cell density at $A(s_i)$, Rod opsin expression within $A(s_i)$, Lectin labeling within $A(s_i)$, GFAP expression within $A(s_i)$, distortion index of the thickness profile within $A(s_i)$, and distortion index of the density profile within $A(s_i)$, the experimental conditions (Table 7.1). On average 400 feature vectors are extracted from each image.

Table 7.1: Features derived from the ONL in retinal images.

Feature	Meaning
Thickness	thickness of the ONL at s_i (Section 5.3).
Cell density	photoreceptor density within a sliding window $A(s_i)$ (Section 4.2).
Rod opsin	average intensity of rod opsin expression within a sliding window $A(s_i)$.
Lectin	average intensity of lectin labeling within a sliding window $A(s_i)$.
GFAP	average intensity of GFAP expression within a sliding window $A(s_i)$.
$\mathrm{DI}_{\mathrm{thickness}}$	distortion index of the thickness profile within $A(s_i)$.
$\mathrm{DI}_{\mathrm{density}}$	distortion index of the density profile within $A(s_i)$.
Exp	experimental conditions of detachment.

Learning a Bayesian network

Learning the structure, G, of the Bayesian network is a very challenging problem. The number of potential networks in n nodes is super-exponential in n [17]. For example, in just eight nodes, there are 7.8×10^{11} potential networks [17]. The most common approach to discover the structure of Bayesian network from the data is to define a space of graph models to consider, and set up a scoring function that evaluates how well a model predicts the data. An optimization algorithm is

used to search for the high-scoring model. We use an asymptotic approximation to the full posterior probability called Bayesian information criterion (BIC) [73], which is defined as follows:

$$\log P(G|D) \approx \log P(D|G,\hat{\theta}) - \frac{\log N}{2}|G|, \tag{7.1}$$

where D is the data, N is the number of samples, $\hat{\theta}$ is the maximum likelihood estimate of the parameters θ, $|G|$ is the number of parameters θ. The parameters consist of local conditional probabilities, $p(x_i|\mathbf{pa}(x_i))$, where $\mathbf{pa}(x_i)$ is a parent node of x_i.

We construct a Bayesian network with eight variables $x_1, \ldots, x_8$ which are the computed features from the image and the experimental condition. Figure 7.5 illustrates the pathway of retinal detachment represented as a Bayesian network.

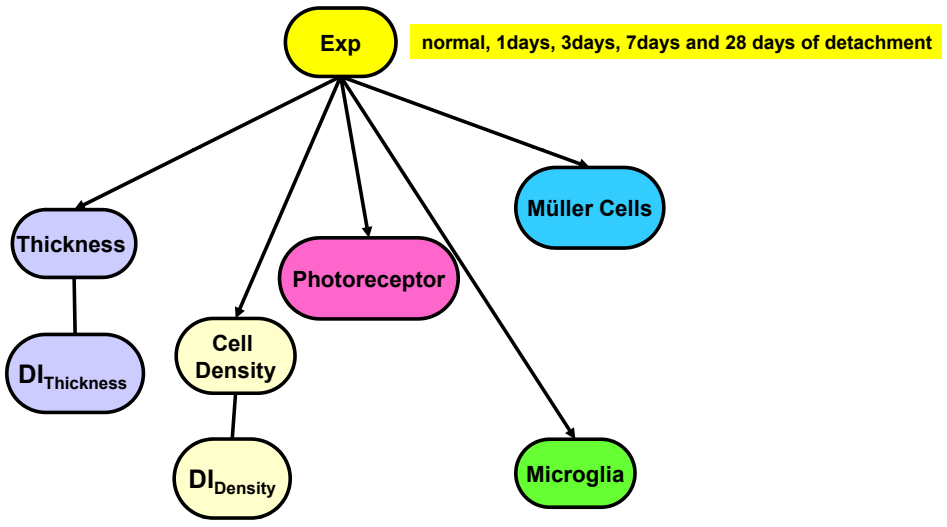

Figure 7.5: The pathway of retinal detachment represented as a Bayesian network. Each node represents a feature extracted from a retinal image. A solid line denotes a connection based on biological knowledge. The rest of the missing arcs will be learned through an inference algorithm.

Some of the arcs between nodes (solid arrows) are already connected based on biological knowledge. There are still missing connections among nodes; for example, no arc between node GFAP and node Lectin indicates the unknown connection between these two. The complete structure, G, including the dependencies between variables are found through hill climbing algorithm using BIC as a scoring function.

Experimental results

95 digital images of normal (10 images) and detached feline retinas (14, 14, 14, and 43 images for 1, 3, 7 and 28 days of detachment) were generated with an Olympus FluoView laser scanning confocal microscope from tissue sections. Tissues are labeled with isolectin B4 and antibodies to rod opsin and GFAP. From each of these images, the feature vectors described in Table 7.1 are computed. On average 400 feature vectors are computed from the ONL in each image. The ONL boundary is automatically segmented using GPAC with nuclei density information (Section 6.4). We compute thickness, cell density, average intensity of rod opsin and GFAP from the each point on the median axis of the ONL. Distortion indices of thickness and density are also computed. 38,000 data points are collected from 95 images and we sample 9,500 data points to learn the structure. The data values in each dimension of 8-dimensional data point are discretized into three categories: low, medium, and high. Since there are still many possible structures (7.8×10^{11}) for eight nodes, we use a greedy hill climbing algorithm [60, 34] to search the optimal network. We start with a candidate network (Figure 7.5), and consider a set of potential modifications, such as addition, removal or reversal of

an edge between nodes. The scoring function, BIC, is evaluated for every modified network. The highest-scoring modified network becomes the current candidate, and the process is repeated until no modified network scores higher than current candidate. Kevin Murphy's Bayes net toolbox [61, 60] is used to find the best network structure.

The resulting causal network structure found through greedy hill climbing algorithm is shown in Figure 7.6. Some results are not surprising, for example, the causal influence of experimental conditions on thickness, cell density, and protein expression levels. On the other hand, the subnetwork associating changes in cell density and expressions of rod opsin and GFAP with detachment at different time points is quite interesting. *This is the first time that these associations have been modeled in a quantitative manner that is reproducible.*

However, the question remains as to how good the selected model is. To answer this, we compute the posterior probability of network structure as follows [34]:

$$P(G|D) = \frac{P(G)P(D|G)}{P(D)}, \tag{7.2}$$

where P(D) is a normalization constant that does not depend on the structure. Since the scoring function estimates maximum likelihood of posterior probability of network, the recovered structure G more likely approximates the observed data as $P(G|D) \rightarrow 1$. The posterior probability $P(G|D)$ of constructed network structure is $\simeq 1$ $(1+1.1\times10^{-12})$, indicating the recovered structure most likely approximates the data.

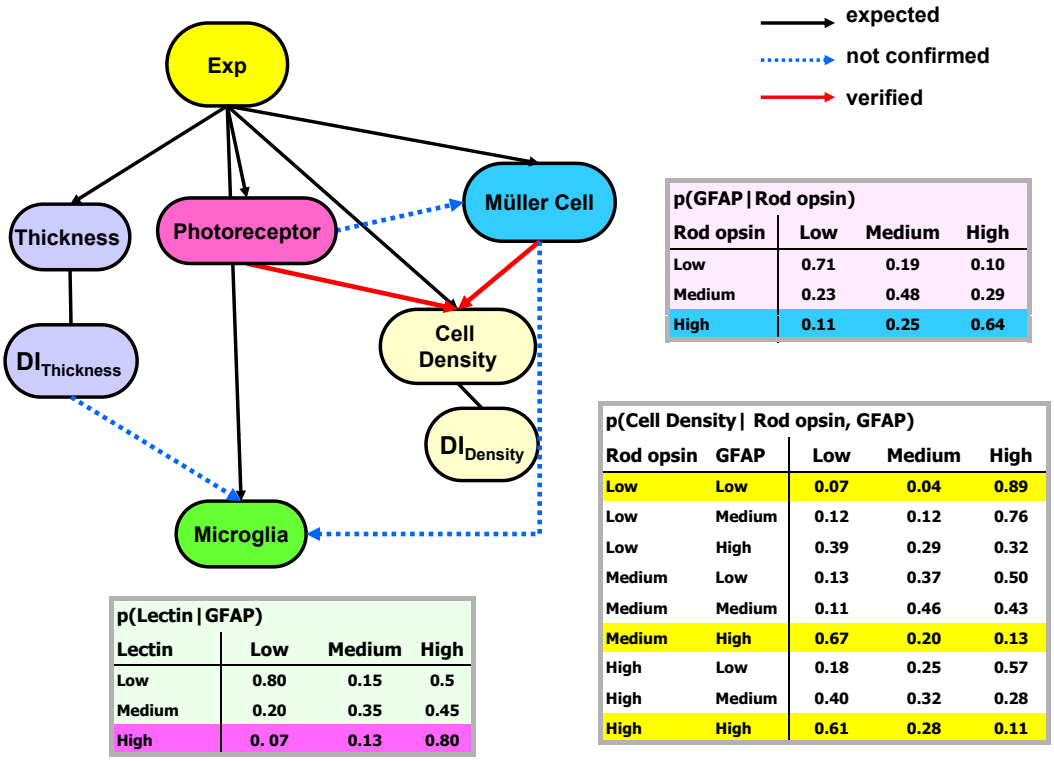

p(GFAP | Rod opsin)

Rod opsin	Low	Medium	High
Low	0.71	0.19	0.10
Medium	0.23	0.48	0.29
High	0.11	0.25	0.64

p(Cell Density | Rod opsin, GFAP)

Rod opsin	GFAP	Low	Medium	High
Low	Low	0.07	0.04	0.89
Low	Medium	0.12	0.12	0.76
Low	High	0.39	0.29	0.32
Medium	Low	0.13	0.37	0.50
Medium	Medium	0.11	0.46	0.43
Medium	High	0.67	0.20	0.13
High	Low	0.18	0.25	0.57
High	Medium	0.40	0.32	0.28
High	High	0.61	0.28	0.11

p(Lectin | GFAP)

Lectin	Low	Medium	High
Low	0.80	0.15	0.5
Medium	0.20	0.35	0.45
High	0. 07	0.13	0.80

Figure 7.6: A recovered Bayesian network of the retinal detachment process and example conditional probability table. The posterior probability $P(G|D) \approx 1$, indicating the recovered structure most likely approximates the data.

7.2.2 Confirmation of predicted network connections

To evaluate the biological relevance of the recovered structure, we compare each arc with the relationship reported in the literature [27, 53, 44]. Arcs are categorized into three classes:

- expected: constructed from the observed dependence,
- not confirmed: the causal relationship is revealed by a Bayesian network, yet the biological explanation is not clear,

- verified: the link between the nodes are not well known, however, we are able to interpret biological meaning and also find the images to support it.

Rod opsin, GFAP, and cell density

Figure 7.7 shows a subnetwork with its conditional probability table. The influence of GFAP and rod opsin on cell density presents the direct relationships between the expression of rod opsin and GFAP, and photoreceptor cell density. The connection predicts that upregulation of the protein expression level is associated with the cell density which is related to photoreceptor cell death. More interestingly, the conditional probability, $p(\text{Cell density}|\text{Rod opsin}, \text{GFAP})$, suggests that the upregulation of rod opsin and GFAP decreases the cell density of photoreceptors (highlighted rows in Figure 7.7).

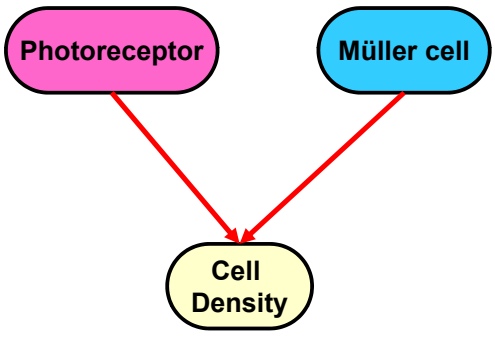

p(Cell Density| Rod opsin, GFAP)

Rod opsin	GFAP	Low	Medium	High
Low	Low	0.07	0.04	0.89
Low	Medium	0.12	0.12	0.76
Low	High	0.39	0.29	0.32
Medium	Low	0.13	0.37	0.50
Medium	Medium	0.11	0.46	0.43
Medium	High	0.67	0.20	0.13
High	Low	0.18	0.25	0.57
High	Medium	0.40	0.32	0.28
High	High	0.61	0.28	0.11

Figure 7.7: Recovered relationship between protein expression levels and cell density. $p(\text{Cell density}|\text{Rod opsin}, \text{GFAP})$ suggests that the upregulation of rod opsin and GFAP decrease photoreceptor cell density. The highlighted rows are reported in [44, 27].

To validate this prediction, we first take a look at the trend of each of these

features (the expression level of GFAP and rod opsin) in response to detachment. Figure 7.8 summarizes the changes in cell density and protein expression levels. In Figure 7.8, Y axis in the left denotes the cell density and one in the right represent the protein expression levels. After detachment, the photoreceptor cell density is decreased while the expression of GFAP within the ONL is monotonically increased. Rod opsin expression is increased after detachment and begins to decrease after 7 days of detachment. This decrease might be related to the decrease in number of photoreceptors so there is less cytoplasm for protein to be redistributed. There is also a tentative hypothesis suggesting that photoreceptors stop producing rod opsin at certain time points after detachment. The predicted connection is consistent with the trend captured by quantitative analysis and this hypothesis.

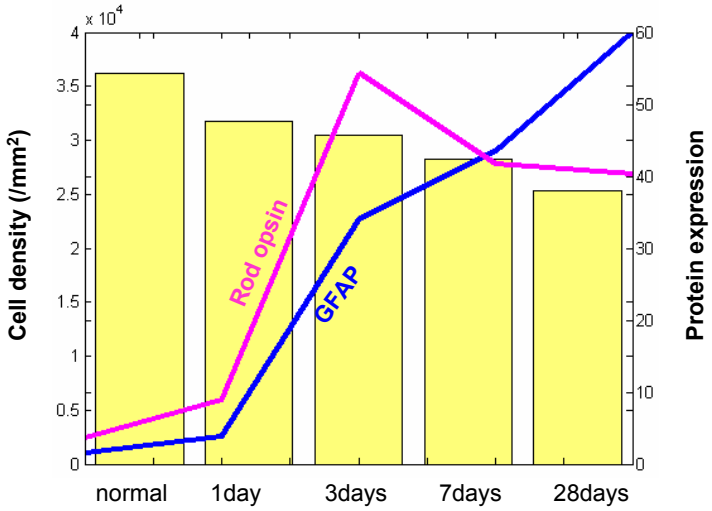

Figure 7.8: Quantitative analysis of cell density and protein expression levels. Cell density is decreased after detachment. Rod opsin expression is increased after detachment and begins to decrease after 7-day detachment. GFAP expression continues to increase, implying the negative relationships with cell density. The observed trend confirms the relevance of the connection shown in Figure 7.7.

Figure 7.9 shows an example image of 3 days of detached retina and its three profiles along the median axis of the ONL. The cell density decreases where high GFAP expression is detected, which suggests that GFAP expression caused by Müller cell hypertropy takes up the space within the ONL due to cell death and ultimately leads to a decrease in cell density. It is still not clear how the rod opsin expression is related to cell density, but the connection is supported by the quantitative analysis.

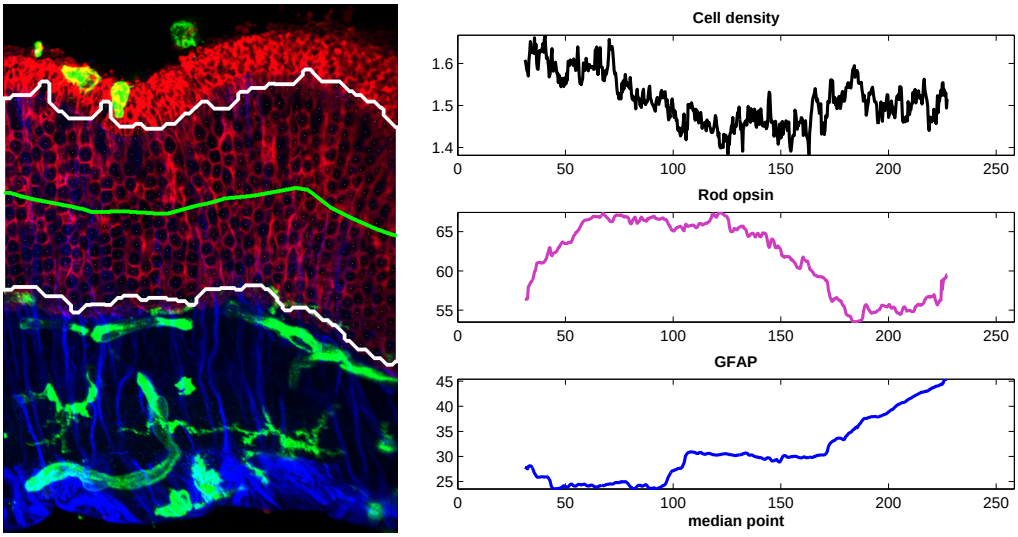

(a) (b)

Figure 7.9: Example image with the profiles of cell density and protein expressions. (a) Example image of a section from a 3 day detached cat retina. The ONL boundary (white) and median axis (green) are overlayed. (b) Profiles are computed from the median axis of the ONL. Photoreceptor cell density, rod opsin expression, and GFAP expression are illustrated starting at the top. As rod opsin and GFAP expression increase, cell density decreases.

GFAP, Rod opsin, and Lectin

The results denoted as "not confirmed" in Figure 7.6 are interesting. Figure 7.10 shows a subnetwork containing three nodes (GFAP, rod opsin, lectin) with its conditional probability table. For example, a connection between GFAP and Lectin suggests that upregulation of GFAP promotes microglial cell activation. A relationship between Müller cells and microglia after detachment has been proposed, yet this interaction is speculative. The influence of rod opsin on GFAP is also difficult to interpret.

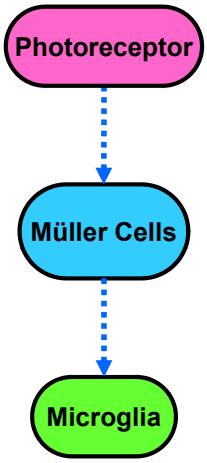

p(GFAP | Rod opsin)

Rod opsin	Low	Medium	High
Low	0.71	0.19	0.10
Medium	0.23	0.48	0.29
High	0.11	0.25	0.64

p(Lectin | GFAP)

Lectin	Low	Medium	High
Low	0.80	0.15	0.5
Medium	0.20	0.35	0.45
High	0. 07	0.13	0.80

Figure 7.10: Recovered relationship among protein expressions of GFAP, rod opsin, and lectin. p(Lectin|GFAP) suggests that the upregulation of GFAP promotes microglial cell activation.

7.3 Characterizing the Effect of Retinal Detachment in Genetic Mutant Mouse

Retinoschisis

Retinoschisis (RS) is an X-linked inherited disease that causes blindness in humans through the mutation of a protein called 'retinoschisin'. The mutation results in the spontaneous formation of breaks or tears in the retina as shown in Figure 7.11. Blindness results from this physical splitting of the retina where holes cause severe tissue degeneration. A possible treatment to prevent blindness is to replace the defective gene by injecting viral vectors carrying the gene. This creates a retinal detachment, however, and little is understood about the additional damage caused by retinal detachment in combination with the missing gene.

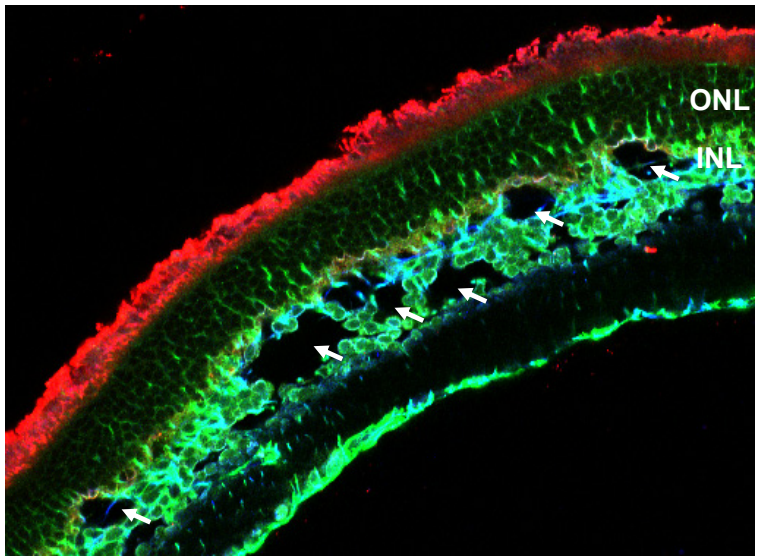

Figure 7.11: Example image of a section from retinoschisin knockout (RSKO) mouse retina mimicking retinoschisis. The lack of the protein, retinoschisin, results in the spontaneous formation of breaks or tears in the retina (denoted by white arrows).

The retinoschisin knockout (RSKO) mouse, a mouse that has been genetically modified to lack the RS gene, is a standard model for the human disease RS. Steve Fisher's group recently started using the RSKO model to study the detachment caused by this gene therapy. More specifically, we would like to use the Bayesian network model developed in the previous section to determine quantitatively the effect of retinal detachment in the mutant mice. Based on quantitative measurements of the images, the general defect of RS is derived from the comparison between the RSKO and wild type (WT) (i.e. normal) mice (Section 7.3.1). The defect is used as a basis to characterize the additional damage in RSKO mice due to the detachment (Section 7.3.2). Finally, extracted features are fed into a Bayesian inference algorithm to learn the interaction between features. From the constructed network, we find that the underlying retinal changes following retinal detachment induce a reduction in the size of existing retinal cavities (Section 7.3.3). This finding has not previously been reported and may lead to a new approach for diagnosis and treatment of RS.

7.3.1 Quantifying the defect of RSKO mice

Before characterizing the effect of the detachment, we compared the retinas of WT to those of RSKO mice to quantify the defect of aberrant gene. Using it as a basis, we can accurately characterize the additional damage to the retina due to the detachment. Figure 7.12 displays an example image of normal retina of WT and RSKO mice. In the RSKO mouse (Figure 7.12 (b)), a number of retinal cavities are observed in the inner nuclear layer (INL). The expression of GFAP is increased and the outer segments (OS) are shortened compared to the WT mouse.

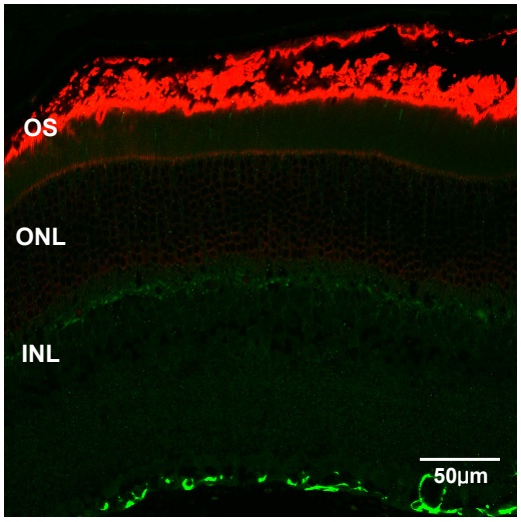

(a)

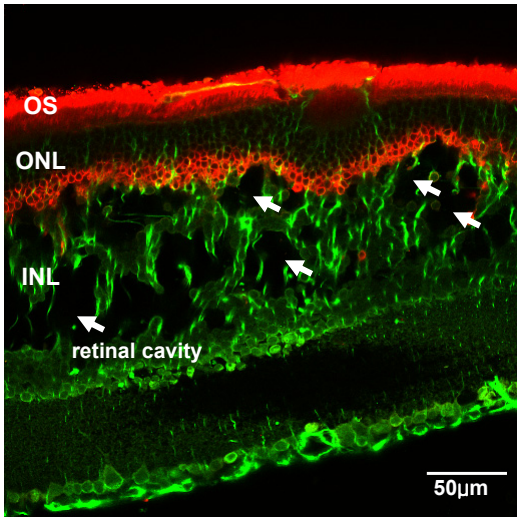

(b)

Figure 7.12: Comparison between WT and RSKO mice. Images are double labeled with antibodies to rod opsin (red) and GFAP (green). (a) A normal retina from a WT mouse. (b) An normal (attached) retina of RSKO mouse. A number of cavities (holes) are shown in the INL (denoted as a white arrow). Compared to WT, more GFAP is expressed throughout the retina, and the ONL appears to be thinner.

We also measure the cell density and distortion index of cell density (Figure 7.13). In RSKO mice, the number of photoreceptor nuclei was slightly decreased compared to WT mice (49,976/mm^2 vs. 51,764/mm^2, Student's t-test[1] $p < 0.007$). The distortion index is increased to 0.04 indicating there is more variation in the local cell density profile; this is significant level of distortion index. This suggests a spatial rearrangement of photoreceptors within the ONL.

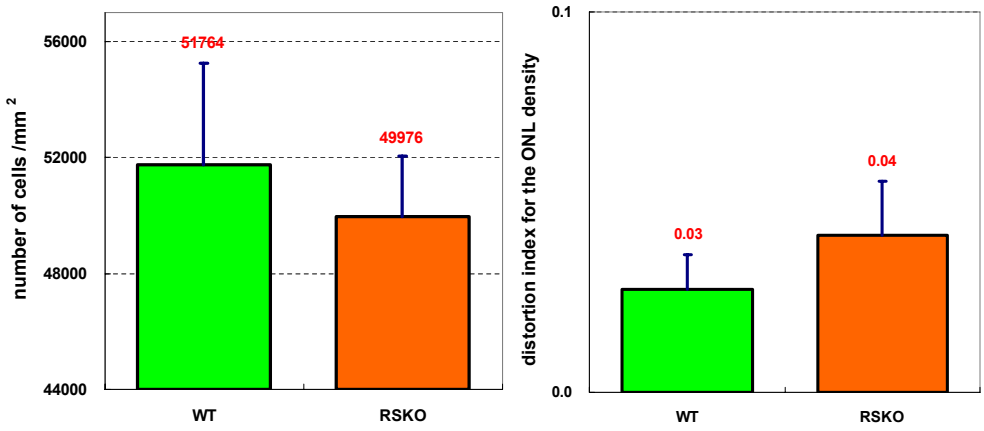

(a) (b)

Figure 7.13: Photoreceptor cell density and distortion index of WT and RSKO mice. (a) Cell density. The number photoreceptor nuclei in RSKO mice was slightly decreased compared to WT mice (49,976/mm^2 vs. 51,764/mm^2, $p < 0.007$). (b) Distortion index of cell density. It measures the variation of the local cell density profile. RSKO mice has a higher distortion index indicating more rearrangement of photoreceptor nuclei.

Similarly the thickness of the ONL is significantly reduced in RSKO mice (40 μm vs. 59 μm, $p < 1\times10^{-17}$) (Figure 7.14). Considering the slight change in cell density, this significant decrease of thickness implies that there is a smaller number (not density) of photoreceptors in RSKO mice. Additionally, the distortion

[1]Student's t-test assesses whether the means of two groups are *statistically* different from each other [82]. Usually the returned p value is less than 0.05, two groups are considered significantly different.

index of thickness indicates there is more structural distortion within the ONL in RSKO mice. Usually, the distortion index of normal mouse retina is less than 0.1. In summary, the quantitative/qualitative data indicates that damage already exists to the retina due to the aberrant retinoschisin gene, and is *not caused by detachment*.

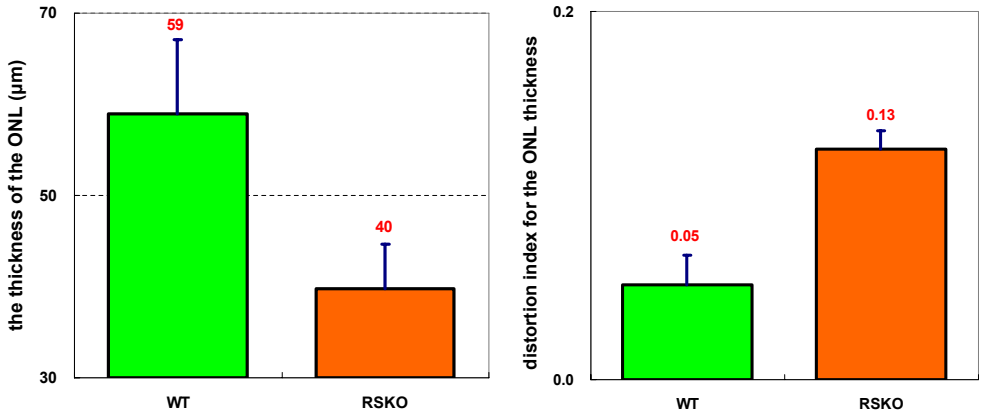

(a) (b)

Figure 7.14: Thickness of the ONL and distortion index of WT and RSKO mice. (a) Thickness of the ONL. The thickness of the ONL is significantly reduced in RSKO mice (40 μm vs. 59 μm, $p < 1\times10^{-17}$). (b) Distortion index of thickness. Distortion index of thickness in RSKO mice increased significantly indicating more structural distortion in the ONL.

7.3.2 Quantifying the effect of detachment in RSKO mice

Detachments were made in the right eyes of RSKO mice by injecting saline between the retinal pigment epithelium (RPE) and neural retina, which mimics gene therapy injections. The left eyes served as controls. Eyes were removed after 1, 7, and 28 days of detachment. It is known that mouse retinas detached with saline will reattach spontaneously within 24 hours, thus, all retinas in the study are

considered detached for 1 day followed by 0, 6, and 27 days of reattachment. 296 digital images (115, 68, 56 and 57 images for control, 1, 7, 28 days of detachment) were collected using an Olympus FluoView confocal microscope. The size and number of retinal cavities, the thickness of the INL and ONL, and the number of photoreceptor nuclei are quantified.

Photoreceptor cell density

Following detachment/reattachment in RSKO, there is a slight decline in the number of photoreceptors (Figure 7.15). It is not surprising that the number of photoreceptors is decreased since it is a commonly observed cellular event initiated by detachment. Note that the loss is marginal.

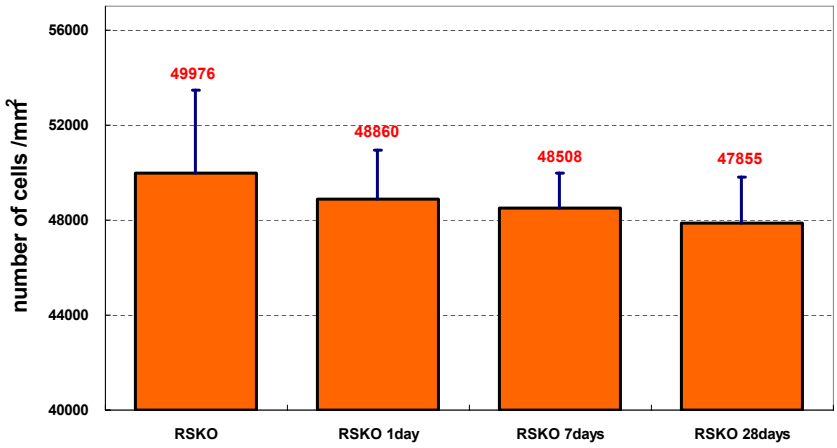

Figure 7.15: Photoreceptor cell density of RSKO mice after 1 day of detachment and reattachment. Following detachment/reattachment in RSKO, there is further decline in the number of photoreceptors.

Thickness of the ONL and the INL

We find a large variation in the thickness of the ONL and the INL in RSKO mice (Figure 7.16). We suspect that the thickness of the nuclear layers is affected by the location of the retina in the eye; peripheral retina being thinner than central retina. To eliminate this variation, we measure the thickness of the entire retina. The thickness of the INL and the ONL is then normalized to the thickness of the tissue. Following detachment/reattachment in RSKO mice, there is no change in the thickness of the ONL with respect to the thickness of the tissue. The ratio of thickness of the ONL to tissue remains the same at 0.21. On the other hand, the ratio of the thickness of the INL to tissue decreases (0.33 to 0.3) after detachment/reattachment. This can be explained by a decrease in the area of retinal cavities within the INL after detachment/reattachment.

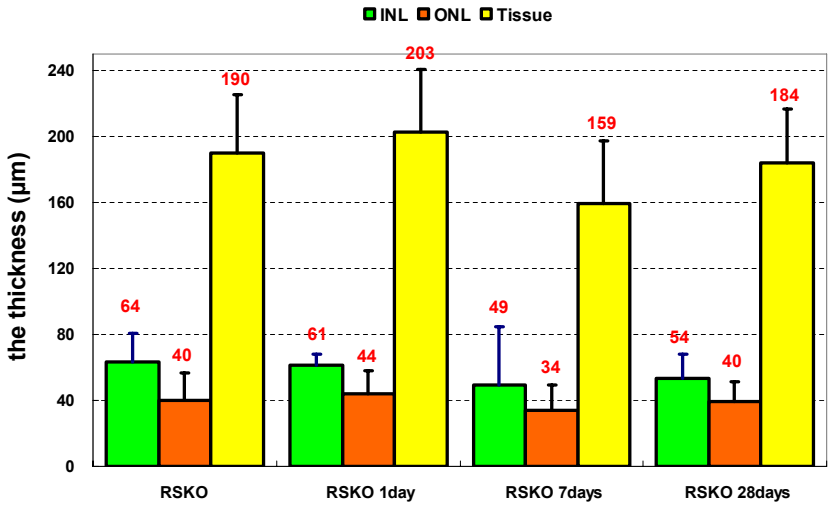

Figure 7.16: Thickness of the ONL in RSKO mice after detachment. Thickness of the INL (green), ONL (orange), and tissue (yellow) are measured. Following detachment/reattachment in RSKO, there is no change in the thickness of the ONL with respect to the thickness of the tissue. The ratio of thickness of the ONL to tissue remains the same as 0.21.

Retinal cavities

We manually draw the boundaries of retinal cavities as shown in Figure 7.17 (a). The number of cavities are counted from each image and normalized to the length of the INL. The average area of the cavities is computed and normalized to the area of the INL [(area of a hole/area of the INL)×100]). Additionally, we extract the medial axis of the INL, the average area of cavities within sliding window $A(s_i)$ is measured from each median point. The window size is the same as that used to measure the cell density in the ONL. The reason for measuring the local average area of the cavities is to find a correlation between photoreceptor cell density and the location of the cavities.

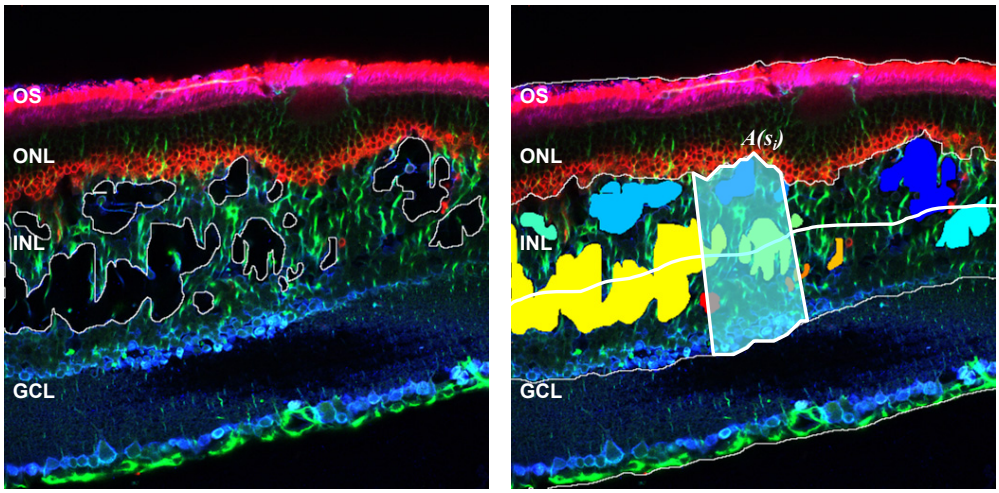

(a) (b)

Figure 7.17: Measuring features of the retinal cavities. (a) An example image of RSKO mice with drawn retinal cavities. (b) A schematic drawing of measurements. The number of cavities are counted and normalized to the length of the INL. The average area of the cavities is computed and normalized to the area of the INL. Similar to measurement of the ONL, the average area of cavities within a sliding window $A(s_i)$ is measured from each median point on the medial axis of the INL.

We find that the number of cavities within the INL does not change. Interestingly, the average area of cavities is reduced after detachment/reattachment (Figure 7.18 (a)). After a 28-day detachment/reattachment, the average area of the cavities is decreased to 8.46% compared to RSKO (17.48 %, $p < 1.5\times10^{-10}$). Figure 7.18 (b),(c), and (d) show the comparison between left eye (control) and right eye (detached for 1 day followed by 0,6, 27 days of reattachment respectively) from the same animal. In spite of the variation across the animals, the trend is the same, i.e. the cavities are smaller after detachment. One possibility to explain this is that the Müller cells (or RPE) begin to "pump" more fluid from the retina after they become activated by detachment. Both of these cell types have specific molecules designed for the removal of fluid. The idea needs to be tested through further experiments.

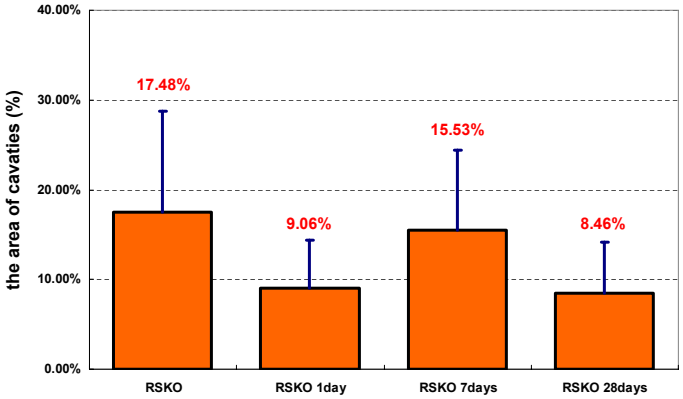

(a)

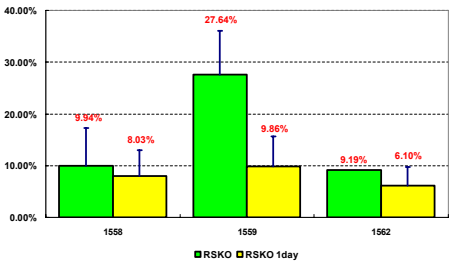

(b)

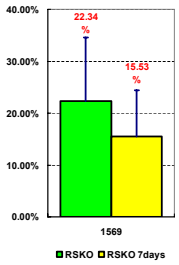

(c)

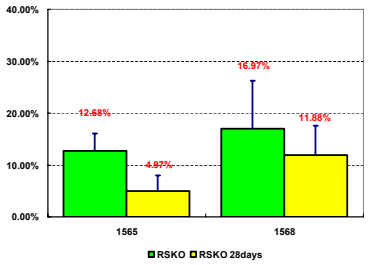

(d)

Figure 7.18: Quantitative analysis of retinal cavities. (a) The average area of cavities is reduced after detachment/reattachment. The significant decrease in the 7-day detachment/reattachment time point is due to variations among animals. After 28-days detachment/reattachment, the average area of the cavities is decreased as 8.46% compared to RSKO (17.48%, $p < 1.5\times10^{-10}$). (b) Average area of the cavities after 1 day of detachment. The graph shows the average area of cavities of three different animals. Some animals (animal ID: 1559, in the middle) show more retinal cavities than others. (c) Average area of the cavities detached for 1 day followed by 6 days of reattachment. (d) Average area of the cavities detached for 1 day followed by 27 days of reattachment. (b), (c), and (d) illustrate the variation of area of cavities among animals. However, the trend is still the same.

7.3.3 Finding the relationships in RSKO mice using the Bayesian network

We find that the average area of retinal cavities of 28 days detached retinas is reduced by 51% compared to normal RSKO retina ($p < 1.5\times 10^{-10}$) (Section 7.3.2). This is unexpected and it is an open question as to what underlying retinal changes following retinal detachment causes a reduction in the size of existing retinal cavities (holes). To discover any relationships presented between the features (photoreceptor cell density, the thickness of the ONL, and the average area of the retinal cavities), we again used the Bayesian network approach.

For the Bayesian network, we first construct a network with four variables: experimental conditions (control, 1 day, 7 days, and 28 days), photoreceptor cell density, the thickness of the ONL, and the average area of the retinal cavities within the INL. 100,000 data points are collected from 296 images but we use 10,000 data points to learn. The data values of each point are discretized into three categories: low, medium, and high. We enumerate all 435 possible structures, and score each structure. The highest scoring network is selected through the brute-force search. The resulting causal network structure found through an exhaustive search over all structures are shown in Figure 7.19. We find three high confidence connections that appeared in at least 80% networks. Two of them are expected; the experimental conditions affect both the cell density and the area of the retinal cavities. These are supported by the quantitative analysis shown in Section 7.3.2.

The connection between cell density and the average area of cavities is more interesting. To validate the biological relevance of the connection, the profiles of thickness, cell density, and area of the cavities are analyzed. Figure 7.20 shows an

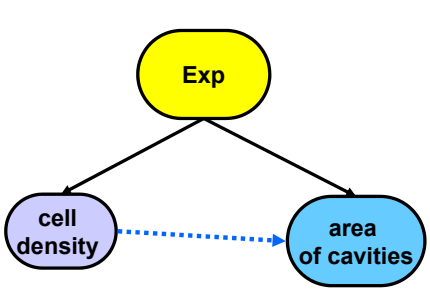

expected

not confirmed

p(cell Density | Exp. cond.)

Cell density	control	1d	7d	28d
Low	0.12	0.10	0.30	0.58
Medium	0.20	0.29	0.61	0.24
High	0.68	0.61	0.29	0.15

p(area of Cavities | Exp. cond.)

area of Cavities	control	1d	7d	28d
Low	0.11	0.54	0.31	0.59
Medium	0.10	0.39	0.40	0.34
High	0.79	0. 07	0.29	0.17

p(area of Cavities | cell Density)

area of Cavities	Low	Medium	High
Low	0.24	0.23	0.51
Medium	0.23	0.35	0.24
High	0.53	0.42	0.25

Figure 7.19: A recovered network of RSKO data and conditional probability table. Through the exhaustive search of possible 543 networks, the highest scoring network is selected. High confidence arcs which are appeared at least 80% of networks are displayed.

example image of an attached retina of a RSKO mouse, and its thickness, density and area profiles. While the thickness profile of the ONL does not change across the median axis of the ONL, the density of photoreceptors varies dramatically (Figure 7.20 (b)). Additionally, the area of the cavities varies along the medial axis of the INL correlates with a change in photoreceptor cell density. When we calculate the Pearson product-moment correlation coefficient[2] [81] between cell density and area of cavities, the correlation coefficient is -0.54. According to

[2]It is a measure of the correlation of two variables X and Y measured on the same object, that is, a measure of the tendency of the variables to increase or decrease together. For a set of N data pairs (x_i, y_i), it is defined as follows:

$$\mathrm{Corr}_{\mathrm{pearson}}(X,Y) = \frac{\sum_{i=1}^{N}(x_i-\overline{x})(y_i-\overline{y})}{\sqrt{\sum_{i=1}^{N}(x_i-\overline{x})2}\sqrt{\sum_{i=1}^{N}(y_i-\overline{y})2}},$$

where $\overline{x}$ and $\overline{y}$ are the means of the data X and Y.

Cohen's interpretation of the correlation coefficient [15]; a correlation of -0.54 is regarded as a very large 'negative' correlation. The strong negative correlation combined with the causal link from the network supports the hypothesis that underlying retinal changes following retinal detachment causes a reduction in the size of existing retinal cavities. It is still not clear how photoreceptors are associated with the retinal cavities, and more work is needed to study these associations.

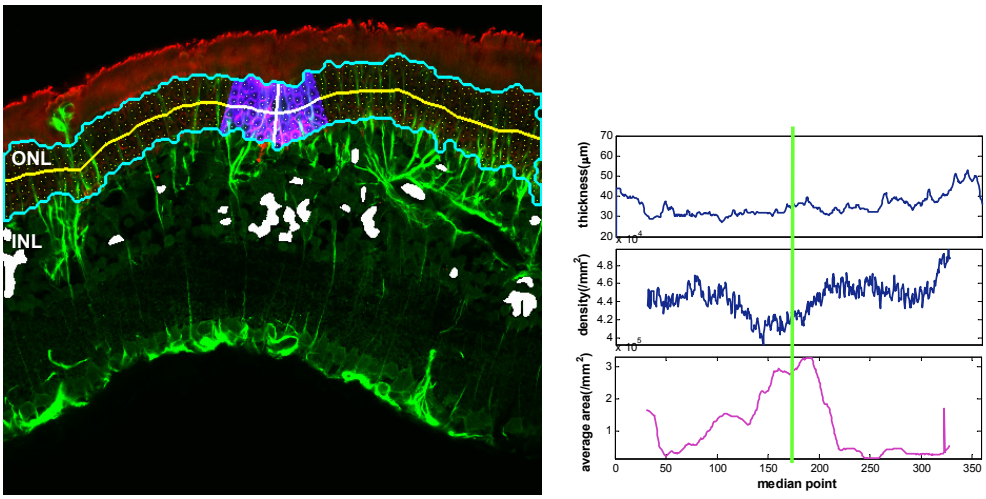

(a) (b)

Figure 7.20: Example image of RSKO mouse retina and its profiles. (a) An attached retina of RSKO mouse labeled with antibodies to rod opsin and GFAP. ONL boundary and medial axis are overlayed. The retinal cavities in the INL are displayed in white. (b) Profiles of thickness of the ONL, photoreceptor cell density, and the average area of the retinal cavities (from the top). Cell density and the area of cavities shows a strong negative correlation (Pearson's correlation coefficient: -0.6076).

In summary, these data indicate that short term (1-day) detachments in RSKO mice followed by a period of reattachment does not accentuate the damage to the retina already underway due to the aberrant retinoschisin gene and may in fact reduce the size of existing retinal lamellar cavities. This suggests that performing

a subretinal injection for the delivery of therapeutic agents may be a viable option in the treatment of retinoschisis.

7.4 Summary

We model the retinal detachment process using a Bayesian network, to analyze the direct influence between proteins, and to understand the effect of detachment. A Bayesian network constructed with quantitative features derived from retinal images not only elucidates most of the traditionally reported relationships, but also predicts correlation among rod opsin, GFAP, and cell density. Secondly, we quantify the defect of the aberrant retinoschisin gene to characterize the additional damage to the retina due to the detachment. Quantitative analysis and the constructed Bayesian network suggest that short term (1-day) detachments in RSKO mice followed by a period of reattachment does not accentuate the damage to the retina already underway due to the aberrant retinoschisin gene. Furthermore, a new finding from the constructed network implies that the change in photoreceptor cell density causes a reduction in the size of existing retinal lamellar cavities. This suggests that performing a subretinal injection for the delivery of therapeutic agents may be a viable option in the treatment of retinoschisis.

We find that the developed model is useful for interpreting the experimental data and to test hypotheses for future experiments. A detailed understanding of retinal detachment via modeling can provide opportunities to test therapeutic agents that may reduce the damaging effects of detachment or improve the outcome of reattachment surgery. It may also reveal information leading to an understanding other causes of blindness rooted in retinal defects or injuries.

Chapter 8

Conclusions and Future Work

"It was six men of Indostan, To learning much inclined,
Who went to see the Elephant (Though all of them were blind),
That each by observation Might satisfy his mind."

John Godfrey Saxe's version of "The blind men and the elephant"

Bio-molecular images are very complex and rich in information, increasing both the difficulty as well as the potential for image analysis and data mining. Each image has unique characteristics, because these images typically obtained to address specific questions or hypotheses. There is often a great deal of time and labor involved in preparing the tissue or cells even before the images are taken, and image acquisition itself can be very time and labor consuming. This thesis is motivated by a desire to provide a detailed quantitative description of the images that would help in a better understanding of the underlying biological processes.

Even though our approach has produced some tangible results for quantifying the cellular changes of the retina, we acknowledge much remains to be done. We conclude in the following with potential future research directions which we believe

will advance the analysis of bio-molecular images.

8.1 3-D Image Analysis for Characterizing Morphology of Cells/Tissues

We observed that it is difficult to analyze the morphology of cellular structures using 2-D images. For example, a long thin structure like the axon of a neuronal cell can appear as either a circle or a line depending on the sectioning orientation. Additionally, the geometrical relationships among cells may be misinterpreted using 2-D images. It is necessary to reconstruct the 3-D view of the structure for analyzing the morphology of a single cell and geometrical relationship among cells.

The primary value of a confocal microscope is its ability to create optical sections through a 3-D specimen. Moreover, it is possible to reconstruct 3-D volumetric representations by assembling a stack of 2-D images along the vertical axis (i.e. z direction). This property of the confocal laser scanning microscopy (CLSM) is fundamental for solving 3-D biological problems where information from regions distant from the plane of focus can obscure the image (thick objects such as brain or retina). The pixel size in the z-direction is much larger than the xy-direction leading to a challenge in computing features in 3-D. We, however, foresee that the extension of our approach to 3-D worth pursuing to provide more accurate information of the cellular structure of retina. Reconstructing a 3-D view will be of immediate benefit in answering numerous questions ranging from the branching pattern of a single cell (e.g. ganglion cell) to the interaction between

the second-order neurons and Müller cells.

8.2 Integrated Image Analysis of Multiple Scale and Multiple Modalities

We investigated high resolution retinal imaging techniques: CLSM, transmission electron microscope (TEM), and high resolution transmitted light microscopes. These techniques are used depending on the goal of the study and each imaging technique reveals information about a tissue in different scales (from molecular to cellular) and resolutions (from nm to μm). When biologists want to confirm an observation made from CLSM, they turn to TEM for more detailed and structural information. With the increasing availability of biological structural data that spans multiple scales and imaging modalities, it is required to develop a method to integrate the information from multiple scales and modalities. While a number of methods have been developed to represent subcellular, cellular, and tissue structure at different scales and modalities, few have been explored the fusion of such information. Building a hierarchical model that interconnects multi scale data sets, and represents a realistic model, is a very challenging problem. However, the potential benefit is great, by providing simulation of retinal tissue after injury that will rapidly promote the understanding of cellular mechanisms of retina.

8.3 Visualization of Retinal Detachment

Cellular responses from different time points give crucial information about cellular mechanisms underlying the complex responses to retinal detachment and reattachment. Additionally biologists want to extrapolate information found for one species to another, and in doing so find general information true for a range of species, for example all mammals. One possible solution to capture time-varying quantitative information within and across species is to compose a visualization demonstrating biological changes in time. This information is presented in a picture consisting of quantification information interpolated from statistics of features from the observed data set. First, we need to model changes in the morphology of a single cell such as a cone photoreceptor over time. For example, features such as shape, number of cells and texture are calculated from data sets at each time point. This data will be fitted to a time-varying model. The picture at an arbitrary time point will be synthesized to fit interpolated statistics derived from the model. The ultimate goal is to synthesize a retinal image at any arbitrary time point capturing all the changes in features corresponding to cells in a retinal image.

8.4 Summary

We developed novel methods for quantitative analysis and modeling of confocal retinal images. We proposed an automated nucleus detection method which provides reliable and consistently accurate results for counting cell nuclei. The nucleus detector greatly reduces the variability across experiments and the sampling

error caused by picking a subset of data to analyze. Additionally, we proposed quantitative measurements to characterize the structural distortion of retina, including layer thickness, local cell density, and distortion indices. We found that the quantitative analysis for retinal images not only corroborates the conclusions derived from manual measurements and qualitative assessments, but also provides new information about structural changes during retinal detachment. Finally, we proposed a quantitative modeling of retinal detachment process for learning complex interactions between cells, proteins, and their environment. We investigated the use of Bayesian networks as a statistical modeling tool to build a model for analyzing direct influence among proteins associated with retinal detachment. The constructed network implies the interaction between cells and protein, for example, the correlation among cell density, glial fibrillary acid protein (GFAP), and the distribution of rod opsin, after detachment. We found that a detailed understanding of retinal detachment via modeling can provide opportunities to test therapeutic agents that may reduce the damaging effects of detachment or improve the outcome of reattachment surgery.

Statistical modeling in combination with quantitative analysis provides biologists with the opportunity to resolve the problem which could not be solved before, and further leads to novel findings in cell biology.

Bibliography

[1] BioQuant: Image analysis system. http://www.bioquant.com/. Last visited: Aug 24th, 2006.

[2] MetaMorph: the complete imaging solution. http://www.universal-imaging.com/products/metamorph/. Last visited: May 3rd, 2007.

[3] M. Abercrombie. Estimation of nuclear population from microtome sections. *The Anatomical Record*, 94:239–247, 1946.

[4] D. Anderson, W. Stern, S. Fisher, P. Erickson, and G. Borgula. Retinal detachment in the cat: the pigment epithelial-photoreceptor interface. *Invest Ophthalmol Vision Science*, 24:906–926, 1983.

[5] G. H. Ball and D. J. Hall. A clustering technique for summarizing multivariate data. *Behavioral Science*, 12:153–155, 1967.

[6] A. Baumberg. Reliable feature matching across widely separated views. In *Proc. of IEEE Conference on Computer Vision and Pattern Recognition*, pages 774–781, Hilton Head Island, South Carolina, June 2000.

[7] J. R. Bergen and M. S. Landy. *Computational Modeling of Visual Texture Segregation*. Computational Models of Visual Processing,M. Landy and J. A. Movshon (editors).

[8] L. Bertelli, B. Sumengen, B. S. Manjunath, and F. Gibou. A multi-phase level sets framework for pairwise similarity-based image segmentation. Technical report, Nov 2006.

[9] J. Byun, M. R. Verardo, N. Vu, D. Fedorov, G. P. Lewis, S. K. Fisher, and B. S. Manjunath. Quantifying structural distortions in retinal tissue before and after injury. In *2006 Workshop on Multiscale Biological Imaging, Data Mining & Informatics*, Sep 2006.

[10] J. Byun, N. Vu, B. Sumengen, and B. S. Manjunath. Quantitative Analysis of Immunofluorescent Retinal Images. In *IEEE International Symposium on Biomedical Imaging: From Nano to Macro (ISBI)*, Arlington, Virginia, USA, April 2006.

[11] J. Byun, L. Wang, G. P. Lewis, S. K. Fisher, and B. S. Manjunath. Challenges in Bio-molecular Imaging and Information Discovery: Developing a Searchable, Distributed Retinal Image Database. In *The Association for Research in Vision and Ophthamalogy (ARVO)*, Fort Lauderdale, Florida, April 2004.

[12] J. Canny. Finding edges and lines in images. Technical report, MIT Artificial Intelligence Laboratory AITR-720, 1983.

[13] T. F. Chan and L. A. Vese. Active contours without edges. *IEEE Transactions on Image Processing*, pages 266–267, 2001.

[14] Y. Choi, C. S. Won, Y. M. Ro, , and B. S. Manjunath. *Texture Descriptors*. Introduction to MPEG-7, Multimedia Content Description Interface, B. S. Manjunath, P. Salembier and T. Sikora (editors), Jun 2002.

[15] J. Cohen. *Statistical power analysis for the behavioral sciences (2nd ed.)*. Hillsdale, N.J, 1988.

[16] B. Cook, G. P. Lewis, S. K. Fisher, and R. Adler. Apoptotic photoreceptor degeneration in experimental retinal detachment. *Investigative Ophthalmology and Visual Science*, 36(6):990–996, 1995.

[17] G. F. Cooper and E. Herskovits. A bayesian method for the induction of probabilistic networks from data. *Machine Learning*, 9(4):309–347, 1992.

[18] D. Demandolx and J. Davoust. Multiparameter image cytometry: from confocal micrographs to major subcellular structures in fluorescence microscope images of hela cells. *Bioimaging*, 5(3):159–169, 1997.

[19] A. P. Dhawan. A review on biomedical image processing and future trends. *Comput Methods Programs Biomed.*, 31(3-4):141–183, 1990.

[20] P. Dimitrov, C. Phillips, and K. Siddiqi. Robust and efficient skeletal graphs. In *Conference on Computer Vision and Pattern Recognition*, 2000.

[21] R. O. Duda and P. E. Hart. *Pattern Classification and Scene Analysis*. John Wiley & Sons Inc, 1973.

[22] J. S. Duncan and N. Ayache. Medical Image Analysis: Progress over Two Decades and the Challenges Ahead. *IEEE Trans. on Pattern Analysis and Machine Intelligence (PAMI)*, 22(1):85–105, 2000.

[23] P. A. Erickson, S. K. Fisher, D. H. Anderson, W. H. Stern, and G. A. Borgula. Retinal detachment in the cat: The outer nuclear and outer plexiform layers. *Investigative Ophthalmology and Visual Science*, 24(7):927–942, 1983.

[24] D. Fedorov, L. M. G. Fonseca, C. Kenney, and B. S. Manjunath. Automatic registration and mosaicking system for remotely sensed imagery. In *SPIE 9th International Symposium on Remote Sensing*, Sep 2002.

[25] J. C. Fiala. Reconstruct: a free editor for serial section microscopy. *Journal of Microscopy*, 218:52–61, 2005. http://synapses.bu.edu/tools/. Last visited: Aug 24th, 2006.

[26] S. K. Fisher, J. Byun, D. Fedorov, N. Vu, B. Sumengen, M. Verardo, G. P. Lewis, and B. S. Manjunath. Image informatics tools for the analysis of retinal images. In *Invest Ophthalmol Vision Science 2006;47: Association for Research in Vision and Ophthalmology (ARVO) E-Abstract 4225*, Apr 2006.

[27] S. K. Fisher, G. P. Lewis, K. A. Linberg, and M. R. Verardo. Cellular remodeling in mammalian retina: results from studies of experimental retinal detachment. *Progress in Retinal and Eye Research*, 24:395–431, 2005.

[28] S. K. Fisher, M. Verardo, J. Byun, G. P. Lewis, G.Luna, S.Kjellstrom, and P.Sieving. Retinal changes following experimental retinal detachment in the retinoschisin knockout mouse. In *The Association for Research in Vision and Ophthamalogy (ARVO)*, Fort Lauderdale, Florida, April 2007.

[29] L. M. J. Florack, B. M. terHaar Romeny, J. J. Koenderink, and M. A. Viergever. Scale and the differential structure of images. *Image and Vision Computing*, 10(6):376–388, July/August 1992.

[30] W. Förstner and E. Gülch. A fast operator for detection and precise location of distinct points, corners and center of circular features. In *Proc. of ISPRS Intercommission Conference on Fast Processing of Photogrammetric Data, Interlaken, Switzerland*, pages 281–305, June 2-4 1987.

[31] N. Friedman, M. Linial, I. Nachman, and D. Pe'er. Using bayesian network to analyze expression data. *Journal of Computational Biology,*, 7:601–620, 2000.

[32] R. C. Gonzalez and R. E. Woods. *Digital Image Processing*. Addison-Wesley Pub, 1992.

[33] C. Harris and M. Stephens. A combined corner and edge detector. In M. M. Matthews, editor, *Proc. of the 4th ALVEY vision conference*, pages 147–151, University of Manchester, England, Septemeber 1988.

[34] D. Heckerman. A tutorial on learning bayesian networks. Technical report, Microsoft Research Advanced Technology Division, 1996.

[35] V. Howard, S. Reid, A. Daddeley, and A. Boyde. Unbiased estimation of particle density in the tandem scanning reflected light microscope. *Journal of Microscopy*, 138:203–212, 1985.

[36] ImageJ. ImageJ:Image processing and analysis in Java, 2005. http://rsb.info.nih.gov/ij/images/ [visited Sep 18th, 2005].

[37] J.Byun, M. R. Verardo, B. Sumengen, G. P. Lewis, B. S. Manjunath, and S. K. Fisher. Automated tool for the detection of cell nuclei in digital microscopic images: Application to retinal images. *Molecular Vision*, 12:949–960, Aug 2006.

[38] T. Joachims. Making large-Scale SVM Learning Practical. In B. Schkopf, C. Burges, and A. Smola, editors, *Advances in Kernel Methods - Support Vector Learning*. MIT Press, 1999.

[39] C. Kenney, B. Manjunath, M. Zuliani, G. Hewer, and A. Van Nevel. A condition number for point matching with application to registration and post-registration error estimation. *IEEE Transactions on Pattern Analysis and Machine Intelligence*, 25(11):1437–1454, November 2003.

[40] C. Kenney, M. Zuliani, and B. Manjunath. An axiomatic approach to corner detection. In *Proc. of IEEE Conference on Computer Vision and Pattern Recognition*, pages 191–197, San Diego, California, June 2005.

[41] C. S. Kenney, B. S. Manjunath, M. Zuliani, M. G. A. Hewer, and A. V. Nevel. A condition number for point matching with application to registration and postregistration error estimation. *IEEE Transactions on Pattern Analysis and Machine Intelligence*, 25(11):1437–1454, Nov 2003.

[42] A. D. Kim, P. Muller, and M. Vannucci. *Bayesian Inference for Gene Expression and Proteomics*. Cambridge University Press, 2006.

[43] G. P. Lewis, D. G. Charteris, C. S. Sethi, and S. K. Fisher. Animal models of retinal detachment and reattachment: identifying cellular events that may affect visual recovery. *Eye*, 16(4):375–387, 2002.

[44] G. P. Lewis, C. S. Sethi, K. M. Carter, D. G. Charteris, and S. K. Fisher. Microglial cell activation follwing retinal detachment: a comparison between species. *Molecular Vision*, 11:491–500, 2005.

[45] Z. Li, M. O. Tso, H. M. Wang, and D. T. Organisciak. Amelioration of photic injury in rat retina by ascorbic acid. *Investigative Ophthalmology and Visual Sciences*, 26(1589), 1985.

[46] G. Lin, U. Adiga, K. Olson, J. F. Guzowski, C. A. Barnes, and B. Roysam. A hybrid 3-d watershed algorithm incorporating gradient cues & object models for automatic segmentation of nuclei in confocal image stacks. *Cytometry Part A,*, 56(1):23–36, November 2003.

[47] T. Lindeberg. Feature detection with automatic scale selection. *International Journal of Computer Vision*, 30(2):79–116, 1998.

[48] S. P. Lloyd. Least squares quantization in pcm. *IEEE Transactions on Information Theory,*, 28(2):129–137, 1982.

[49] D. G. Lowe. Distinctive image features from scale-invariant keypoints. *International Journal of Computer Vision*, 60(2):91–110, 2004.

[50] N. Malpica, C. O. de Solorzano, J. J. Vaquero, A. Santos, I. Vallcorba, J. M. Garcia-Sagredo, and F. del Pozo. Applying watershed algorithms to the segmentation of clustered nuclei. *Cytometry.*, 28(4):289–297, 1997.

[51] B. S. Manjunath and W. Ma. Texture features for browsing and retrieval of image data. *IEEE Trans. on Pattern Analysis and Machine Intelligence (PAMI)*, 18(8):837–842, 1996.

[52] B. Matsumoto. *Methods in Cell Biology (Volume 70).* Academic Press, 1993.

[53] K. Mervin, K. Valter, J. Maslim, G. Lewis, S. Fisher, and J. Stone. Limiting photoreceptor death and deconstruction during experimental retinal detachment: the value of oxygen supplementation. *American Journal of Ophthalmology*, 128(2):155–164, 1999.

[54] A. A. Michelson. *Studies in Optics.* Chicago Press, 1927.

[55] J. J. Michon, Z. Li, N. Shioura, R. J. Anderson, and M. O. M. Tso. A Comparative study of Methods of Photoreceptor Morphometry. *Investigative Ophthalmology and Visual Sciences*, 32(2):280–284, 1991.

[56] K. Mikolajczyk and C. Schmid. Indexing based on scale invariant interest points. In *Proc. of IEEE 8th International Conference on Computer Vision and Pattern Recognition*, pages 525–531, Vancouver, Canada, 2001.

[57] K. Mikolajczyk and C. Schmid. Scale & affine invariant interest point detectors. *International Journal of Computer Vision*, 60(1):63–86, 2004.

[58] H. Moravec. Obstacle avoidance and navigation in the real world by a seeing robot rover. Technical Report CMU-RI-TR-3, Carnegie-Mellon University, Robotics Institute, September 1980.

[59] D. Mumford and J. Shah. Boundary detection by minimizing functionals. In *IEEE Computer Society Conference on Computer Vision and Pattern Recognition (CVPR)*, 1985.

[60] K. Murphy. *Dynamic Bayesian Networks: Representation, Inference and Learning*. PhD thesis, Fall 2002.

[61] K. Murphy. Student's t-distribution from math-world- a wolfram web resource., 2007. http://http://bnt.sourceforge.net. Last visited: Mar 25th, 2007.

[62] T. W. Nattkemper. Automatic segmentation of digital micrographs: A survey. *MEDINFO*, pages 847–852, 2004.

[63] A. Nedzved, S. Ablameyko, and I. Pitas. Morphological segmentation of histology cell images. *ICPR*, 1:500–503, 2000.

[64] A. Noble. *Descriptions of Image Surfaces*. PhD thesis, Department of Engineering Science, Oxford University, 1989.

[65] N. Otsu. A threshold selection method from gray-level histograms. *IEEE Transactions on Systems, Man, and Cybernetics*, 9(1):62–66, 1979.

[66] D. M. Paskowitz, G. Nune, D. Yasumura, H. Yang, R. B. Bhisitkul, S. Sharma, M. T. Matthes, M. A. Zarbin, M. M. LaVail, and J. L. Duncan. BDNF Reduction of Retinal Toxicity of Verteporfin PDT. *Investigative Ophthalmology and Visual Science*, 45(11):4190–4196, 2004.

[67] D. L. Pham, C. Xu, and J. L. Prince. Current methods in medical image segmentation. *Annu Rev Biomed Eng.*, 2:315–317, 2000.

[68] K. Rohr. Modelling and identification of characteristic intensity variations. *Image and Vision Computing*, 10(2):66–76, 1992.

[69] J. C. Russ. *The Image Processing Handbook*. CRC, 1995.

[70] K. Sachs, O. Perez, D. Pe'er, D. A. Lauffenburger, and G. P. Nolan. Causal protein-signaling networks derived from multiparmeter single-cell data. *Science,*, 308:523–529, 2005.

[71] T. Sakai, J. B. Calderone, G. P. Lewis, K. A. Linberg, S. K. Fisher, and G. H. Jacobs. Cone photoreceptor recovery following experimental detachment and reattachment: an immunocytochemical, morphological, and electrophysiological study. *Investigative Ophthalmology and Visual Science*, 44:416–425, 2003.

[72] C. Schmid, R. Mohr, and C. Bauckhage. Comparing and evaluating interest points. In *Proc. of IEEE 6th International Conference on Computer Vision*, pages 230–235, Bombay, India, January 1998.

[73] G. Schwarz. Estimating the dimension of a model. *The Annals of Statistics*, 6(2):461–464, 1978.

[74] J. Shi and J. Malik. Normalized cuts and image segmentation. *IEEE Transactions on Pattern Analysis and Machine Intelligence*, pages 888–905, 2000.

[75] J. Shi and C. Tomasi. Good features to track. In *Proc. of IEEE Conference on Computer Vision and Pattern Recognition (CVPR'94)*, pages 593–600, Seattle, Washington, June 1994.

[76] B. Sumengen and B. S. Manjunath. Graph partitioning active contours (gpac) for image segmentation. *IEEE Transactions on Pattern Analysis and Machine Intelligence (PAMI)*, Apr 2006.

[77] M. Tanito, M. H. Elliot, Y. Kotake, and R. E. Anderson. M4-hydroxynonenal and 4-hydroxyhexenal in light-exposed rat retina. *Investigative Ophthalmology and Visual Science*, 46(10):3859–3868, 2005.

[78] B. Triggs. Detecting keypoints with stable position, orientation, and scale under illumination changes. In *Proc. of the 8th European Conference on Computer Vision*, volume 4, pages 100–113, 2004.

[79] V. N. Vapnik. *The Nature of Statistical Learning Theory*. Springer, 1995.

[80] M. R. Verardo, G. P. Lewis, J. Byun, M. Takeda, K. A. Linberg, U. Wilhelmsson, M. Pekny, D. Chen, and S. K. Fisher. Reduced glial hypertrophy and increased neuronal reactivity following retinal detachment in mice deficient in gfap and vimentin, 2007. submitted to *Investigative Ophthalmology and Visual Science*.

[81] E. W. Weisstein. Correlation coefficient from math-world- a wolfram web resource., 2007. http://mathworld.wolfram.com/CorrelationCoefficient.html. Last visited: Mar 19th, 2007.

[82] E. W. Weisstein. Student's t-distribution from math-world- a wolfram web resource., 2007. http://mathworld.wolfram.com/Studentst-Distribution.html. Last visited: Mar 25th, 2007.

[83] R. W. Williams and P. Rakic. Three-dimensional counting: An accurate and direct method to estimate numbers of cells in sectioned material. *Journal of Comparative Neurology*, 278:344–352, 1988.

[84] I. T. Young. Quantitative microscopy. *IEEE Engineering in Medicine and Biology*, 15(1):59–66, 1996.

[85] M. Zuliani, C. Kenney, and B. Manjunath. A mathematical comparison of point detectors. In *Proc. of the 2nd IEEE Workshop on Image and Video Registration*, 2004.

[86] M. Zuliani, C. S. Kenny, and B. S. Manjunath. Condition theory for point neighborhood characteristic structure detection. *IEEE Transactions on Pattern Analysis and Machine Intelligence*, In press, 2006.

Glossary

agarose

A natural colloid extracted from sea weed used to make gels. Agarose gels are formed by suspending dry agarose in an aqueous buffer, then boiling the mixture until a clear solution forms. This is poured and allowed to cool to room temperature to form a rigid gel. Agarose is used to embed tissue for confocal imaging. 24

alpha36H

The specific extracellular matrix molecules. An antibody is used to label unknown chondroitin sulfate proteoglycan 143

apical

The apical membrane of a polarized cell is the part of them plasma membrane that forms its lumenal surface. 11

axon

A long process that emerges from the cell body of a neuron. Axons transmit messages ? like a feeling of pain or a command to move ? throughout the body under the form of an electrical signal. 11, 13, 14, 19, 20

Bayesian network

A probabilistic graphical model that describes statistical independencies between multiple variables. 8, 55, 67, 68, 70, 165, 167, 169, 173, 174, 177, 182, 192, 195

cross section

A vertical section of retina illustrating all layers. 3, 6, 30

CD44

A cell-surface glycoprotein involved in cell-cell interactions, cell adhesion and migration. In retina, CD44 is localized to Muller cell apical microvilli. 135, 143

choroid

The vascular layer of the eye lying between the retina and the sclera. The choroid provides oxygen and nourishment to the outer layers of the retina. 13

CIELab

A color space, defined in terms of L^*,a^*, and b^* coordinates, in which equal distances in the space represent approximately equal color differences. 154

closing

Morphological operation defined as a dilation followed by an erosion. Closing tends to smooth sections of contours, but it generally fuses narrow breaks and long thin gulfs, eliminates small holes, and fills gaps in the contour. 116

DAPI

4'-6-Diamidino-2-phenylindole (DAPI) is a fluorescent stain that binds strongly to DNA. It is used extensively in fluorescence microscopy to recognize a nucleus of a cell. 92, 95, 101

dendrites

The dendrites are numerous and extend from the cell body of the neuron. They allow for a large number of neurons to interconnect forming a network. The dendrites detect the electrical signals transmitted to the neuron by the axons of other neurons. 11, 13, 17–20, 32

electron micrographs

A photographic reproduction of an image formed by the action of an electron beam. 28, 29

fluorescent

A luminescence that is mostly found as an optical phenomenon in cold bodies, in which the molecular absorption of a photon triggers the emission of another photon with a longer wavelength. Usually the absorbed photon is in the ultraviolet range, and the emitted light is in the visible range, but

this depends on the absorbance curve and Stokes shift of the particular fluorophore. 3, 25, 32, 36, 37

glial cells

Glial cells are maintenance and support cells that provide support and nutrition in the central nervous system (CNS). There are two basic types of glial cells, Müller cells and astrocytes. 21

ground truth

Any measurement of an observed quantity that can be used to validate or verify a new (often remote sensing) measurement or technique [from glossary of metrology]. 81, 83, 85

histogram equalization

A method in image processing of contrast adjustment using the image histogram. Through this adjustment, the intensities can be better distributed on the histogram. This allows for areas of lower local contrast to gain a higher contrast without affecting the global contrast. Histogram equalization accomplishes this by effectively spreading out the most frequent intensity values. 37

H & E

Haematoxylin and Eosin, description=Hematoxylin stains tissue a deep blue while eosin stains a deep red. Depending upon the tissue, all cells are composed of a nearly infinite combination of the various hues and shades of these two stains. Most cells have a reproducible staining pattern, regardless of the tissue. 95, 97

hyperoxia

Hyperoxia is excess oxygen in body tissues or higher than normal partial pressure of oxygen. 24

image analysis

Techniques involves the quantification and classification of images and objects of interests within images. 39

image processing

Any technique which alters and displays in more tangible form, the information contained in images. 25

immunocytochemistry

A technique that uses antibody probing to locate the position of a protein in a tissue. 24, 27, 32, 33

immunofluorescent

Immunofluorescence staining. The labeling of antibodies or antigens with fluorescent dyes. Immunofluorescent labeled tissue sections are studied using a fluorescence microscope or by confocal microscopy. 10, 132, 136, 141

interdigitate

To become interlocked like the fingers of folded hands. 11

invaginations

A form or shape resulting from an infolded tissue. 17

microglia

Macrophages that migrate into the retina during development and become quiescent in the adult until activated (by injury, disease, and the like). 135

microvilli

The microvilli are tiny, hairlike structures on the surface of epithelial cells involved in absorption and secretion. 11, 13

morphological operations

Image processing techniques based on mathematical morphology. They are useful in the representation and description of region shape, such as boundaries, skeletons, and convex hull. There are two primary operations: dilation and erosion. They are related to convolution but are more for logical decision-making than numeric calculation. Like convolution, binary morphological operators such as dilation and erosion combine a local neighborhood of pixels with a pixel mask to achieve the result. Dilation, in general, causes objects to dilate or grow in size; erosion causes objects to shrink. The amount and the way that they grow or shrink depend upon the choice of the structuring element. 116

neuropil

A dense intricate feltwork of interwoven fine glial processes, fibrils, synaptic terminals, axons, and dendrites interspersed among the nerve cells in the gray matter of the central nervous system. 17

PDEγ

Phosphodiesterase γ. Anti-PDE γ labels rod and cone outer segments (OS) as well as the entire cone cell. 16, 30

Poisson distribution

Expresses the probability of a number of events occurring in a fixed period of time if these events occur with a known average rate, and are independent of the time since the last event. 36

postsynaptic

The cell whose membranes receive neurotransmitter after its release by another cell (the presynaptic cell) at a synapse 11

retinal quadrants

Four quadrants of a wholemount retina. Superior temporal (ST), superior nasal (SN), inferior temporal (IT), and inferior nasal (IN). The ST quadrant contains the area centralis (macular) and the SN quadrant contains the optic nerve head. 120, 122

retina

A light-sensitive layer of tissue that lines the inside of the eye and sends visual messages through the optic nerve to the brain. 2, 10

retinopathy

Any disease of the retina. Retinopathy is a general term that refers to some form of non-inflammatory damage to the retina of the eye. 24, 164, 166, 167, 169

shot noise

A type of electronic noise that occurs when the finite number of particles that carry energy, such as electrons in an electronic circuit or photons in an optical device, is small enough to give rise to detectable statistical fluctuations in a measurement. 36

TO-PRO

A family of monomeric, cyanine nucleic acid stains that allow very sensitive DNA detection due to good fluorescence signal intensity. 16, 41, 75, 78, 79, 83, 86, 89, 92, 101, 103, 106, 107, 109, 112

vibratome®

Vibrating microtome. One of the tissue sectioning equipments. 24

wholemount

A retinal section viewed from either surface of retina (RPE or ILM) illustrating a specific layer via optical sectioning by confocal microscope. 3, 6, 32

List of Acronyms

artificial neural network (ANN)

Commonly just neural network (NN). An information processing paradigm that is inspired by the way biological nervous systems, such as the brain, process information. The key element is an interconnected group of artificial neurons that uses a mathematical model or computational model for information processing based on a connectionist approach to computation 61, 63

Bayesian information criterion (BIC)

A Statistical criterion for model selection. It is an asymptotic approximation to the full posterior probability and commonly used as a scoring function of a Bayesian network. 70, 173–175

bromodeoxyuridine (BrdU)

A synthetic thymidine analog that gets incorporated into a DNA when the cell is dividing (during the S-phase of the cell cycle). Antibodies against BrdU that are conjugated to fluorescent markers can be used to label these cells thereby providing visual evidence of cell division. 125

carbonic anhydrase II (CA)

A protein expressed in early retina in all the cells, but it becomes later restricted to Müller glia. 143

confocal laser scanning microscopy (CLSM)

A popular mode of optical microscopy in which a focused laser beam is scanned laterally along the x and y axes of a specimen in a raster pattern. The emitted fluorescence (reflected light signal) is sensed by a photomultiplier tube and displayed in pixels on a computer monitor. The pixel display dimensions are determined by the sampling rate of the electronics and the

dimensions of the raster. Signal photons that are emitted away from the focal plane are blocked by a pinhole aperture located in a plane confocal with the specimen. This technique enables the specimen to be optically sectioned along the z axis. 3, 25, 27, 28, 30, 36, 45, 56, 197, 198

central nervous system (CNS)

The largest part of the nervous system, including the brain, the spinal cord, and the retina. 1, 2, 10, 21

cellular retinaldehyde binding protein (CR)

A protein expressed in Müller glia and in cells of the retinal pigment epithelium. 143

C-terminal binding protein 2 (CtBP2)

Synaptic ribbon protein 30

cytochrome oxidase (CX)

An enzyme that acts as a chemical catalyst to facilitate chemical reactions occurring inside of cells as they consume nutrients and produce life-sustaining functions. It is found in mitochondria. 135, 143, 145, 147

electron microscope (EM)

An electron-optical device which produces a magnified image of an object. Detail may be revealed by virtue of selective transmission reflection or emission of electrons by the object. 28

ganglion cell layer (GCL)

A nerve cell layer composed of the cell bodies of ganglion cells. 11, 13, 16, 20, 21, 142, 143

glial fibrillary acid protein (GFAP)

Glial fibrillary acid protein. It is an intermediate filament protein found in glial cells such as astrocytes, ependymal cells, and Müller cells. 8, 22, 34, 46, 48, 70, 128, 135, 142, 143, 154, 155, 159, 165, 166, 169, 170, 172–176, 178–181, 183, 194, 195, 199

graph partitioning active contours (GPAC)

A generic region-based segmentation method based on a new class of variational segmentation cost functions. The cost functions are based on pair-wise

dissimilarities between individual pixels and have been successfully applied to natural images by graph partitioning techniques [76]. 55, 64, 65, 70, 134, 153, 170, 175

glutamine synthetase (GS)

An enzyme that plays an essential role in the metabolism of nitrogen by catalyzing the condensation of glutamate and ammonia to form glutamine. It is detected in Müller cells in retina 143

homogeneous texture descriptor (HTD)

A texture descriptor based on Gabor filters that provides a quantitative characterization of homogeneous texture regions for similarity retrieval. 137, 139, 147, 162

inner limiting membrane (ILM)

Technically not a real membrane, it is a place of fused cell processes. The fusion is between foot processes of the Müller cells. 11, 21, 22, 32

inner nuclear layer (INL)

A nerve cell layer composed of the cell bodies of bipolar cells and horizontal cells. 11, 13, 16, 18, 19, 21, 32, 75, 83, 86, 89, 104, 106, 128, 130, 131, 142, 143, 151, 154, 158, 183, 186–189, 192, 194

inner plexiform layer (IPL)

A plexiform layer composed of the dendrites of ganglion cells and post synaptic terminal of horizontal cells and bipolar cells. 11, 13, 20, 142, 143, 149, 151, 170

inner segments (IS)

Inner segments of photoreceptors. 14, 15, 142, 143, 149

Laplacian of Gaussian (LoG)

A combination of a Laplacian and Gaussian filter where its characteristic is determined by the σ parameter and the kernel size as shown in the mathematical expression of the kernel. 79, 81

numerical aperture (NA)

In optics, the numerical aperture (NA) of an optical system is a dimensionless number that characterizes the range of angles over which the system

can accept or emit light. The N.A. of each objective lens is inscribed in the metal tube, and ranges from 0.25 to 1.4. 38

outer limiting membrane (OLM)

Technically not a real membrane, it is formed by the junctional complexes between photoreceptor cells and the glial cells of the retina. 11, 16, 21, 22, 48

outer nuclear layer (ONL)

A nerve cell layer composed of the cell bodies of the rods and cones. 3, 4, 8, 11, 13, 16, 17, 27, 40, 41, 43, 44, 48, 56, 61, 66–68, 70, 72, 75–79, 83–86, 91, 99–101, 103, 104, 106–109, 111, 112, 116–118, 120, 122, 123, 125, 127, 128, 130, 131, 133–139, 142, 143, 147, 151, 153–155, 157–164, 166, 169, 170, 172, 173, 175, 178, 180, 183, 185–189, 192, 194

outer plexiform layer (OPL)

A plexiform layer composed of the pre synaptic terminal of horizontal cells and bipolar cells, and synaptic terminals of the rods and cones. 11, 13, 17, 18, 20, 27, 142, 143, 149, 151, 154

outer segments (OS)

Outer segments of photoreceptors. 4, 13–16, 43, 141–143, 151, 170, 183

phosphate buffered saline (PBS)

A buffer solution commonly used in biochemistry. It is a salty solution containing sodium chloride, sodium phosphate and potassium phosphate. The buffer helps to maintain a constant pH. The concentration usually matches the human body (isotonic). 24

protein kinase C (PKC)

Protein kinase C. 18, 19

peanut agglutinin (PNA)

PeaNut Agglutinin preferentially binds galactose-containing carbohydrates, especially galactose-galactosamine linkages, selectively labels cone photoreceptor-associated domains of the cone matrix sheaths in a variety of vertebrate retinas. 143

retinal pigment epithelium (RPE)

The pigmented cell layer adjacent to the neurosensory retina that nourishes retinal visual cells, and is firmly attached to the underlying choroid and overlying retinal visual cells. 11, 13, 24, 32, 151, 186, 189

retinoschisis (RS)

A genetic disease that affects the vision of men who inherit the disease from their mothers. This condition frequently starts during childhood and is officially called Juvenile X-linked Retinoschisis. Affected men inherit this trait from their mothers who carry the condition but retain normal vision. 181, 182

retinoschisin knockout (RSKO)

The gene producing a protein, retinoschisin, has been knocked out of that particular organism 182, 183, 185–190, 192, 194, 195

support vector machine (SVM)

Statistical pattern recognition technique [79]. 55, 61–63, 70, 135, 137–139, 147, 162

transmission electron microscope (TEM)

An electron-optical device which produces a magnified image of an object by transmission electrons. 25, 28, 29, 198

vesicle associated membrane protein (VAMP)

Vesicle associated membrane protein in synaptic terminals 17

wild type (WT)

The typical form of an organism, strain, gene, or characteristic as it occurs in nature, as distinguished from mutant forms that may result from selective breeding. 182, 183, 185, 186

Index